

RWTH Aachen University of Technology



Department of Cardiovascular Engineering

Univ.-Prof. Dr.-Ing. Ulrich Steinseifer

Institut of Applied Medical Engineering

and



Auckland Bioengineering Institute

Prof. Peter Hunter

Eine strukturbasierte Analyse der Remodellierung des

Herzmuskels

Entwicklung eines Materialmodells

A Structure-Based Analysis of Cardiac Remodelling

A Constitutive Modelling Approach

Presented for Master thesis

Name, Matr.-No.: Cand. Ing. Justyna Niestrawska, Matr.-No. 288585

Date: 20.12.2013

Supervised by Prof. Martyn Nash, Ph.D. Vicky Wang

 Dipl.-Ing. Jan Roggenkamp

This publication is meant for internal use only. All rights reserved by the Department of
Cardiocascular Engineering, RWTH Aachen University.

Declaration

I certify that this work has been carried out and written up entirely by myself. No literature references and resources other than those cited have been used. To the best of my knowledge and belief, the thesis contains no material previously published or written by any other person except where due reference is made.

Place, Date

Signature

Acknowledgements

I would like to thank my supervisors, Professor Martyn Nash (Associate Director Research, Auckland Bioengineering Institute) and Dr. Vicky Wang for their unwavering guidance and tremendous amount of support and motivation throughout my thesis. Thank you for handing on your enthusiasm and excitement about cardiac mechanics and also for making it easy for me to feel welcomed in a new institute and a new city at the other side of the world.

I would also like to thank Associate Professor Ian LeGrice and Dr. Gregory Sands for sharing their vital expertise and knowledge about the structure of the heart.

Also many thanks to Alexander Wilson for letting me look over his shoulder (and for the little pranks that made everyday life interesting).

For the opportunity to work in a world renowned institute and to live in New Zealand for 10 months I would like to thank the Chair of Medical Engineering at the Helmholtz Institute for Biomedical Engineering, RWTH Aachen and especially Professor Klaus Radermacher and Dipl.-Ing. Christine Goffin. Thank you for the organization of this exchange program.

Many thanks to Dipl.-Ing. Jan Roggenkamp for being my supervisor back at home. Thank you for your time and your support throughout my thesis.

Last but not least I would like to thank my parents and Jan for letting me leave and supporting me during all struggles, regardless how stressed and unfriendly I was.

Definition and Scope of Work

Abstract

Heart failure (HF) is a common cause of hospitalization. It is a heterogeneous disease which involves an impaired ability for the heart to pump blood to meet the body's requirements. Initially HF has been characterised as ventricular dysfunction during systole (systolic HF). However, it has been recently found that a large number of patients develop dysfunction during ventricular filling (diastolic HF).

The mechanical function of the heart exhibits a high complexity which can be affected by both local and global mechanical properties. To develop a deeper understanding of the processes during HF it is essential to develop computational models of the left ventricle (LV). Although computational models of LV mechanics have been studied intensively, constitutive equations that describe mechanical properties of myocardium especially under diseased conditions are still lacking in the field. Also existing constitutive models are often empirical and its parameters lack physical meaning. Hence there is an evident need for the development of a new passive constitutive equation which reflects the structure of myocardium more directly and is capable of reproducing clinically relevant functional outputs such as LV pressure-volume relations.

The goal of this thesis is to develop a novel structure-based constitutive model of the rat heart that is capable of representing the passive mechanical response of normal and diseased myocardial tissue, utilizing data derived from cine MRI, confocal microscopy images and ex-vivo pressure-volume measurements.

A literature review on existing constitutive relations for passive LV mechanics has been undertaken. Based on this review a series of modifications to an existing constitutive law have been implemented and their influence on local and global passive mechanics have been investigated using Finite Element (FE) simulation of simple shear, biaxial extension and passive LV filling.

For the first time a constitutive model using a single set of material parameters combined with structural parameters derived directly from images has been demonstrated to predict passive LV function of both normal and diseased hearts.

Keywords

Heart Failure, Constitutive Modelling, Structural Images, Cardiac Tissue Mechanics

Zusammenfassung

Herzinsuffizienz stellt eine der häufigsten internistischen Erkrankungen dar. Es handelt sich um eine heterogene Erkrankung, die sich dadurch auszeichnet, dass das Herz unfähig ist dem Körper die benötigte Blutmenge zuzuführen. Ursprünglich ist Herzversagen als die Dysfunktion des kontraktilen Verhaltens während der Systole bezeichnet worden. Jüngste Studien deuten jedoch darauf hin, dass viele Patienten mit Herzinsuffizient eine Fehlfunktion der Füllung des Ventrikels während der Diastole aufweisen.

Die mechanische Funktionsweise des Herzens weist eine hohe Komplexität auf, bei der sowohl lokale als auch globale mechanische Eigenschaften eine Rolle spielen. Um ein tieferes Verständnis für die Vorgänge während des Herzversagens zu entwickeln, ist es sinnvoll, Computermodelle zu entwickeln. Die bereits existierenden Modelle sind meist empirisch. Deshalb ist es erforderlich, ein neues passives Materialgesetz das sowohl die Struktur des Myocardiums direkter beschreibt als auch klinisch relevante Daten wie Druck-Volumen-Verhältnisse im linken Ventrikel berücksichtigt.

Das Ziel dieser Arbeit ist es, ein solches neuartiges, struktur-basiertes Materialmodell zu entwickeln, das in der Lage ist die passive mechanischen Eigenschaften von gesundem und krankem Myocardium zu repräsentieren. Hierzu wurden sowohl magnetresonanztomographische (cine MRT) und konfokalmikroskopische Aufnahmen als auch ex-vivo Druck-Volumen Relationen verwendet.

Zu diesem Zweck wurde zunächst eine Literaturrecherche zu dem Stand der Technik in Materialmodellen für Weichgewebe, speziell das Myocardium betreffend, durchgeführt Anschließend wurden Mikroskopieaufnahmen des Herzens analysiert und darauf aufbauend Modifikationen an einem existierenden Modell durchgeführt. Deren Einfluss auf die lokale und globale passive Mechanik wurde mit Hilfe von Finite Elemente Simulationen von einfacher Scherung, biaxialer Dehnung und passiver Füllung untersucht.

Erstmals war es möglich ein Materialgesetz zu entwickeln, das mit einem Set von Materialparametern kombiniert mit strukturbasierten Parametern aus Mikroskopieaufnahmen in der Lage war, Druck-Volumen-Verhältnisse im linken Ventrikel von sowohl gesunden als auch kranken Herzen zu beschreiben.

Schlagwörter

Herzinsuffizienz, Materialgesetz, strukturbasierte Aufnahmen

Table of Contents

Acknowledgements.....	I
Definition and Scope of Work	III
Abstract.....	V
Zusammenfassung.....	VII
1 Introduction.....	1
2 Objectives	3
3 Background.....	5
3.1 Anatomy and Function of the Heart	5
3.2 Architecture and Mechanical Properties of the Heart	7
3.3 Indicator of Function	9
3.4 Heart Failure	10
3.5 Fundamental Elements of Continuum Mechanics	12
3.6 Computational Modelling Tools.....	14
4 Constitutive Modelling Preliminaries	15
4.1 Constitutive Relations	15
4.2 State of the Art in Constitutive Equations.....	16
4.3 Experimental Data Sources.....	25
4.4 Summary of Structural Changes	29
5 Modelling Framework	33
5.1 Material Parameter Estimation.....	33
5.2 Simulation of Simple Shear	34
5.3 Simulation of Axial Extension	35
5.4 Finite Element Modelling of Passive Filling	35
5.5 Subject Specific Geometry Fitting.....	37
5.6 Subject Specific Parameter Estimation	37
6 Constitutive Equations for Heart Failure Mechanics.....	41
6.1 Augmented Holzapfel Equation	41

6.2	First Modification.....	43
6.3	Second Modification.....	45
6.4	Convexity and Material Stability.....	48
7	Modelling of Heart Failure Mechanics	51
7.1	Implementation of the Augmented Holzapfel Equation	51
7.2	Implementation of the First Modification.....	55
7.3	Implementation of the Second Modification.....	61
8	Summary and Future Work.....	77
9	Nomenclature	81
10	References.....	83
11	Appendix	87
11.1	Appendix 1A.....	87
11.2	Appendix 1B	89
11.3	Appendix 1C	90
11.4	Appendix 2A.....	91
11.5	Appendix 2B.....	92
11.6	Appendix 2C	93
11.7	Appendix 2D.....	94
11.9	Appendix 3A.....	95
11.10	Appendix 3B	98

1 Introduction

Heart failure (HF) is one of the leading causes of hospitalisation in the world; in New Zealand 4 % of deaths are due to HF. During HF the heart is unable to pump sufficient blood to meet the body's metabolic requirements. Conventionally HF has been characterised by impaired contractile performance and enlargement of the left ventricle (LV). However, equal numbers of patients who exhibit HF syndromes have preserved ejection fraction with impaired ventricular filling, referred to as diastolic HF. Although they require different treatments there is a debate whether systolic and diastolic HF are distinct or overlapping diseases. The pathophysiological mechanisms are poorly understood and there is no knowledge about changes in tissue properties due to the remodelling of the LV during HF. [1, 2]

The Heart Mechanics group at the Auckland Bioengineering Institute, University of Auckland is interested in investigating the biophysical mechanisms which are responsible for the impaired mechanical function during HF using an animal model. This mechanistic insight will help in the long term to develop treatments that are targeted to specific aspects of cardiovascular dysfunction. For this purpose spontaneously hypertensive rats (SHRs) and Wistar-Kyoto controls (WKY) are being studied. SHR become hypertensive at an early age and develop diastolic abnormalities at 12 months. This is followed by ventricular dilatation and death due to systolic pump failure at 24 months. They are a useful animal model because they develop features that are close to those seen in human HF [1]. In previous studies high resolution confocal imaging revealed reorganisation of SHR myocardium, including enlargement of myocyte cross section and fusion of perimysial collagen. Also differences in chamber stiffness have been recorded [3]. Motivated by these findings the Cardiac Mechanics group aims to characterise tissue specific mechanical properties for both healthy and diseased hearts by modelling mechanical behaviour of LV myocardium.

Several continuum models of LV mechanics have been employed to investigate the contribution of cardiac geometry and passive material properties to diastolic dysfunction. However, constitutive equations are usually purely empirical and the

material parameters lack physical meaning. Furthermore it is often impossible to isolate the mechanical behaviour along distinct material directions and material parameters are highly correlated because of the coupled influence of parameters on LV deformation [4]. Hence there is an obvious need for a new constitutive model that is capable of capturing information from imaging and clinically relevant functional outputs.

2 Objectives

The objectives of this master's thesis were to:

- Undertake a literature review for existing continuum models for passive myocardium and use this knowledge as a starting point for the development of a new model.
- Develop a new passive constitutive equation that represents the mechanical response of healthy and diseased myocardial tissue. A model like this is designed to provide a mechanistic insight into the pathophysiological variations of LV mechanics under HF conditions, based on the structural and mechanical data from Spontaneously Hypertensive rats (SHRs).
- Tailor the constitutive model to enhance the robustness and predictability of material parameters that will be estimated to predict the different mechanical responses of healthy and diseased myocardium.

3 Background

3.1 Anatomy and Function of the Heart

The heart is a hollow muscular organ that distributes oxygenated blood to the body and assures the survival of peripheral tissues. It can adjust the output to meet a wide range of metabolic needs of the body, from sleep to exercise. The heart can be seen as two pumps that work in series, with the right heart generating lower pressures than the left heart: the right atrium (RA) and right ventricle (RV) that pump blood into the pulmonary circulation, and the left atrium (LA) and left ventricle (LV) which pump blood into the systemic circulation. Within the heart, valves control the direction of blood flow (Fig. 3-1). [5]

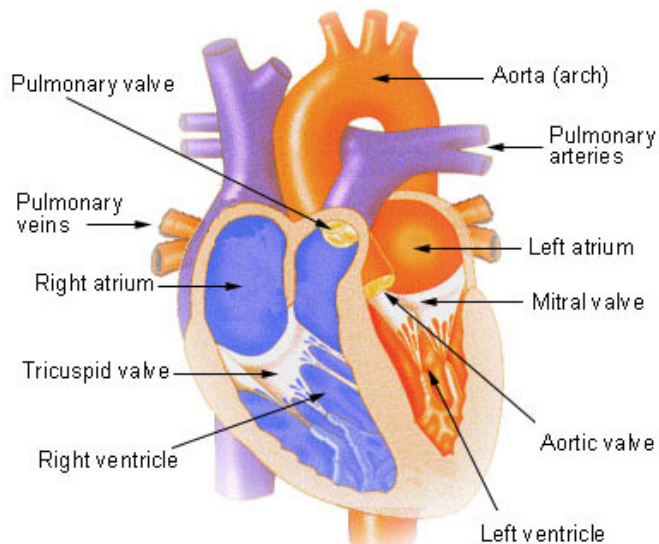


Fig. 3-1 Anatomy of the heart [6]

The pump function is regulated by a coordinated sequence of electrical and mechanical events repeated in every cardiac cycle, which is summarised in the Wigger's Diagram for the left heart (Fig. 3-2). [5]

A cardiac cycle can be divided into two phases: systole and diastole. The following paragraph describes systole and diastole in the left heart, although an equivalent sequence occurs in the right heart. [5]

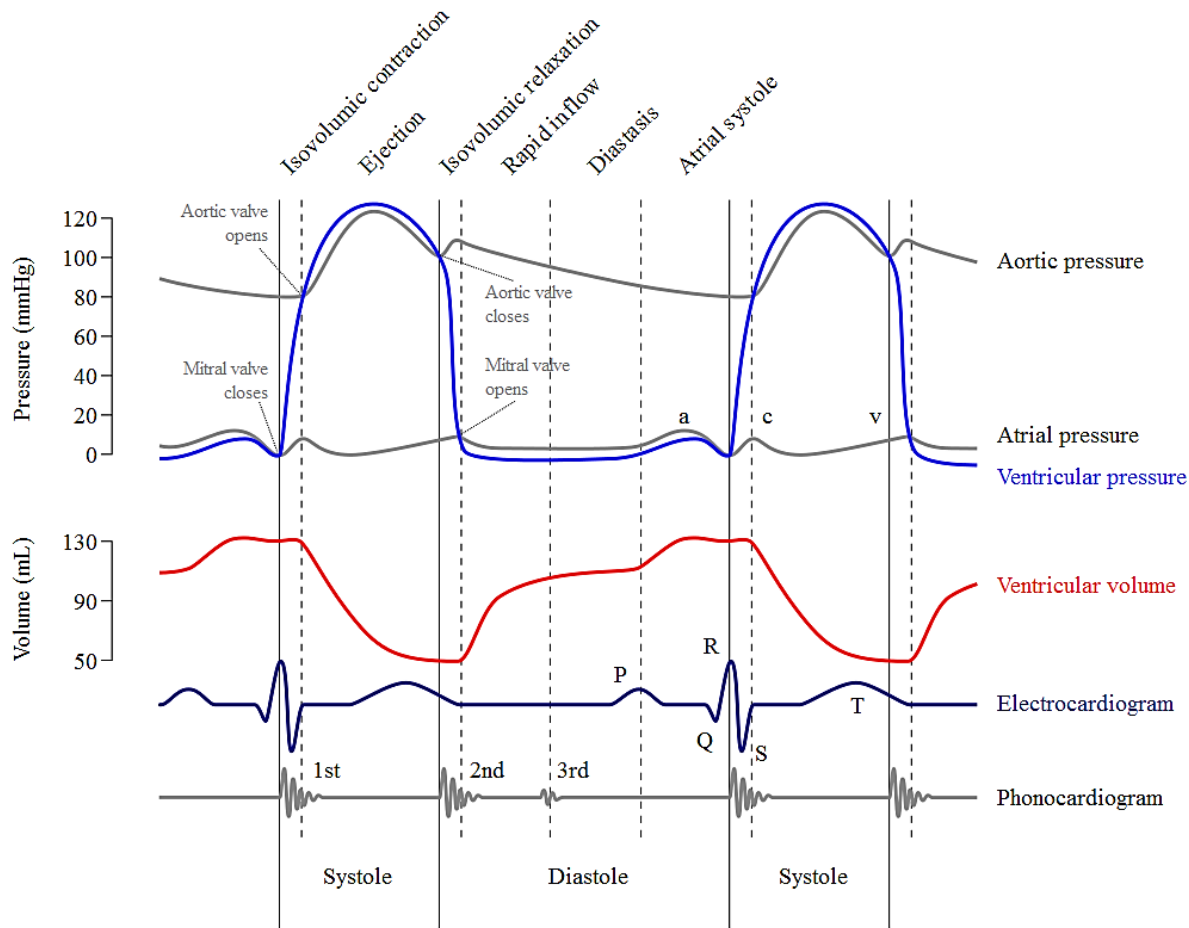


Fig. 3-2 Wigger's Diagram for the left heart [7]

Systole represents the period of time when left and right ventricles contract. Since inlet and outlet valves are initially closed the ventricular pressure increases with no change in volume (isovolumetric contraction). As soon as the pressure in the LV exceeds the pressure in the aorta, the aortic valve opens and blood is ejected into the systemic circulation. In the later part of systole blood flow decelerates with an inversion of the pressure gradient that causes the aortic valve to shut. During ventricular systole, pressure in the LA decreases because the atrial base is pulled downwards, increasing the volume in the LA, and as a result blood flows into the LA from the pulmonary veins. [8]

Diastole on the other hand is the time during which the ventricles are relaxed. Initially inlet and outlet valves are closed and the ventricular pressure decreases, again with no change in volume (isovolumetric relaxation). Meanwhile, blood continues to flow into the atria. When the intraventricular pressure falls at some point below the atrial pressure, the atrio-ventricular valves open, enabling ventricular filling. As the ventricle continues to fill the intraventricular pressure rises, which reduces the pressure gradient across the valve and ventricular filling slows. Diastasis is the middle stage of diastole when the initial passive filling has

slowed down. The final phase of diastole is when the atria contract and is termed 'active filling'. [8]

3.2 Architecture and Mechanical Properties of the Heart

The heart muscle, myocardium, is composed of myocytes that make up 70 % of myocardium by volume. Non-myocytes such as fibroblasts, macrophages etc., vascular tissue and the extra cellular matrix (ECM) which comprises fibrillar proteins make up the remainder. ECM is important in defining myocardial architecture and contributes not only to transmural force transmission but also to potential energy storage during the systole and to the limitation of sarcomere extension during diastole. The predominant component of the ECM is collagen that provides tensile support and hence plays a central role in the mechanical performance of the heart. It can be classified into three main components: epimysium, which surrounds the entire muscle, perimysium, interconnecting and surrounding groups of myocytes and endomysium, which surrounds and connects individual myocytes and capillaries (Fig. 3-3). [9]

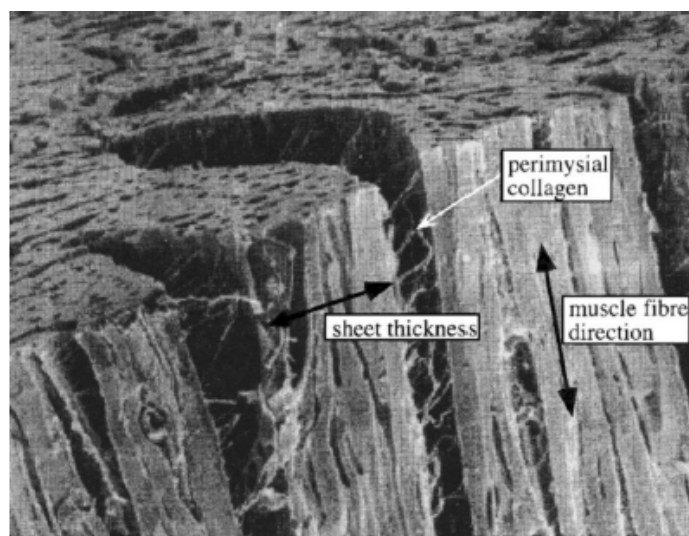


Fig. 3-3 Two orthogonal surfaces of mid-wall specimen [10]

Myocytes are roughly cylindrical cells with typical lengths from 80 μm to 100 μm and diameters that range from 10 μm to 20 μm . They are arranged in a branching network and are connected to each other longitudinally at multiple points through intercalated disks. These disk junctions are the site of electrical and mechanical coupling between myocytes, through gap junctions and adherens junctions respectively. [11]

Cardiac myocytes themselves are comprised of sarcomeres arranged in series and parallel. Sarcomeres are basic units of contraction and consist of thick and thin filaments that slide past each other whilst the muscle contracts (Fig. 3-4). The

amount of interaction between actin and myosin determines the amount of force generated during contraction. [2]

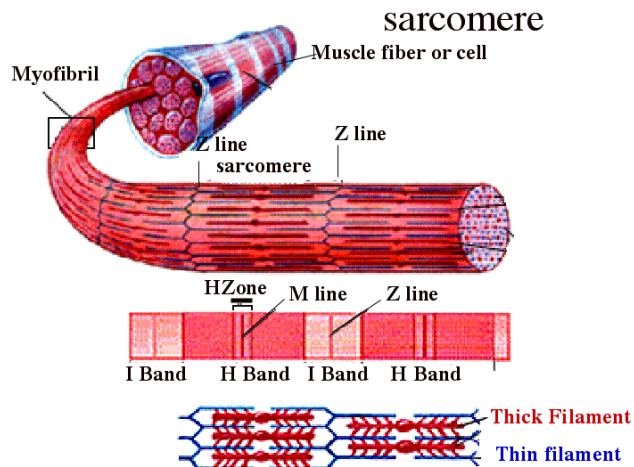


Fig. 3-4 Myocytes sarcomere arrangement [2]

Le Grice et al. [12] showed that myocardium is not a uniformly connected structure but consists of groups of myocytes that are arranged into layers which are on average four cells thick bound by endomysial collagen and separated by cleavage planes. Thus, a natural set of material directions can be defined in the myocardium; fibre, sheet and sheet-normal as shown in Fig. 3-5. From these observations it can be suggested that myocardium should exhibit orthotropic behaviour. The myocyte layers are loosely coupled by perimysial collagen, which provides them with the ability to slide over each other [11].

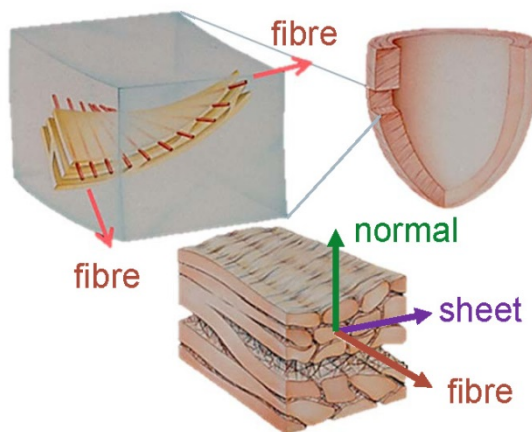


Fig. 3-5 myocardium structure, adapted from [11]

When viewed in planes parallel with the epicardial surface, the orientation of the 'myocardial sheets' varies smoothly across the ventricular wall from - 60° at the epicardial surface to + 90° near the endocardium. This has typically been described as the transmural variation in myocardial fibre orientation. When viewed in planes cut across the ventricular wall the orientation of the myocardial

laminae are also seen to vary from epicardium to endocardium, however this is regionally more variable than the fibre orientation. Although the muscle layer orientation is uniform, the degree of coupling between contiguous layers varies across the wall with a higher density of branching between muscle layers at the subepicardium than at the midwall. [12]

Myocardium has a highly nonlinear, anisotropic stress-strain behaviour in biaxial tension tests. The stress-strain properties along the three structurally-based axes are quite different, reflecting the collagen organisation along these axes. Fig. 3-6 describes schematically the reaction of myocardium when stretched along each of the three axes. [11]

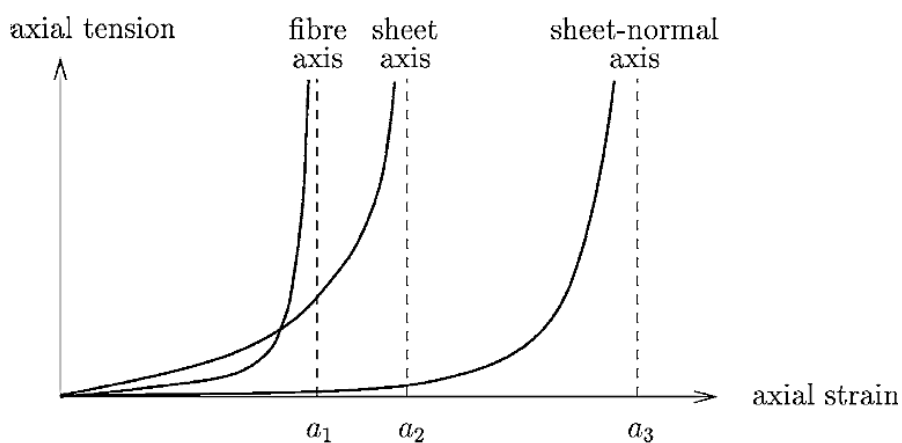


Fig. 3-6 strain-stress properties of ventricular myocardium [13]

3.3 Indicator of Function

To analyse the characteristics of cardiac performance a pressure-volume-loop for the LV can be constructed by plotting cavity pressure versus volume during a single cardiac cycle. The loop represents four basic stages of the cardiac cycle as seen in the Wigger's diagram: 1. diastolic filling, 2. isovolumetric contraction, 3. ejection and 4. isovolumetric relaxation (see Fig. 3-7 a)). Several hemodynamic parameters can be determined from this loop, including cardiac output, myocardial contractility, ejection fraction. Stroke work (SW), which is the external work performed by the heart, can be determined from the area enclosed by the loop, whereas the volume of blood ejected during one cardiac cycle is the stroke volume (SV). It can be defined by the difference between end-diastolic and end-systolic volumes. [1]

The analysis of pressure-volume loops can help to understand key aspects of normal and pathologic cardiac performance, although it should be considered that mechanics of the ventricle should not be reduced to a 1D problem. In Fig. 3-7 b) and c) the effects of diastolic and systolic dysfunction on the pressure-volume loop can be seen. For example, if passive LV compliance (change in volume for a

given applied pressure) is reduced due to hypertrophy, diastolic dysfunction may occur (Fig. 3-7 b)). If the capacity to generate active force is reduced a decreased slope of the active pressure volume relation is seen, resulting in a reduced SV for a given end-diastolic volume (systolic dysfunction, Fig. 3-7 c)). [1]

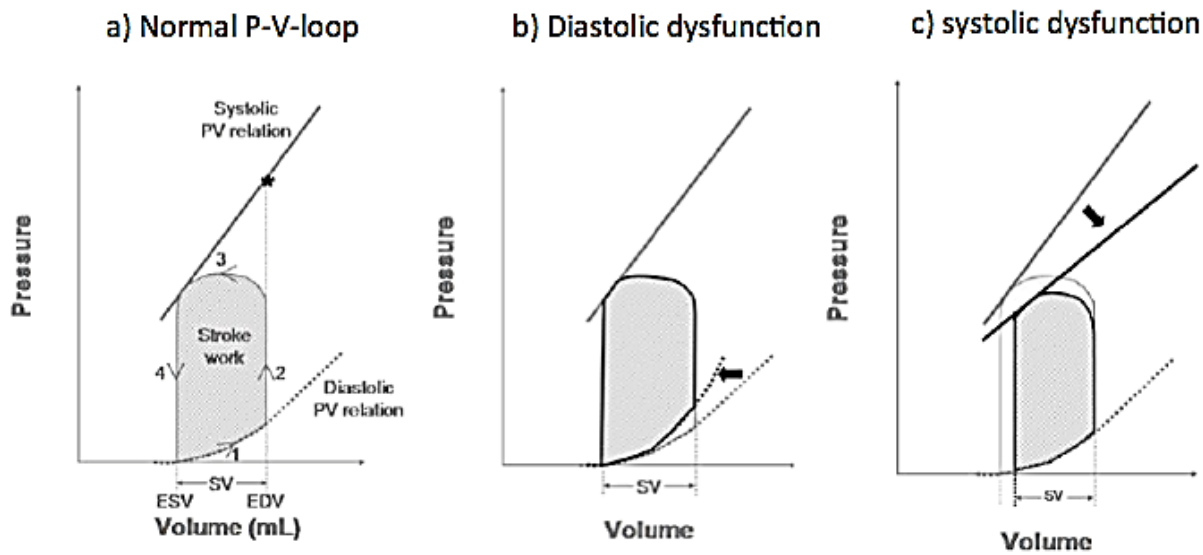


Fig. 3-7 Modifications in cardiac pressure-volume-loops (adapted from [1])

3.4 Heart Failure

The term heart failure describes a complex disease since it is a final result of multiple possible dysfunctions of the heart, e.g. hypertensive heart disease (HHD), valvular disorders, or coronary disease etc. [14]

Heart failure affects about 2 % of the Western population and is the most common hospitalization cause for patients over 65 years of age. In New Zealand, 4 % of deaths are due to heart failure [1]. It is defined as an impaired ability of the heart to fill and/ or eject blood such that it cannot adequately meet the metabolic needs of the body. [14]

Traditionally, the term heart failure has been described as a reduced ejection fraction and enlargement of the LV (systolic heart failure, or heart failure with reduced ejection fraction - HFrEF). Nevertheless, it has become recognized that HF can occur even when ejection fraction is normal - a normal contractile function with impaired ventricular filling is then defined as diastolic heart failure or heart failure with preserved ejection fraction (HFpEF). To define the syndrome of HFpEF three general criteria have been proposed: 1. "Clinical symptoms of heart failure"; 2. "Normal LV systolic function"; and 3. "Evidence of abnormal LV diastolic function". [14] Several features of HFpEF fraction have been characterized, for example structural and functional alterations of the heart such

as hypertrophy of myocytes, changes in the composition of the ECM and abnormalities in intracellular calcium handling. [2]

All these characteristics underlie impaired LV diastolic relaxation and decreased LV compliance, but are not necessarily specific HFpEF fraction since they can be found in hypertensive individuals as well as in individuals with HFrEF. [15] It is currently unknown whether systolic and diastolic HF are distinct or overlapping diseases [16, 17]. Although there have been conflicting results in recent research regarding this question, systolic and diastolic HF require different treatments. In fact there are no treatments currently that alter the course of diastolic HF. This therapeutic difference remains unexplained, in part because the pathophysiological mechanisms underlying heart failure are poorly understood. [14]

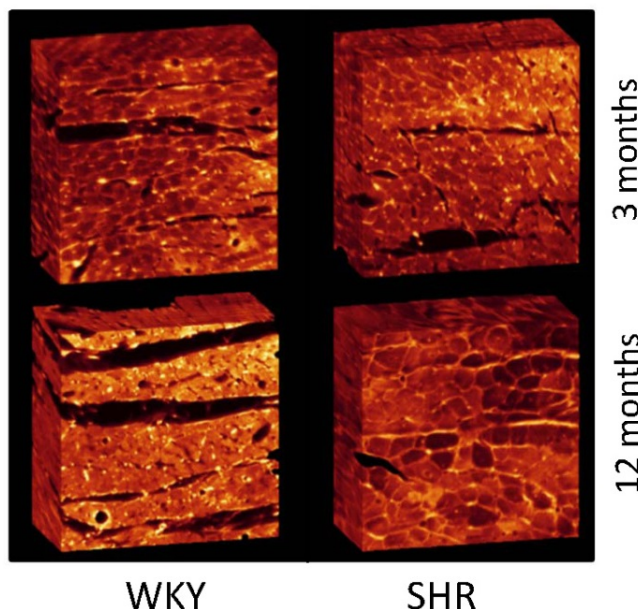


Fig. 3-8 Confocal microscopy images of SHR (right) and healthy rat myocardium (left) [18]

In many disease states the heart remodels its muscular structure as part of an attempt to maintain adequate function in some cardiovascular diseases, such as hypertension. This is seen clearly in the spontaneously hypertensive rat (SHR), a good animal model of human HHD since it replicates the classical progression of structural and functional changes seen in human HHD. Using quantitative extended confocal microscopy techniques [3] it is possible to observe several changes in myocardial tissue structure (see Fig. 3-8). These changes include progressive reorganisation of the extracellular matrix such as loss of laminar structure and myocytes being surrounded by thick layers of endomysial collagen. Additionally myocyte hypertrophy, increased variability in myocyte diameter and increased ventricular wall thickness occur. Furthermore a progressive diastolic dysfunction with eventual progression to systolic heart failure is observed. [1]

The changes in LV geometry in HHD are illustrated in Fig. 3-9. The initial response of the heart to pressure overload which occurs in HHD is concentric ventricular hypertrophy (case b). The heart preserves the cavity volume, generates greater contractile force during systole and normalises wall stresses by increasing the cross sectional area. The ejection fraction is usually preserved in this stage of HHD. During eccentric hypertrophy (case c) sarcomeres are added in series which results in ventricular dilatation and wall thinning. This can be observed in later stages of HHD as a result of increasing passive stiffness and ongoing pressure overload. With dilatation the sphericity of the LV chamber increases. [19]

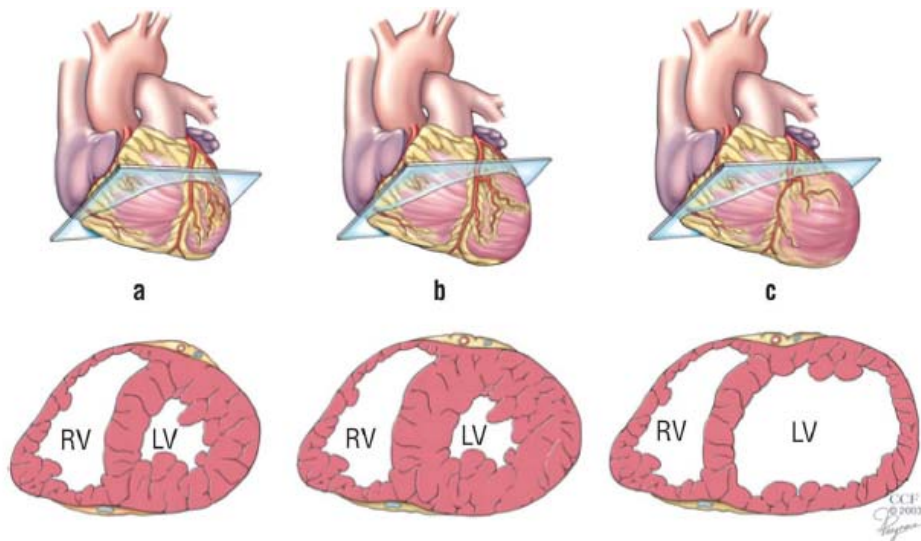


Fig. 3-9 a) healthy LV, b) concentric hypertrophy, c) eccentric hypertrophy [20]

3.5 Fundamental Elements of Continuum Mechanics

To be able to represent deformation and traction fields acting on myocardium stress and strain in finite deformation elasticity theory have to be determined. For this purpose a two-state quasi-static analysis is used: the undeformed, stress-free state at a LV pressure of zero and a deformed state after reaching equilibrium. Fundamental equations for this analysis are summarised below. [2]

To define the deformation undergone by the heart between the two states mentioned above a deformation gradient tensor \mathbf{F} can be defined.

Equation 3-1

$$\mathbf{F}_M^i = \frac{\partial x_i}{\partial X_m}$$

where x_i represent the deformed coordinates of a material point p and X_m represent the undeformed coordinates of the same point p. The subscript (*i*)

represents spatial coordinates with respect to a global reference coordinate system and (M) material coordinates (see Fig. 3-10). [11]

For the calculation of strain in the deformed material two tensors are introduced: the right Cauchy-Green deformation tensor (\mathbf{C} , Equation 3-2) and the Lagrangian Green's strain tensor (\mathbf{E} , Equation 3-3), which contains kinematic information. [11]

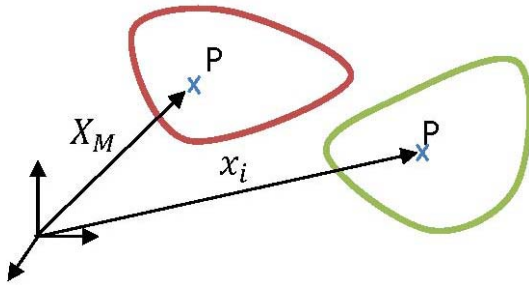


Fig. 3-10 Description of deformation by relating material coordinates X_M to spatial coordinates x_i , red is the undeformed and green the deformed configuration

Equation 3-2

$$\mathbf{C} = \mathbf{F}^T \mathbf{F} = \left\{ \frac{\partial x_k}{\partial X_M} \frac{\partial x_k}{\partial X_N} \right\}$$

Equation 3-3

$$\mathbf{E} = \frac{1}{2} (\mathbf{C} - \mathbf{I})$$

where \mathbf{I} is the identity tensor. It is useful to define properties of the right Cauchy-Green deformation tensor that remain constant despite rotations. These principal invariants of \mathbf{C} are defined as follows:

Equation 3-4

$$I_1 = \text{tr}(\mathbf{C}), I_2 = \frac{1}{2} [I_1^2 - \text{tr}(\mathbf{C}^2)], I_3 = \det(\mathbf{C})$$

To gain information about kinetics, stress equilibrium equations and a stress tensor are required. These are deduced from the laws of conservation of mass, linear and angular momentum and the principle of virtual work. In the engineering field three types of stress tensors are used: the Cauchy stress tensor, the first Piola-Kirchhoff stress tensor and the second Piola-Kirchhoff stress tensor. They differ in the states in which force and area are quantified. Since the second Piola-Kirchhoff stress tensor (\mathbf{T}^{MN}) describes material behaviour at a point in the reference configuration and thus represents stresses with respect to material coordinates it is used in finite deformation elasticity theory. It is

independent of rigid-body rotation or translation and is related to the Cauchy stress tensor σ as shown in Equation 3-5. [11]

Equation 3-5

$$\sigma = J^{-1} \mathbf{F} \cdot \mathbf{T} \cdot \mathbf{F}^T, J = \det(\mathbf{F})$$

The Cauchy stress tensor is defined with respect to a deformed body configuration. Since it is difficult to interpret the physical meaning of the second Piola-Kirchhoff stress tensor large deformation problems are often solved in terms of the Cauchy stress. [11]

3.6 Computational Modelling Tools

CMISS (<http://www.cmiss.org/>) stands for continuum mechanics, image analysis, signal processing and system identification. It is a mathematical modelling environment designed for solving complex bioengineering problems using finite element and boundary element analysis and collocation techniques. It consists of a graphical front end (cmgui: cm graphical user interface) that has advanced 3D modelling capabilities and a computational backend.

CellML (<http://www.cellml.org>) is a language based on the XML markup language. It is being developed by the Auckland Bioengineering Institute as an open standard. The purpose is to store and share computational mathematical models via an online repository. It was originally designed to describe biological models; however CellML is now used for broader applications such as the implementation of constitutive equations.

For its application describing constitutive equations the CellML code takes six components of Green's strain tensor as variable inputs and a number of constants to represent material parameters. The 2nd Piola Kirchhoff stress tensor components are herewith calculated and output to an external framework.

4 Constitutive Modelling Preliminaries

This section starts with an introduction to constitutive relations used to describe relations between stress and strain for large deformations, especially for those undergone by the heart muscle. A literature review is given on the state of the art of modelling ventricular mechanics and the need of improvement to be able to model heart failure is pointed out. Subsequently experimental data sources used to model heart failure are introduced and a summary on structural changes that occur during heart failure is given.

4.1 Constitutive Relations

Relations between stress components and deformation are unique for each material. While Hooke's law can be used to describe the stress-strain relationship of linear elastic materials such as steel, the relationships for other materials such as myocardium can be nonlinear and thus much more complex. In the context of finite deformation elasticity they are defined by constitutive relations. [11]

The second Piola-Kirchhoff stress tensor (\mathbf{T}) can be expressed in terms of Lagrangian Green's strain tensor as follows:

Equation 4-1

$$\mathbf{T}^{MN} = \frac{1}{2} \left(\frac{\partial W}{\partial E_{MN}} + \frac{\partial W}{\partial E_{NM}} \right)$$

where \mathbf{W} is the strain energy density function. [11]

Since the heart can be assumed as incompressible, the incompressible constraint ($I_3 = 1$) should be taken into account and with that another term called hydrostatic pressure (p) should be added to Equation 4-1 to ensure that all diagonal terms of the stress tensor are representing true hydrostatic stress. Since not only passive response of myocardium to deformation should be taken into account but also active contraction a third term has to be added. Contraction of the heart is due to activation of myocytes by an electrical wave propagating through the heart. The contractile stress generated is represented in the term T_a , assuming that contractile tension is generated mainly along the longitudinal axes

of the myocytes. Equation 4-2 becomes a general form of constitutive relation for the myocardium. [11]

Equation 4-2

$$\mathbf{T}^{MN} = \frac{1}{2} \left(\frac{\partial W}{\partial E_{MN}} + \frac{\partial W}{\partial E_{NM}} \right) - p \frac{\partial X_M}{\partial x_k} \frac{\partial X_N}{\partial x_k} + T_a \frac{\partial X_M}{\partial x_1} \frac{\partial X_N}{\partial x_1}$$

4.2 State of the Art in Constitutive Equations

In general two categories of constitutive models can be distinguished: phenomenological and structural models. Phenomenological constitutive models are based on the fit to experimental mechanical response data, which makes them usually conceptionally simple and easy to compute. They represent the material behaviour, but are, because fitted to data, only capable to describe one loading state, not the load-dependent behaviour that soft tissues usually show. The set of material parameters does not carry any physical meaning and the parameters are usually strongly coupled. Hence reproducibility is not given. [4, 21]

Several early models were based on the inappropriate assumption of linear isotropic elasticity. In 1987 Humphrey & Yin proposed the first anisotropic model that was invariant-based and took into account the fibre structure by including the invariants I_1 and I_4 into their equation (Equation 4-3). The first term describes the behaviour of isotropic tissue, the second the energy stored in fibres. With this formulation a variation between isotropic and transversely isotropic behaviour is possible. [21]

Equation 4-3

$$W = c \{ \exp[b(I_1 - 3)] - 1 \} + A \left\{ \exp \left[a(\sqrt{I_4} - 1)^2 \right] - 1 \right\}$$

Subsequent work of Guccione et al. 1991 [22] and Humphrey et al. 1990 [22] included several transversely isotropic models, which took account for the key mechanical properties but not for the orthotropic character of myocardium. One of the first orthotropic constitutive models was introduced by Hunter et al. [23] in form of a pole-zero model that included eighteen parameters. Other orthotropic models are for example the Fung-type strain-energy function proposed by Costa et al. 2001 [24], which has seven material parameters or the exponential Fung-type strain-energy function proposed by Schmid et al. 2006 [25]. Most of the developed models rely on phenomenological descriptions of the fibre structure but their material parameters lack a clear physical meaning. [4]

Equation 4-4 shows the approach of Costa et al. Although the E_{ij} terms represent the orthotropic behaviour of myocardium the b_{ij} parameters lack physical meaning. [24]

Equation 4-4

$$W = \frac{1}{2}a(\exp Q - 1)$$

where

$$Q = b_{ff}E_{ff}^2 + b_{ss}E_{ss}^2 + b_{nn}E_{nn}^2 + 2b_{fs}E_{fs}^2 + 2b_{fn}E_{fn}^2 + 2b_{sn}E_{sn}^2$$

The second type of constitutive models are structural models. They are based on the attempt to incorporate structural parameters of the myocardium into the equation. Hence a more adequate description of the material is possible, including load-dependent responses. However, in existing models parameters are still correlated to each other and hence no uniqueness of the solution is given. Structural models can be further divided into ‘Holzapfel type’ and ‘mixture theory’ models. An overview is given in Table 4-1.

An alternative to the invariant based approach was presented by Lanir et al. in 1987 [26]. They assumed that the total strain energy of a tissue is the sum of individual fibre strain energies that are linked through appropriate tensor transformations from fibre to global coordinates. They postulate that collagen fibres in the myocardium form two distinct networks: transverse collagen bundles that interconnect with muscle fibres (perimysial collagen) and collagen fibres that are parallel to muscle fibres. Muscle and collagen fibres are embedded in a fluid matrix and the passive stiffness is assumed to be only due to collagen fibres. Furthermore they claim that the overall constitutive behaviour of myocardium is defined by the mechanical properties of collagen and muscle fibres, the structure of myocardial tissue, i.e. the distribution of fibres and the behaviour of the fluid matrix.

Since uniaxial loading of a passive muscle results in a nonlinear relation between the extension ratio and the passive tensile stress, fibres are assumed to follow a similar material law as passive muscles, since they are considered to be undulated first and then gradually straightened (see [27]) (Equation 4-5).

Equation 4-5

$$T_c = \begin{cases} D(e^{c(\alpha_c - \alpha_r)} - 1)\alpha_c, & \alpha_c > \alpha_r \\ 0, & \alpha_c \leq \alpha_r \end{cases}$$

where C and D are material parameters of the fibre, α_c the extension ratio of a fibre and α_r , the largest extension ratio without stress.

The mechanical response of one myocardial fibre is described by active properties (Equation 4-6).

Equation 4-6

$$T_m = B \left(1 - \frac{(\alpha_m - \alpha_0)^2}{(\alpha_z - \alpha_0)^2}\right) \cdot \left(1 - \frac{\beta}{\beta_{max}}\right) \cdot \alpha_m \cdot f(t^*)$$

The generated force of one muscle fibre depends on the sarcomere length (first part of the equation), the velocity of shortening (second bracket) and the time since the onset of activation $f(t^*)$. α_0 stands for the optimal extension ratio (maximal active force), α_m for the stretch of a muscle fibre and α_z represents the extension ratio with zero force. Local stress tensors due to e.g. one parallel collagen fibre and one muscle fibre are given, respectively, by

Equation 4-7

$$(\Delta T_{cp})_{11} = T_c (\bar{e}_l \cdot \bar{n}_{cp})^2, \text{ all other components zero}$$

Equation 4-8

$$(\Delta T_m)_{11} = T_m (\bar{e}_l \cdot \bar{n}_m)^2, \text{ all other components zero}$$

where \bar{e}_l is a vector parallel to the local fibre direction in the deformed state and \bar{n}_m an unit vector in direction of the deformed fibre. The overall stress is calculated by summing up the contributions to stress of all individual fibres.

Earlier Lanir et al. [27] proposed theoretical framework for constitutive equations for fibrous tissues such as the skin, where the above mentioned idea of undulated fibres was developed. They assume that fibres show undulation in a varying degree, that they are gradually recruited under tension and then rotate and stretch. They propose a density distribution function $R_k(U)$ with U being the unit vector tangent to the fibre. With that $R_k(U)\Delta\Omega$ describes the fractions of fibres of type k that are oriented in the direction of U and occupy a spatial angle Ω . Lanir et al. assume a fluid matrix, that develops hydrostatic pressure as long as it flows. The flow is stopped when the forces binding the matrix to the fibres counteract the hydrostatic pressure. The undulation is defined by an undulation density distribution function D(X).

Sacks et al. [28] use the above described framework to establish a constitutive model for planar collagenous tissues incorporating fibre orientation. The fibre orientation is obtained by using small angle light scattering (SALS). The obtained data is directly incorporated into a structural constitutive model. SALS is a

technique in which Helium-Neon laser light is passed through a specimen. Since the wavelength is within the order of magnitude of the fibre diameter the spatial intensity distribution is directly related to the fibre distribution and a statistical fibre distribution function $R(\theta)$ can be defined.

In the proposed model fibre recruitment, linear elastic properties, the collagen volume fraction and uncramping are taken into account. The gradual recruitment of fibres with the fibre strain ε is simulated by $D(\varepsilon_s)$, i.e. a statistical distribution of the fraction of fibres fully stretched between ε and $\varepsilon + \Delta\varepsilon$. The stress generated in the direction of one fibre is then defined by Equation 4-10, with K incorporating the fibre volume fraction.

Equation 4-9

$$D(\varepsilon_s) = \frac{1}{\beta^\alpha \Gamma(\alpha)} \varepsilon_s^{\alpha-1} \exp\left(-\frac{\varepsilon_s}{\beta}\right)$$

Equation 4-10

$$T_{11}^f = K \int_0^\varepsilon D(x) \frac{\varepsilon - x}{1 + 2x} dx$$

$D(\varepsilon_s)$ is approximated by a gamma distribution. In this model three material parameters have to be defined: K , α and β .

The strain energy function is defined below with $w(\varepsilon)$ being the strain energy function of one fibre.

Equation 4-11

$$W = \int_{-\pi/2}^{\pi/2} R(\theta) w(\varepsilon) d\theta$$

Hence the second Piola-Kirchhoff stress tensor can be described by

Equation 4-12

$$\mathbf{T} = \int_{-\pi/2}^{\pi/2} R(\theta) T_{11}^f(\varepsilon) [N \otimes N] d\theta$$

The above described mixture theory approaches are all rather complicated and computationally expensive. Furthermore there is not detailed enough data available to e.g. take the overall fibre distribution into account.

Holzapfel and Odgen [4] introduced in 2009 a structurally based orthotropic relation based on work of Humphrey & Yin [21] to describe passive myocardium (Equation 4-13).

Equation 4-13

$$\bar{W} = \frac{a}{2b} \exp[b(I_1 - 3)] + \sum_{i=f,s} \frac{a_i}{2b_i} \{\exp[b_i(I_{4i} - 1)^2] - 1\} + \frac{a_{fs}}{2b_{fs}} [\exp(b_{fs}I_{8fs}^2) - 1]$$

with quasi-invariants described as follows:

Equation 4-14

$$I_1 = \text{tr}(\mathcal{C}), I_{4f} = f_0 \cdot (\mathcal{C}f_0), I_{4s} = s_0 \cdot (\mathcal{C}s_0), I_{8fs} = f_0 \cdot (\mathcal{C}s_0)$$

where $f_0 = [1 \ 0 \ 0]^T$ and $s_0 = [0 \ 1 \ 0]^T$.

The transversely isotropic I_{4f} and I_{4s} terms describe the contribution from fibre and sheet directions. They contribute to the stored energy when their directions are under tension. However, since fibres do not support compression the terms are zero if $I_{4s} \leq 1$ or $I_{4f} \leq 1$. I_1 incorporates the material response of the isotropic matrix and incorporates the sheet-normal response with that. The orthotropic I_{8fs} term describes the coupling between fibre and sheet direction. The constants a , a_i , b , b_i , a_{fs} and b_{fs} are positive constitutive parameters. The ‘ a ’ parameters carry the unit of stress [kPa] whereas the ‘ b ’ parameters are dimensionless. Although this equation is capable of accounting for the orthotropic material behaviour the constants still lack a clear physical meaning. Furthermore it is impossible to isolate the mechanical response along each of the directions, since the normal direction is incorporated in the I_1 invariant. [4]

Approaches that incorporate parameters which are directly related to mechanical or structural properties of the myocardium would give a more robust and biophysically meaningful constitutive relation. E.g. variations in material properties could be more directly interpreted in terms of their effect on the mechanical behaviour. [11]

A variation of Holzapfel’s equation was attempted by Wang et al. in 2013 [29] by taking residual stresses into account. They claim that accounting for residual stresses may be important in models that describe remodelling, because remodelling could act to set up and maintain residual stresses. They define an initial Cauchy-Stress τ in a reference configuration B_r . If traction vanishes τ becomes a residual stress. Since the strain-energy function depends on τ and invariants I_i as well as the Cauchy-Stress σ they introduce additional Invariants I_{6-9} which are dependent on the Cauchy-Green deformation Tensor \mathcal{C} and τ (Equation 4-15).

Equation 4-15

$$I_6 = \text{tr}(\tau\mathcal{C}), I_7 = \text{tr}(\tau\mathcal{C}^2), I_8 = \text{tr}(\tau^2\mathcal{C}), I_9 = \text{tr}(\tau^2\mathcal{C}^2)$$

And the Cauchy-stress σ can be written in terms of those invariants as follows (Equation 4-16).

Equation 4-16

$$\sigma = -p\mathbb{I} + F \sum_{i=1,4f,4s,4fs} \frac{\partial W}{\partial I_i} \frac{\partial I_i}{\partial F}$$

In the residual-stress free configuration σ reduces to Equation 4-17

Equation 4-17

$$\tau = \frac{\partial W}{\partial F}(\mathbb{I}, \tau) - p\mathbb{I}$$

and the following relations can be derived (Equation 4-18).

Equation 4-18

$$\begin{aligned} B &= \mathbb{I}, I_1 = 3, I_{4f} = I_{4s} = 1, I_{4fs} = 0, \Sigma = \tau, I_6 = I_7 = \text{tr}(\tau), \\ I_8 &= I_9 = \text{tr}(\tau^2), 2W_1 = p = a, 2(W_6 + W_7) = 1, W_8 + W_9 = 0 \end{aligned}$$

In this simple approach Wang et al. assume small strains; hence they take only W_6 into account and state that it should be constant for simplicity. Taking Equation 4-18 into account Holzapfel's augmented equation is the following (Equation 4-19).

Equation 4-19

$$\bar{W} = \frac{a}{2b} \exp[b(I_1 - 3)] + \sum_{i=f,s} \frac{a_i}{2b_i} \{\exp[b_i(I_{4i} - 1)^2] - 1\} + \frac{a_{fs}}{2b_{fs}} [\exp(b_{fs}I_{8fs}^2) - 1] + \frac{I_6}{2}$$

In a next step Wang et al. simplify the equation by assuming that the shear components are negligible in the local coordinate system. Hence the residual stress components lie in the principal directions and can be expressed by existing invariants in Holzapfel's expression as follows.

Equation 4-20

$$\begin{aligned} I_6 &= \text{tr}(\tau C) = \tau_{ss}I_{4s} + \tau_{ff}I_{4f} + \tau_{nn}I_{4n} \\ I_7 &= \text{tr}(\tau C^2) = \tau_{ss}I_{5s} + \tau_{ff}I_{5f} + \tau_{nn}I_{5n} \end{aligned}$$

Since

Equation 4-21

$$I_1 = \text{tr}(C) = I_{4s} + I_{4f} + I_{4n}$$

I_6 can be expressed by Equation 4-22.

Equation 4-22

$$I_6 = \tau_{nn}I_1 + (\tau_{ff} - \tau_{nn})I_{4f} + (\tau_{ss} - \tau_{nn})I_{4s}$$

where τ_{ii} are the residual stresses in principal directions. [29]

Since the available data on residual stresses is very restricted, the application of the above described equation is rather complicated. Wang et al. claim that they cannot find any differences in the pressure-volume curves when incorporating residual stresses. They hypothesise that their assumption of residual stresses being due to the isotropic matrix could be wrong and hence new constitutive models are needed to take residual stresses into account. Furthermore it is not clear whether the unloaded configuration is in equilibrium as assumed or not. [29]

Eriksson et al. [30] consider in their work from 2013 the disarray in fibre and sheet orientations. They state that the fibre alignment in the healthy heart follows closely helical pathways and the angular dispersion of the directions of the fibres is rather small (12-15°), whereas the dispersion of the sheet structure is large. When it comes to a diseased heart the angular dispersion of the fibre directions reaches 65°. Eriksson et al. claim, however, that there is no data available for diseased sheet structure. To model the fibre disarray they introduce an invariant based framework that is based on an augmentation of Holzapfel's and Ogden's law [4] with a distribution function developed for fibre distribution in collagenous arteries [31]. The circular dispersion of fibres (see Fig. 4-2) is modelled by the introduction of structure tensors, defined in material coordinates shown in the following equation.

Equation 4-23

$$H_f = \kappa_f I + (1 - 3\kappa_f)(f_0 \otimes f_0), H_s = \kappa_s I + (1 - 3\kappa_s)(s_0 \otimes s_0)$$

where $\kappa_i = 0$ means perfect alignment and $\kappa_i = 1/3$ complete dispersion. κ_i can be derived from a probability density function $\rho(\theta)$ (PDF) (Equation 4-24).

The values of the PDF can be fitted against histograms of the dispersion of fibre and sheet angles as follows: First the fibre angles θ in the data are shifted to an average angle $\bar{\theta}$ by centring around $\bar{\theta} = 0^\circ$. Subsequently the maximum likelihood estimates function in MATLAB (The MathWorks Inc., Natick, USA) is used together with $\rho(\theta)$ to retrieve the parameter b with a 95 % confidence interval. Finally κ_i is estimated by Equation 4-25.

Equation 4-24

$$\rho(\theta) = 4 \sqrt{\frac{b}{2\pi}} \frac{\exp(b(\cos(\theta) + 1)}{\operatorname{erfi}(\sqrt{2b})}$$

Equation 4-25

$$\kappa_i = \frac{1}{4} \int_0^\pi \rho_i(\theta) \sin^3 \theta d\theta$$

The augmented Holzapfel and Ogden relation is now:

Equation 4-26

$$\bar{W} = \frac{a}{2b} \exp[b(I_1 - 3)] + \sum_{i=f,s} \frac{a_i}{2b_i} \{ \exp[b_i(I_{4i}^* - 1)^2] - 1 \} + \frac{a_{fs}}{2b_{fs}} [\exp(b_{fs}I_{8fs}^2) - 1]$$

Equation 4-27

$$I_{4i}^* = \kappa_i I_1 + (1 - 3\kappa_i) I_{4i}$$

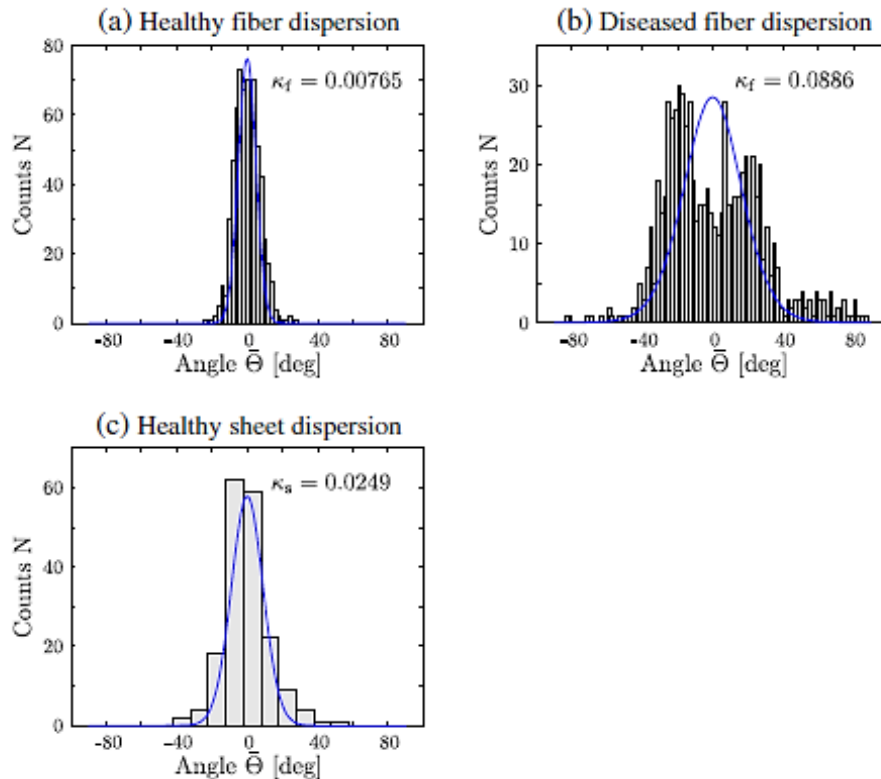


Fig. 4-1 Data acquainted from [32] and used in [30] to determine κ_i

When κ_i equals 0 the original model is retrieved. With an increased dispersion an increasingly more isotropic active and passive mechanical response is modelled because I_{4i}^* represents the blend between the isotropic invariant I_1 and the directionally dependent invariant I_{4i} . If the dispersion is large enough the preferred myocyte orientation vanishes.

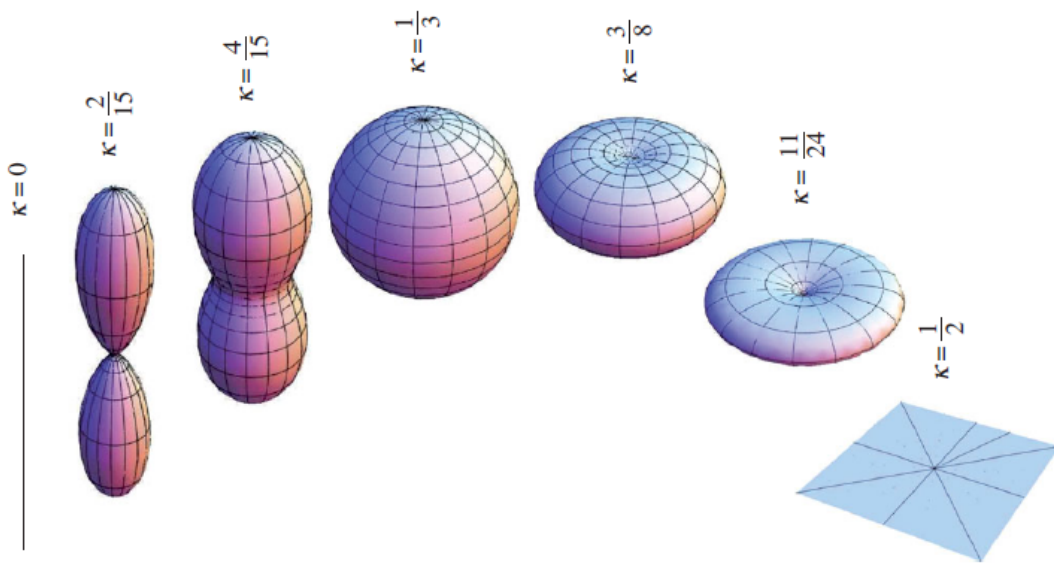


Fig. 4-2 3D graphical representation of the orientation density based on the probability density function for different values of κ [33]

Phenomenological Models	Structural Models	
Fung type	Mixture Theory	Holzapfel type
Humphrey & Yin 1987	Lanir et al. 1989	Holzapfel 2009
Guccione et al. 1991	Sacks et al. 2003	Erikson et al. 2013
Costa et al. 1996		Wang et al. 2013
Schmidt et al. 2010		
<u>Advantages</u>	<u>Advantages</u>	
<ul style="list-style-type: none"> • Easy to compute • Conceptually simple • Represent bulk material behaviour 	<ul style="list-style-type: none"> • Allow incorporation of structural parameters • Motivated by basic constituents of myocardium 	
<u>Disadvantages</u>	<u>Disadvantages</u>	
<ul style="list-style-type: none"> • Parameters have no physical meaning • Curve-fitting: non-uniqueness of parameters, coupling of parameters • Reproducibility • Inability to model remodelling 	<ul style="list-style-type: none"> • Parameter correlation • Representing basic material behaviour • Uniqueness of solution not given • Impossible to isolate mechanical response along each of the directions 	

Table 4-1 Breakdown of different classes of constitutive models

The main disadvantage of the reviewed models is that the material parameters lack physical meaning and cannot be estimated from any functional or structural data. Hence there is no uniqueness of the solution given and parameters are often coupled.

4.3 Experimental Data Sources

In the following section a summary of experimental data sources is given that are used to gain information about the geometry and kinematics, microstructure and function of the LV under healthy and HF conditions.

4.3.1 Cardiac Magnetic Resonance Imaging

The principles and physics of Magnetic Resonance Imaging (MRI) are beyond the scope of this thesis. A good overview can be found in [34]. Instead a short insight in special techniques is given subsequently.

To enable the assessment of heart function multiphase images can be acquired throughout the cardiac cycle. This technique is called CINE MRI. Dimensions of the LV that were used to create a Finite Element Model of the LV were derived from high resolution CINE MRI images. [34]

Global deformation and regional heart motion can be measured with tagged MRI. It is usually performed using spatial modulation of magnetization (SPAMM) technique. Tagged MRI saturates signals from parallel bands of tissue by combining radio frequency pulses with short gradient waveforms. These parallel bands follow the deformation of the myocardium. 3D motion of the heart can be thus reconstructed by post-processing of the tagged MR images. The final images are reconstructed from data taken over several cardiac cycles and represent the average motion of the heart. [34]

4.3.2 Dokos' Simple Shear Experiment

In 2002 Dokos et al. [35] performed simple shear experiments on pig heart muscle in order to examine shear properties of passive ventricular myocardium. Dokos et al. used a right-hand coordinate system FSN that reflects the local architecture of the myocardium: F denotes the fibre orientation, S is the transverse to the fibre and denotes the sheet direction and N is the sheet normal direction. 3x3x3 mm cubic samples were cut from the left ventricular midwall in a way that the side aligned with the coordinate system (see Fig. 4-3). [35]

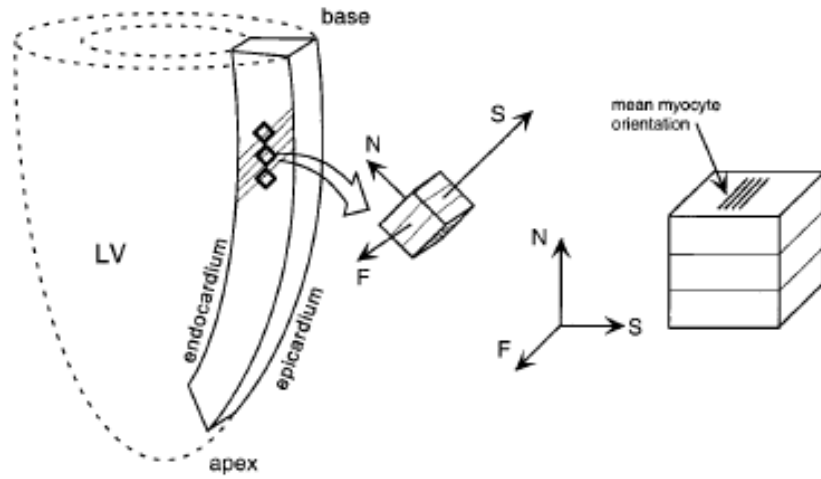


Fig. 4-3 Schematic representation of locations and orientations of samples [35]

For the experiment Dokos et al. measured the dimensions of each myocardial specimen and then applied shear deformation under quasistatic conditions. The samples were glued to upper and lower platforms that were displaced relatively to each other. Cycles of sinusoidal shear in a range from - 50 % to 50 % were applied separately to each specimen in two orthogonal directions. Force transducer at the top and the bottom recorded three dimensional forces at each displacement step. [35]

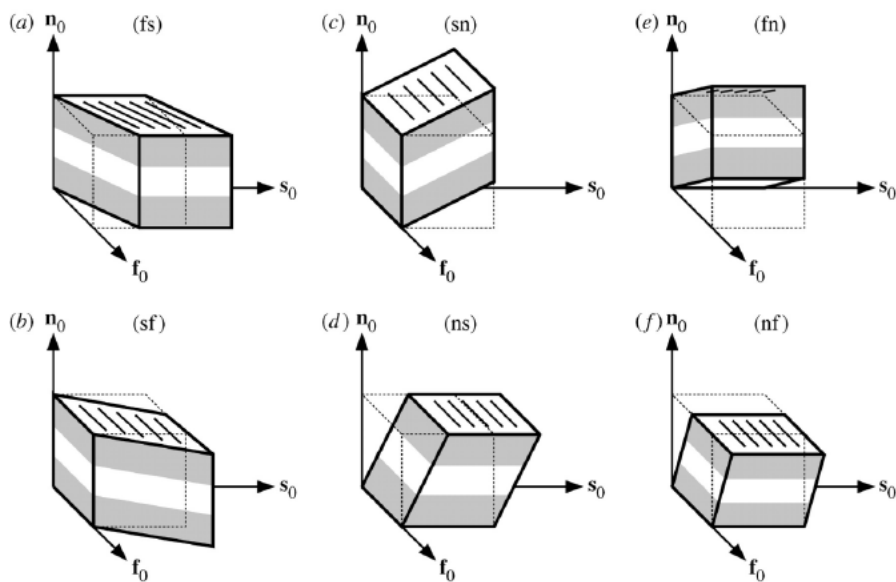


Fig. 4-4 Six possible modes of simple shear [35]

The six possible shear modes are illustrated in Fig. 4-4 where the first index represents the normal to the face onto the shear force has been applied to and the second index indicates the direction of the applied shear force. [35]

4.3.3 Extended Volume Confocal Microscopy Imaging during HF

To examine the progression of myocardial remodelling spontaneously hypertensive rats (SHRs) and Wistar-Kyoto controls (WKY) were studied by LeGrice et al. [18] at three, twelve, eighteen and twenty-four months. SHRs progress in this time through four different stages: systemic hypertension, diastolic dysfunction, early systolic failure and decompensated heart failure.

Extended volume confocal microscopy imaging (EVCM) was used to reveal myocyte and collagen microstructure, variation of myocyte direction, collagen fraction and the degree of laminar fusing.

WKY rats showed an ordered laminar arrangement of myocytes throughout all ages. SHR rats had a corresponding perimysial collagen arrangement at three months, but it changed rapidly from twelve months onwards. Perimysial collagen surrounding muscle layers fused with collagen interconnecting these to form distinct sheets at twelve months, although perimysial collagen fraction remained unchanged with age in both groups. Endomysial collagen density changed in both groups but more significantly in SHRs. Global collagen fraction increased as well in both groups with a less pronounced increase in WKY rats. Myocyte cross-section dimensions were similar in both groups at three months, however, while there was little variation with age at WKY rats, striking changes could be seen at SHRs. Median myocyte cross section area increased between three and twelve months and remained increased with a wider variation at eighteen and twenty-four months. Additionally the number of myocytes per layer increased at SHRs significantly at eighteen and twenty-four months, whereas WKY rats showed three to four layers of myocytes per sheet throughout time. [18]

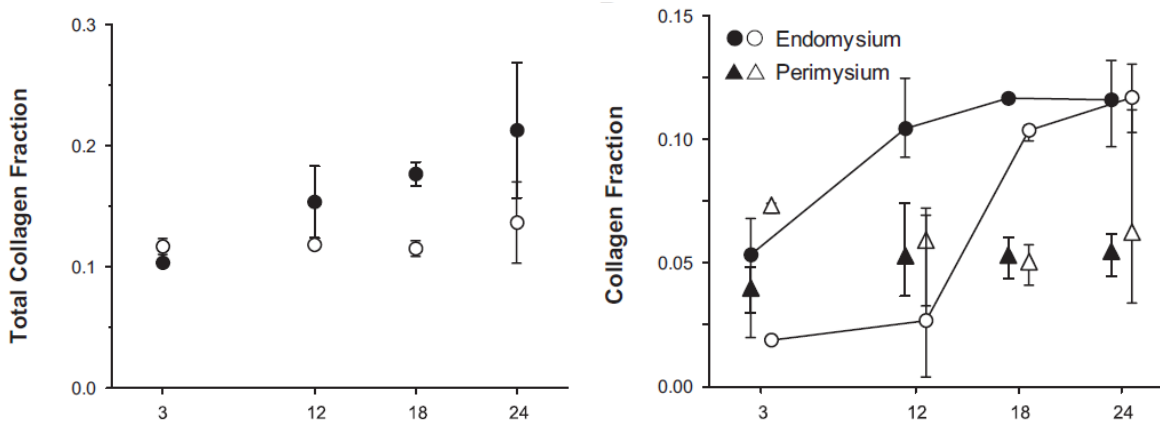


Fig. 4-5 collagen fractions for SHRs (filled symbols) and WKY rats (open symbols) [18]

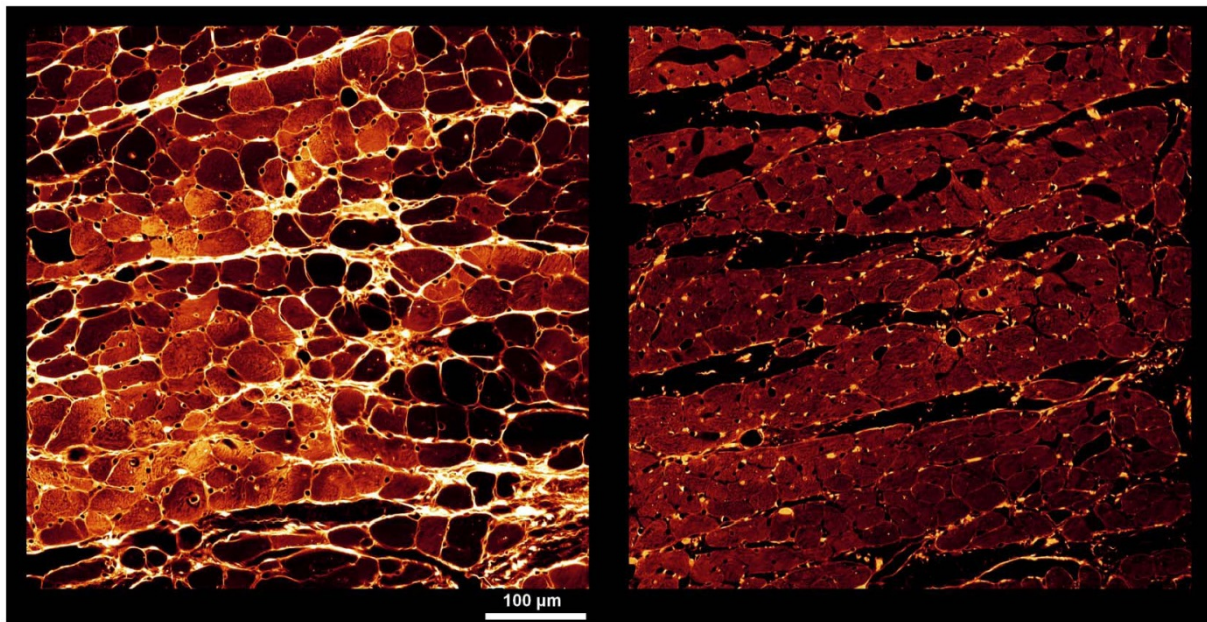


Fig. 4-6 High resolution images from LV midwall at 12 months from a SHR (left) and WKY rat (right) [18]

The most significant differences between WKY rats and SHRs could be seen in the associated collagen framework (see Fig. 4-6). In WKY rats perimysial collagen cords connected adjacent muscle layers loosely allowing these structures to separate during movement. In SHRs in contrary these structures were fused and thickened, giving the impression that the connective tissue matrix was more rigid in SHRs than in WKY rats. The density of type I collagen was more than twice as great in SHRs than in the age-matching WKY controls at twenty-four months, because it was increasingly expressed in the thickened perimysial collagen between layers of myocytes. Although earlier findings suggested that the subsequent development of systolic heart failure is caused by reversal of profibrotic processes this could not be confirmed. Type I collagen in the perimysial network even increased with age hence the progression to systolic heart failure can be better explained by an on-going reorganization of the extracellular matrix scaffold. [18]

4.3.4 Ex-vivo pressure

To be able to compare LV function throughout different stages of heart failure LeGrice et al. [18] characterized the LV pressure-volume relationship for WKY rats and SHRs. The heart was arrested, attached to a Langendorff apparatus and a balloon catheter was inserted into the LV. The balloon was fabricated such that its undeformed volume was greater than that of the LV cavity. It was inflated to a maximum pressure of 30 mmHg by plunging fluid to the balloon, deflated and

pressure was measured via a side port in the balloon catheter. The displaced volume was estimated by the position of the plunger. [18]

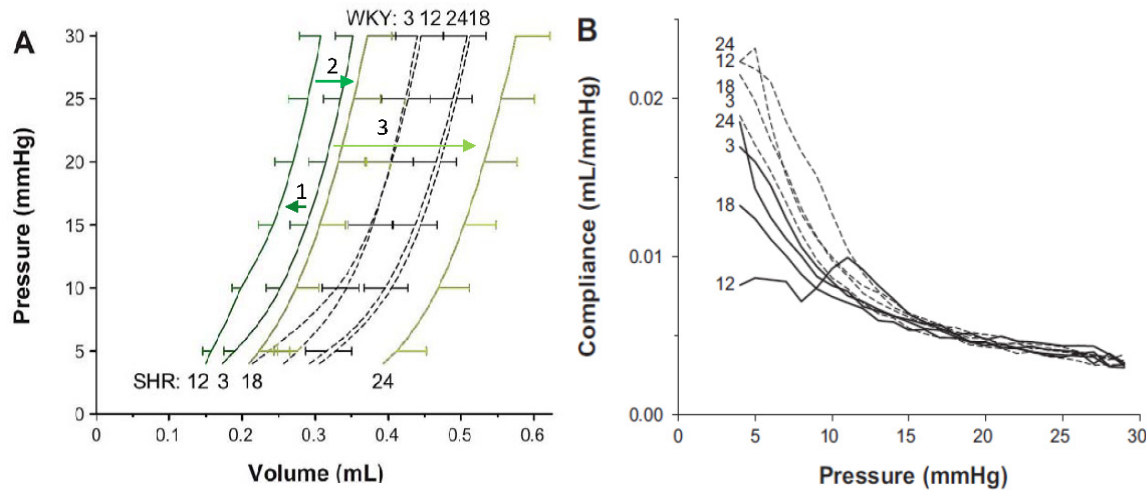


Fig. 4-7 PV (left) and Compliance-Pressure curves (right) for SHRs (solid lines) and WKY rats (dashed lines) [18]

Fig. 4-7 illustrates the Pressure-volume (PV) and Compliance-Pressure curves for SHRs and WKY rats. Curves for SHRs lie to the left of WKY controls at three, twelve and eighteen months and shift to the right at twenty-four months. This could be explained by the LV dilatation associated with heart failure. For filling pressures up to 15 mmHg passive LV compliance is smaller for all SHRs compared to WKY rats, but varies with age. It was reduced at twelve months and increased afterwards. [18]

4.4 Summary of Structural Changes

In this section an overview over structural changes that can be theoretically incorporated into the novel constitutive model is given. Table 4-2 shows an overview over changes in myocyte geometry, PV-curves and structure of collagen.

The most striking difference can be seen in the collagen structure. On the one hand endomysium (orange lines) was observed to fuse with the longitudinal chords of perimysium (green lines, see Fig. 4-8). [18]

On the other hand convoluted fibres of perimysium (black lines) that interconnect muscle layers fused with the meshwork of perimysial collagen surrounding layers of myocytes (violet). In total the ECM seemed to become more dense. [18]

With on-going disease, the fibre and sheet direction become less distinct and the overall response of myocardium seems to be much stiffer (PV- and compliance-curves). [18]

In summary it can be said that the healthy case shows distinct directions of perimysial collagen. The shearing of sheets is only restricted by the sheets themselves and the branches of perimysial collagen between them. During the progression to diastolic HF (fibrosis) thick perimysial collagen planes in the sheet direction are formed and endomysial collagen fuses with longitudinal chords of perimysial collagen.

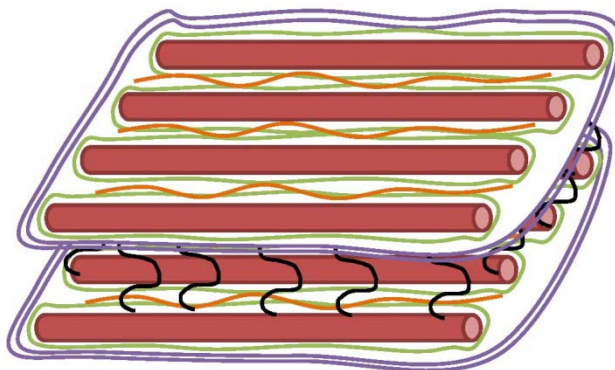


Fig. 4-8 Schematic sketch of the structure of myocardium. Perimysial collagen surrounding layers of myocytes (violet), longitudinal cords of perimysial collagen within layers (orange), perimysial collagen interconnecting adjacent muscle layers (black), endomysial collagen surrounding individual myocytes (green) and myocytes (red)

With progression to systolic HF (disorder) the sheets that have been formed by fusing perimysial collagen become less ordered, the PV-curves shift to higher volumes and become more compliant. However, fibre and normal direction remain fused with a steady volume fraction of endomysial and perimysial collagen.

	Myocytes		PV-Curves		
				<u>Endomyssial</u>	<u>Perimysial</u>
Fibrosis	<ul style="list-style-type: none"> • myocyte cross-section area increased in median and range • space occupied by cleavage planes decreased • more myocytes per layer • number of muscle layers reduced at 12 - 18 months 	<ul style="list-style-type: none"> • 3, 12 and 18 months shifted to left of WKY • compliance reduced at 12 months 	<ul style="list-style-type: none"> • increase in collagen fraction and thickening • fusion with longitudinal cords of perimysial collagen 	<ul style="list-style-type: none"> • convoluted fibers connecting adjacent muscle layers interconnect with meshwork surrounding layers of myocytes, forming distinct sheets • hypertension triggers synthesis of Type I collagen 	
Dispersion	<ul style="list-style-type: none"> • cross-section remained elevated, range increased 	<ul style="list-style-type: none"> • left-shift at 18 months, substantial shift to right of WKY at 24 months • compliance increased 		<ul style="list-style-type: none"> • fused and thickened to form planes • more dispersed, less ordered 	<ul style="list-style-type: none"> • type I collagen fraction more than twice as high as in WKY 24 months

Table 4-2 Summary of structural changes during diastolic HF (Fibrosis) and systolic HF (Dispersion), adapted from [18]

5 Modelling Framework

Mathematical methods used to estimate material parameter sets as well as modelling methods to examine the local and global stress-strain behaviour are summarised in this section.

5.1 Material Parameter Estimation

Whenever an equation is modified in its fundamental shape material parameters have to be estimated. They are optimized by fitting the model predicted shear stress (see section 5.2) to Dokos' simple shear experimental data (see section 4.3.2).

For this optimisation problem a weighted least-squares objective function was chosen, which resembles the L^2 -norm ($\|\mathbf{x}\|_2 = \sqrt{\sum_{k=1}^n |x_k|^2}$) of the error between experimental data and the model prediction. Since Dokos et al. estimated force-displacement data, analytic forces \mathbf{t}_{ana} are derived by means of Nanson's formula from the 2nd Piola Kirchhoff Stress Tensor ([36], p.75) to be compared with the measured force on the top face of the experiment \mathbf{t}_{exp} . For each mode the experiments provides approximately 250 data points over the range of deformations from $(-1/2)\gamma$ to $(1/2)\gamma$. [37]

Usually an objective function Ω defined by a conventional least-squares method would be obtained by summation over all six shear modes, two directions of the top face force and over all data points. This would result in approximately 3000 data points (see Equation 5-1).

Equation 5-1

$$\Omega(\boldsymbol{\vartheta}) = \frac{1}{2} \sum_{modes} \sum_{\substack{x,z \\ force points}} \sum_{data} [\mathbf{t}_{ana}(\boldsymbol{\vartheta}) - \mathbf{t}_{exp}]^2 \Delta x \approx \frac{1}{2} \sum_{modes} \sum_{\substack{x,z \\ force}} \int_{-1/2\gamma}^{1/2\gamma} [\mathbf{t}_{ana}(\boldsymbol{\vartheta}) - \mathbf{t}_{exp}]^2 dx$$

where $\boldsymbol{\vartheta}$ is the vector over all material parameters and Δx is a weighting such that the integrals form a L^2 -norm and serve as a measure for the length of the error.

To reduce the computational time the objective function is approximated by a Gaussian quadrature approach that evaluates the function at the zeros of the Legendre polynomials (see Equation 5-2). [37]

Equation 5-2

$$\Omega^G(\boldsymbol{\vartheta}) = \frac{1}{2} \sum_{\substack{\text{modes} \\ \text{force}}} \sum_{x,z} \sum_{j=1}^G \omega_j [\mathbf{t}_{ana}(\boldsymbol{\vartheta}, x_j) - \mathbf{t}_{exp}(x_j)]^2$$

where G is the number of Gaussian quadrature points and ω_j the respective weights. This modification reduces the initial ~ 3000 equations to 144, if e.g. $G = 12$ was chosen and hence corresponds to 95 % saving in computational time. [37]

5.2 Simulation of Simple Shear

To understand the impact of a new constitutive model on the mechanical behaviour in three material directions simulations on a single cube are undertaken. This helps to understand how the material behaviour is influenced by alterations in constitutive relations.

Simple shear in six different modes is simulated for a shear strain amount of 0.5. The obtained stress values are compared to stress values found by Dokos' simple shear experiments on symmetric 3x3x3 mm cubes (see section 4.3.2) [35].

The Green's strain tensor components corresponding to the six modes of modes of shear can be derived as follows:

Equation 5-3

$$\begin{aligned} E_{NS} &= \begin{pmatrix} 0 & 0 & 0 \\ 0 & 0 & 0.5k \\ 0 & 0.5k & 0.5k^2 \end{pmatrix} & E_{NF} &= \begin{pmatrix} 0 & 0 & 0.5k \\ 0 & 0 & 0 \\ 0.5k & 0 & 0.5k^2 \end{pmatrix} \\ E_{SN} &= \begin{pmatrix} 0 & 0 & 0 \\ 0 & 0.5k^2 & 0.5k \\ 0 & 0.5k & 0 \end{pmatrix} & E_{SF} &= \begin{pmatrix} 0 & 0.5k & 0 \\ 0.5k & 0.5k^2 & 0 \\ 0 & 0 & 0 \end{pmatrix} \\ E_{FN} &= \begin{pmatrix} 0.5k^2 & 0 & 0.5k \\ 0 & 0 & 0 \\ 0.5k & 0 & 0 \end{pmatrix} & E_{FS} &= \begin{pmatrix} 0.5k^2 & 0 & 0.5k \\ 0.5k & 0 & 0 \\ 0 & 0 & 0 \end{pmatrix} \end{aligned}$$

where k denotes the amount of shear [35].

5.3 Simulation of Axial Extension

Three modes of axial extension are simulated, shown in Fig. 5-1 to examine axial behaviour. The green cube represents the undeformed state, whereas the deformed states are represented by a green cube for an extension in fibre direction, yellow in sheet and blue in normal direction. The red arrows embody the fibre orientation. Because of the incompressibility constrain of myocardium each uniaxial extension has to be paralleled by a uniaxial compression, so that Green's shear tensor has two entries for each mode. A strain amount of 0.2 is applied in each direction, respectively and the strain values are estimated for each strain increment.

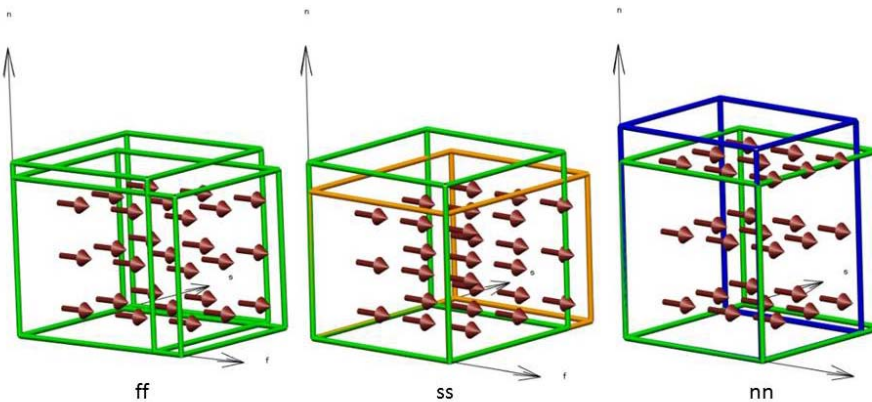


Fig. 5-1 Illustration of the three modes of axial extension

5.4 Finite Element Modelling of Passive Filling

To model passive filling a FE model is set up. It consists of a single element and hence keeps computational times for the simulation low. The internal pressure during passive filling is applied homogeneously on the endocardial surface of the LV model. It is increased in small increments until either 30 mmHg (simulation of passive filling) or 15 mmHg (for the parameter estimation, see section 5.6) is reached.

To model the LV of a rat in the first instance a single element, thick-walled, truncated axisymmetric prolate spheroid model defined by four nodes is used. Each point of this model is defined by the orthogonal coordinates λ , μ and θ . However, for the performance of the mechanics analysis it is more reliable to set up the model in a Cartesian coordinate system [2]. The transformation between Cartesian coordinates x , y and z and prolate spheroidal coordinates λ , μ and θ is shown in Equation 5-4.

Equation 5-4

$$x = f \sinh(\lambda) \sin(\mu) \cos(\theta)$$

$$y = f \sinh(\lambda) \sin(\mu) \sin(\theta)$$

$$z = f \cosh(\lambda) \cos(\mu)$$

where f denotes the focal length, λ represents the radial coordinate, μ represents the longitudinal (angle) coordinate and θ denotes the circumferential coordinate.

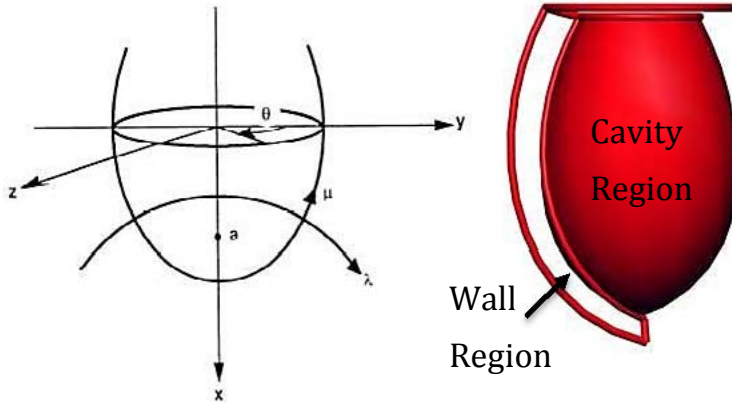


Fig. 5-2 Prolate spheroid geometry with 'a' denoting the focal length (left) [38] and FE model of the LV in undeformed configuration

To implement this model in CMISS, two regions are defined: LV cavity (representing the LV chamber) and LV wall (region surrounding the chamber). The wall region contained fibres, varying transmurally from -60° at the epicardial surface to $+70^\circ$ at the endocardial surface (see Fig. 5-3, right). The sheet angle was set to be $+30^\circ$, according to data from [1] (see Fig. 5-3, left).

Cavity volumes for the prolate spheroid geometry can be calculated using Equation 5-5 and the equatorial wall thickness is calculated by transformation of Nodal coordinates into Cartesian coordinates and calculating the distance between inner and outer nodes at $\mu = 90^\circ$.

Equation 5-5

$$Vol(\lambda) = \frac{4}{3}\pi f^3 \cos(\lambda) (\sin(\lambda))^2$$

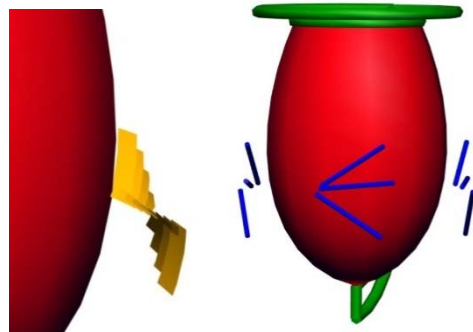


Fig. 5-3 Visualisations of sheet (left) and fibre orientation (right) varying throughout the wall region

5.5 Subject Specific Geometry Fitting

LV model dimensions for the FE model for SHRs and WKY rats of different ages are obtained from CINE MRI along short- and long-axis. This data is processed via the CIM (Cardiac Image Modeller) software package which generates a sixteen element FEM model by tracing epicardial and endocardial boundaries throughout the cardiac cycle (see Fig. 5-4, left). For the purpose of passive inflation simulation the frame at diastasis (see section 3.2) was chosen, as it is assumed that neither active contraction nor passive stretch of the myocardium takes place in this stage.

To convert the obtained FEM model to a CMISS model, surface points are generated using cmgui (see Fig. 5-4, middle). Subsequently the prolate spheroid geometry (see section 5.4) is fitted to obtained surface points in two steps: in the first step the epicardial surface is fitted to epicardial surface data points, in the second step the endocardial surface is fitted to endocardial surface data points (see Fig. 5-4,right).

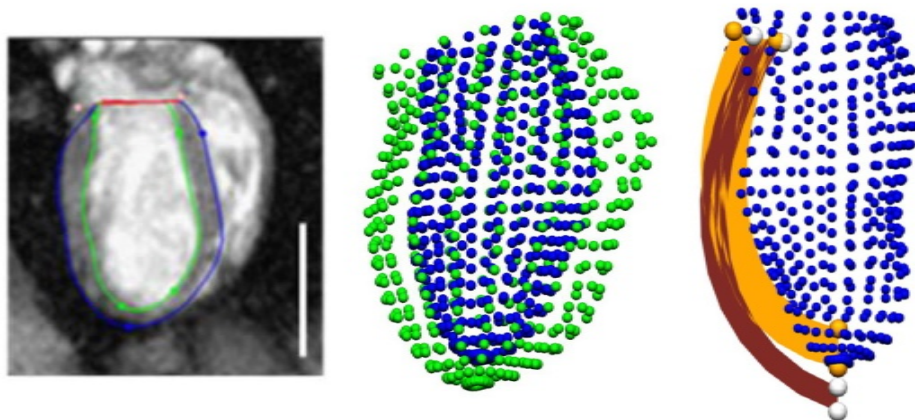


Fig. 5-4 CIM processing of MRI data, long-axis view (left), surface points generated with cmgui (middle) and single element endocardial surface points with unfitted (red) and fitted (yellow) wall region

5.6 Subject Specific Parameter Estimation

During the multivariate optimisation described in section 5.1 parameters are fitted to Dokos' data that was obtained by shearing ex vivo cubes of dead tissue. To be able to fit subject specific parameters of the modified equations to PV-data which is obtained by inflating a living heart as described in section 4.3.4 a second, bivariate optimisation is undertaken as follows.

Initially fitted ' a ' and ' b ' parameters obtained by a multivariate optimisation described in section 5.1 are taken and modified by two global scaling factors ' M '

and ‘ N ’, applied as shown in Equation 5-6. This approach maintains the anisotropic mechanical response captured by Dokos’ shear experimental data by fixing the parameter magnitudes relative to each other.

Equation 5-6

$$\bar{W} = M \left(\frac{a}{2Nb} \exp[Nb(I_1 - 3)] + \sum_{i=f,s} \frac{a_i}{2Nb_i} \{ \exp[Nb_i(I_{4i} - 1)^2] - 1 \} + \frac{a_{fs}}{2Nb_{fs}} [\exp(Nb_{fs}I_{8fs}^2) - 1] \right)$$

The parameters input to CellML and CMISS become:

$$[Ma_f \ Ma_{fs} \ Ma_n \ Ma_s \ Nb_f \ Nb_{fs} \ Nb_n \ Nb_s]$$

‘ M ’ and ‘ N ’ are then fitted to experimental PV-Data of the WKY rat. This results in a novel parameter set used further with SHRs.

For the bivariate optimisation a least-squares objective function is chosen to be the L^2 -norm ($\|\mathbf{x}\|_2 = \sqrt{\sum_{k=1}^n |x_k|^2}$) of the error between experimental volumes and model prediction for a given range of pressures. The Levenberg-Marquardt algorithm is used to minimise the objective function.

The optimisation framework is established in MATLAB solving iteratively the prolate spheroidal LV model in the CMISS framework. Five different initial estimates for ‘ M ’ and ‘ N ’ parameters are tested to make sure that obtained ‘ M ’ and ‘ N ’ parameters resemble the optimum. Initial guesses are [1 1], [1.5 1], [1 1.5], [0.5 1] and [1 0.5]. Updated parameter estimates are input into the CellML file and pressure-volume data as output is returned. The iteration is repeated until either the value of the objective function or the size of changes in each parameter falls below tolerances of $1 \cdot 10^{-7}$ or $1 \cdot 10^{-6}$, respectively. The L^2 -norm of the objective function (*resnorm*) provides an indication of goodness of fit. The optimisation framework can be found in Appendix 3A and an overview is given in the flowchart (Fig. 5-5).

LV model dimensions for the FE model for SHRs and WKY rats of different ages are obtained from CINE MRI as described in section 4.3.1, whereas experimental PV data for the fitting is obtained as described in section 4.3.4.

All measured volumes under ex-vivo conditions are much smaller than those obtained using MRI imaging. It is assumed that experimental volume data has been underestimated. The volume discrepancies could be due to the balloon being prevented to fit perfectly to LV walls. Also elastic recoil of the balloon

material could provide extra resistance and calibration errors may occur. Experimental volumes are adjusted by an offset which is determined from volumes at the end diastolic pressure of 6 mmHg [39].

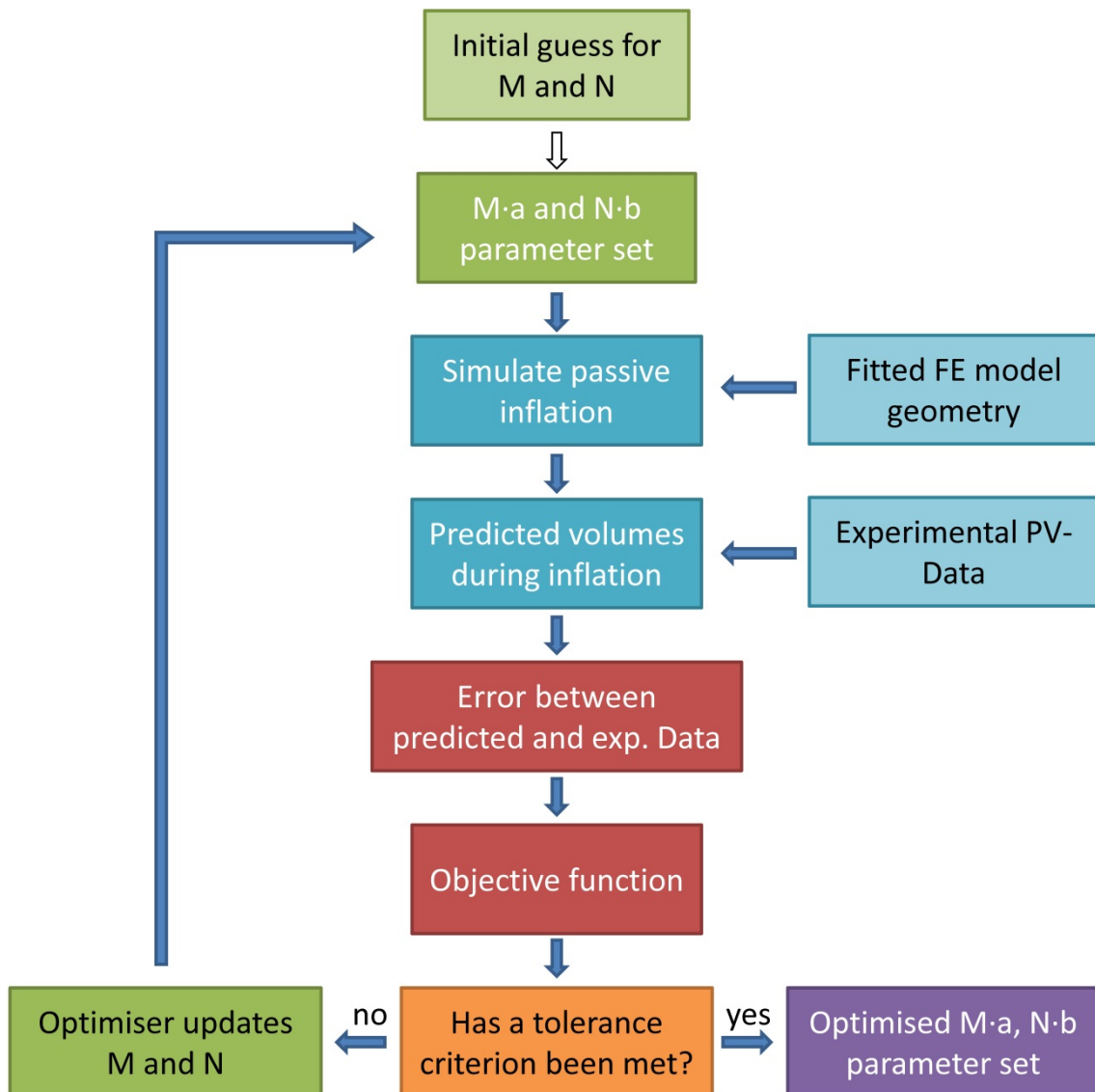


Fig. 5-5 Flowchart summarising the Bivariate optimisation, blue arrows mark the main optimisation process

Although PV-Data up to a pressure of 30 mmHg is available, fitting is undertaken only for filling pressures up to 15 mmHg for following reasons. The most significant differences in slope of the PV-curves (a measure for compliance) can be found for filling pressures <10 mmHg. At pressures higher than 15 mmHg differences in slope become insignificant between ages or species. Furthermore, a typical maximum diastolic filling pressure is ~7 mmHg for 11 month WKY rats [39].

6 Constitutive Equations for Heart Failure Mechanics

The modifications made to the Holzapfel equation in order to develop a more structural based model that can take heart failure mechanics into account are described in this section. All described equations were subsequently analysed in their local and global behaviour. The implementations into CellML will be published on the CellML.org model repository.

6.1 Augmented Holzapfel Equation

As a first approach to incorporate increasing sheet dispersion with progression towards systolic heart failure, Holzapfel's equation augmented with a κ_s parameter (Equation 6-1) [40] was chosen.

Equation 6-1

$$\begin{aligned} \bar{W} = & \frac{a}{2b} v \exp[b(I_1 - 3)] + \frac{a_f}{2b_f} \{\exp[b_f(I_{4f} - 1)^2] - 1\} + \frac{a_s}{2b_s} \{\exp[b_s(I_{4s}^* - 1)^2] - 1\} \\ & + \frac{a_{fs}}{2b_{fs}} [\exp(b_{fs}I_{8fs}^2) - 1] \end{aligned}$$

where

$$I_{4s}^* = \kappa_s I_1 + (1 - 3\kappa_s) I_{4s}$$

To implement the constitutive equation into CellML it was required to rewrite the constitutive equation in terms of the Green's strain tensor components (see section 4.1). The 2nd Piola Kirchhoff stress tensor was calculated (see **Appendix 1A**) and implemented into CellML using the software interface OpenCell (<http://www.cellml.org>).

Usually Equation 6-2 is the general form for a constitutive relation for passive myocardium.

Equation 6-2

$$\mathbf{T}^{MN} = \frac{1}{2} \left(\frac{\partial W}{\partial E_{MN}} + \frac{\partial W}{\partial E_{NM}} \right) - p \frac{\partial X_M}{\partial x_k} \frac{\partial X_N}{\partial x_k}$$

In this approach only the first term was considered since Dokos' data does neither take neither hydrostatic pressure nor contractile stress into account. Hence the obtained stress for this and all following modifications was calculated by

Equation 6-3

$$\mathbf{T}^{MN} = \frac{1}{2} \left(\frac{\partial W}{\partial E_{MN}} + \frac{\partial W}{\partial E_{NM}} \right)$$

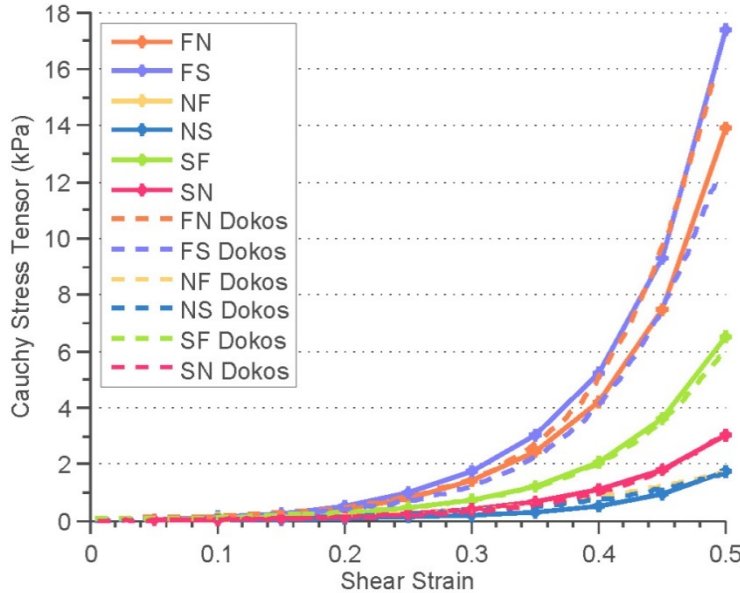


Fig. 6-1 Shear Stress/Strain Curve using Holzapfel's Equation augmented with $\kappa = 0$. (dashed lines are experimental results; solid lines represent the model fit using Wang's parameter set [41])

Material parameters used are summarised in Table 6-1 and are taken from [4] and [41]. As concluded in previous work [42] Wang's parameter set appears to be the best fit to Dokos data, since all estimated curves aligned well to the experimental data. It has to be noted that Holzapfel et al. [4] incorrectly swapped the labels for FS and FN curves, assuming that Dokos had mislabelled the data. This swap can be seen in Fig. 6-1.

a [kPa]	b	a_f [kPa]	b_f	a_s [kPa]	b_s	a_{fs} [kPa]	b_{fs}	
0.059	8.023	18.472	16.026	2.481	11.120	0.216	11.436	[4]
0.236	10.8	20.0	14.2	3.72	5.16	0.411	11.3	[41]

Table 6-1 Summary of used material parameters: Holzapfel [4] and Wang [41]

To validate the implementation calculated stresses by the CellML-CMISS coupled model and a direct MATLAB implementation were compared and found to be

identical. Additionally the 2nd Piola Kirchhoff Stress Tensors of the CellML implementation of Holzapfel's equation [4] was compared to the new implementation of the augmented equation for $\kappa_s = 0$ since the equations should be identical in a case of perfect alignment. It was found to be matching as well.

6.2 First Modification

During progression to diastolic HF significant changes in collagen structure can be observed (see Section 4.4). To model the stiffening of passive mechanical response the structure of Holzapfel's equation was altered. Additional parameters were added depending on the direction to be modified to take changes in collagen volume fraction into account.

The isotropic term (I_1) includes the response of the ECM and incorporates the response in the normal directions. To be able to take changes in the structure in all three directions into account by modifying the corresponding invariants and to make the equation more structure based, the original Holzapfel equation was modified as follows. The isotropic term was removed and a term that considers the response in the sheet-normal direction was added (see Equation 6-4).

Equation 6-4

$$\bar{W} = \sum_{i=f,n,s} \frac{a_i}{2b_i} \{ \exp[b_i(I_{4i} - 1)^2] - 1 \} + \frac{a_{fs}}{2b_{fs}} [\exp(b_{fs}I_{8fs}^2) - 1]$$

In contrast to Eriksson's modification (see section 6.1) where the Invariants are modified, the terms describing the directional response were altered, since Invariants incorporate kinematics only and the terms describe stiffness.

Since endomysial collagen coils progressively around myocytes with progression to diastolic heart failure (see section 4.3.3), it was assumed that it contributes to stiffness in fibre and sheet direction. These directions were chosen to be modified by a normalized endomysial collagen fraction x_{endo} as follows.

Equation 6-5

$$\bar{W}_f = \frac{a_f}{2b_f} \{ \exp \left[b_f x_{endo}^2 (I_{4f} - 1)^2 \right] - 1 \}$$

$$\bar{W}_s = \frac{a_s}{2b_s} \{ \exp[b_s x_{endo}^2 (I_{4s} - 1)^2] - 1 \}$$

$$x_{endo} = \frac{x_{diseased\ endo}}{x_{WKY\ 3\ months\ endo}}$$

where $x_{wky_3_months_endo}$ represents the volume fraction of endomysial collagen in the healthy heart (values of WKY rats at 3 months) and $x_{diseased_endo}$ represents endomysial collagen volume fraction of a diseased heart (values for SHR rats at 3, 12, 18 and 24 months). With on-going disease and also with aging x_{endo} rises and herewith contributes to a stiffer behaviour in fibre and sheet directions.

Perimysial collagen volume fraction increases with age as well and hence increases the amount of perimysial collagen transversely to the normal direction, it was assumed to add stiffness predominantly in the normal direction. The normal direction was modified with a normalized perimysial collagen fraction x_{peri} , defined similar to x_{endo} , see Equation 6-6. The higher the perimysial collagen fraction the stiffer the behaviour in normal direction will be.

Equation 6-6

$$\overline{W_n} = \frac{a_n}{2b_n} \{ \exp [b_n x_{peri}^2 (I_{4n} - 2)^2] - 1 \}$$

The calculation of the 2nd Piola Kirchhoff stress tensor is shown in Appendix 1B.

Values for x_{endo} and x_{peri} were chosen to lie in the order of magnitude as values from Fig. 4-5 would suggest (see Table 6-2). They were determined by dividing the actual volume fraction of each case (eg. $x_{actual_endo}=0.025$ for a 12 month WKY rat) by the actual volume fraction at three months for the WKY rat (i.e. $x_{actual_endo} = 0.02$ or $x_{actual_peri} = 0.075$). For example:

Equation 6-7

$$x_{endo_12WKY} = x_{actual_endo_12WKY}/x_{actual_endo_3WKY} = 0.025/0.02 = 1.25$$

	3WKY	3SHR	12WKY	12SHR	18WKY	18SHR	24WKY	24SHR
x_{actual_endo}	0.02	0.06	0.025	0.10	0.1	0.12	0.12	0.12
x_{actual_peri}	0.075	0.04	0.06	0.05	0.04	0.05	0.063	0.05
x_{endo}	1	3	1.25	5	5	6	6	6
x_{peri}	1	0.53	0.8	0.67	0.53	0.67	0.83	0.67

Table 6-2 Values used for calculation of x_{endo} and x_{peri} , adapted from [18]

Due to the modification of the structure of Holzapfel's equation a new parameter set was obtained using a multivariate optimisation as described in section 5.1. Parameters obtained by this optimisation are summarized in Table 6-3 and the

model fit (solid lines) to Dokos' experimental shear data (dashed lines) is shown in Fig. 6-2. [37]

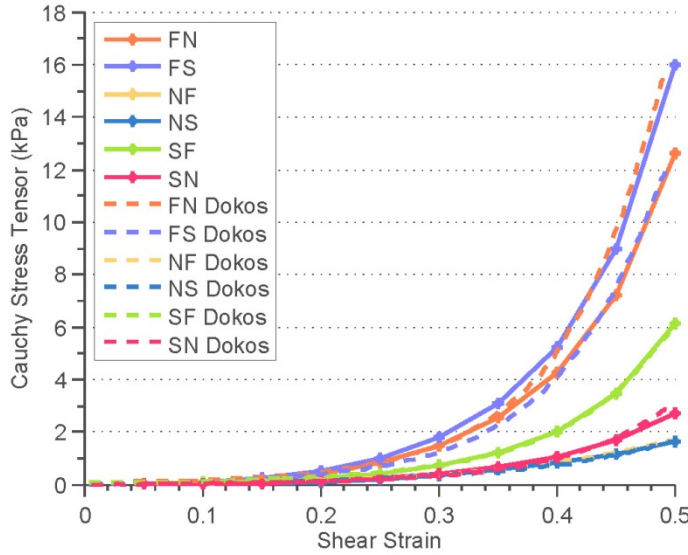


Fig. 6-2 Shear stress/strain curve for the modified equation.

a_n [kPa]	b_n	a_f [kPa]	b_f	a_s [kPa]	b_s	a_{fs} [kPa]	b_{fs}
6.35	0.22	24.82	11.32	6.94	7.07	0.37	11.67

Table 6-3 Summary of material parameters obtained by optimisation

6.3 Second Modification

The mechanical response of the first modification was not satisfactory as model prediction for SHRs at 12 months were stiffer than experimental data and hence the influence of x_{endo} and x_{peri} was too high (see section 7.2.3). Also more structural images became accessible after deriving the first implementation. Based on the structural changes that can be observed in these images, it became clear that perimysial and endomysial collagen influence fibre, sheet and normal direction in another way than assumed in section 6.2. Also values for perimysial collagen volume fraction taken from [15] were not convincing; hence a new way of incorporating the thickening and fusion of perimysial collagen was attempted. Volume fraction was based on a fixed image size. Because of an on-going thickening of collagen between layers, an increase in myocyte diameter and hence a thickening of layers at the same time as collagen fraction increases the perimysial collagen fraction did not change quantitatively. However, a clear rearrangement to sheets with a higher density of perimysial collagen could be observed. Hence values for x_{endo} and x_{peri} should not be obtained from the volume fraction but from other measures such as thickness of collagen.

In this attempt the thickness of endomysial collagen around myocytes was measured in Fig. 6-3. In the WKY 12 months case (right) endomysial collagen thickness $t_{endoWKY}$ laid around 0.4 μm . In the SHR case the thickness $t_{endoSHR}$ increased to around 2 μm . x_{endo} was defined as follows:

Equation 6-8

$$x_{endo} = t_{endoSHR}/t_{endoWKY} = 2/0.4 = 5$$

Perimysial collagen thickness was not as easy to measure as endomysial thickness as the sheets separate in the WKY case due to the drying of the tissue. For an approximate estimation of the thickening of perimysium the cleavage planes were closed and the thickness of perimysium measured in this case compared to the thickness of fused perimysium in the SHR case. The thickness $t_{periWKY}$ was around 2 μm and increases in the SHR case to approximately 12 μm – 20 μm . Hence x_{peri} was defined as follows:

Equation 6-9

$$x_{peri} = t_{periSHR}/t_{periWKY} = [12 : 20]/2 = [6 : 10]$$

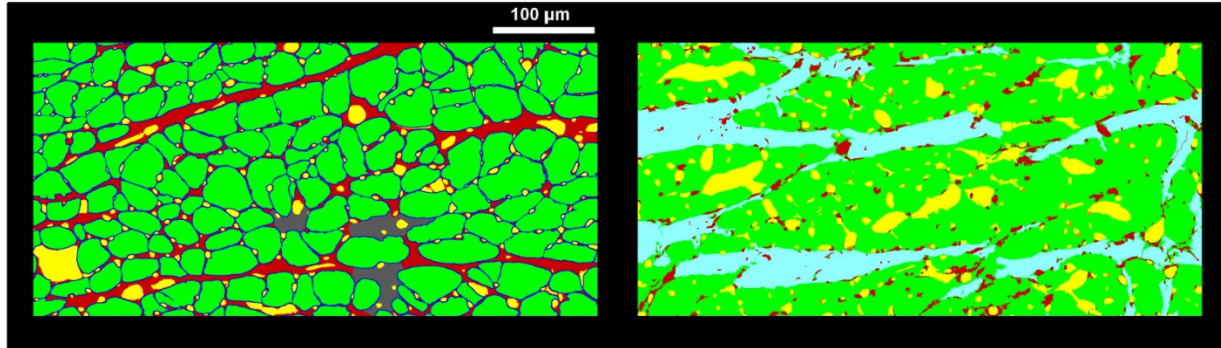


Fig. 6-3 SHR (left) and WKY (right) at 12 months. Blue is endomysial collagen, green myocytes, yellow vessels, grey resembles scar tissue and red perimysial collagen

As the fibre direction that is surrounded by endomysial collagen is just effected by thickening of this collagen during contraction the hypothesis was that the effect can be neglected when simulating passive behaviour. Additionally the sheet direction is strongly affected by the amount of perimysial collagen that fused in between sheets. It counteracts slip between layers as it is possible in a healthy heart and results in a direct resistance to shear.

In contrast to the assumption made in the first modification that thickening of perimysial collagen affects the normal direction, endomysial collagen was here assumed to influence the normal direction most. Since perimysial collagen

thickens between the sheets and hence adds stiffness in the sheet direction, endomysial collagen around fibres thickens and counteracts the extension of myocardium in normal direction (see Fig. 6-4).

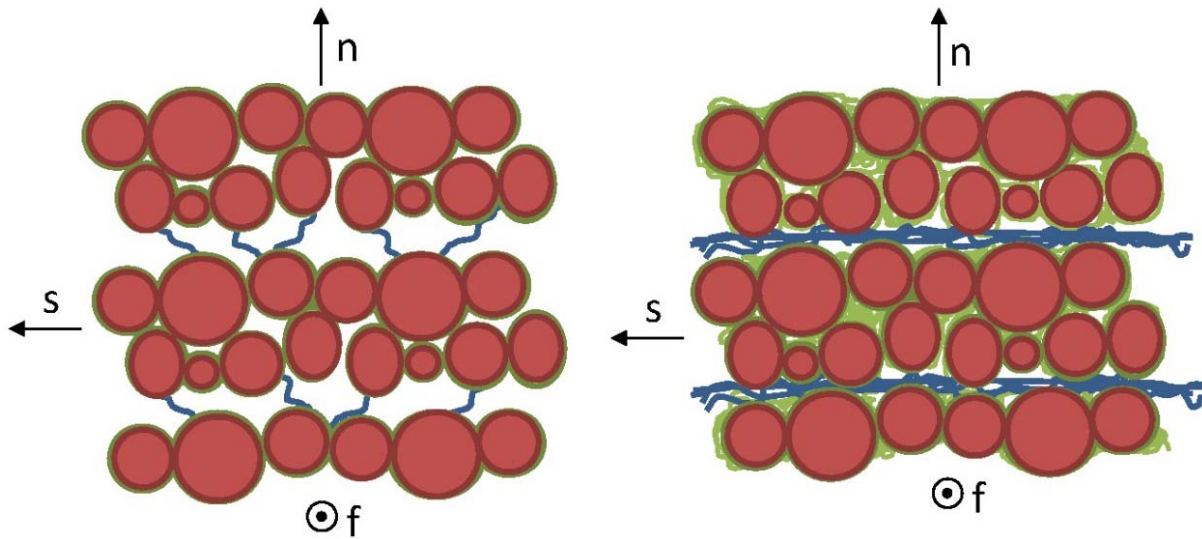


Fig. 6-4 Schematic sketch of healthy (left) and diseased myocardium. Blue depicts persimysial collagen between layers of myocytes and green illustrates endomysial collagen wrapped around individual myocytes

The terms of Equation 6-4 were modified in sheet and normal direction as follows:

Equation 6-10

$$\overline{W}_s = \frac{a_s}{2b_s} \{ \exp[b_s x_{peri}(I_{4s} - 1)^2] - 1 \}$$

$$\overline{W}_n = \frac{a_n}{2b_n} \{ \exp[b_n x_{endo}(I_{4n} - 1)^2] - 1 \}$$

and the Strain-Energy density function became:

Equation 6-11

$$\overline{W} = \frac{a_s}{2b_s} [\exp(b_s x_{peri}(I_{4s} - 1)^2) - 1] + \frac{a_f}{2b_f} [\exp(b_f (I_{4f} - 1)^2) - 1]$$

$$+ \frac{a_n}{2b_n} [\exp(b_n x_{endo}(I_{4n} - 1)^2) - 1] + \frac{a_{fs}}{2b_{fs}} [\exp(b_{fs} I_{8fs}^2) - 1]$$

The 2nd Piola Kirchhoff stress tensor was calculated (see Appendix 1B) and implemented into CellML using the software interface OpenCell. As the gross structure of the constitutive equation did not change in comparison to the first modification the same material parameters were used (see Table 6-3).

6.4 Convexity and Material Stability

To ensure material stability, physically meaningful mechanical behaviour and to avoid undesirable consequences for the development of numerical schemes for the solution of boundary value problems, convexity of the strain-energy density function should be considered [4]. Ogden [43] pointed out that convexity of the strain-energy density function is a consequence of material stability, but it does not necessarily guarantee material stability as components of the strain-energy function could be negative.

The new form of the constitutive equation introduced in section 6.2 (deleting Holzapfel's isotropic term and introducing a term for the normal direction) has got the same advantage as Holzapfel's original equation. As Holzapfel et al. [4] point out, the function consists of a sum of separate functions, including just one invariant at each time and no cross-terms of invariants. Hence the convexity status of each term can be assessed separately. Following Holzapfel et al. [4] four functions are considered to investigate the convexity of the strain-energy density function introduced in section 6.3: $F(I_{4f})$, $G(I_{4s})$, $H(I_{8fs})$ and $J(I_{4n})$ (see Equation 6-12 to Equation 6-15).

Equation 6-12

$$F(I_{4f}) = \frac{a_f}{2b_f} [\exp(b_f(I_{4f} - 1)^2) - 1]$$

Equation 6-13

$$G(I_{4s}) = \frac{a_s}{2b_s} \{\exp[b_s x_{peri}(I_{4s} - 1)^2] - 1\}$$

Equation 6-14

$$H(I_{8fs}) = \frac{a_{fs}}{2b_{fs}} [\exp(b_{fs} I_{8fs}^2) - 1]$$

Equation 6-15

$$J(I_{4n}) = \frac{a_n}{2b_n} \{\exp[b_n x_{endo}(I_{4n} - 1)^2] - 1\}$$

The convexity of $F(I_{4f})$ and $H(I_{8fs})$ has been already shown by Holzapfel et al. [4]. The influence of the introduction of x_{peri} and x_{endo} on convexity is examined here exemplary on the term $G(I_{4s})$ by considering the convexity as a function of the right Cauchy-Green strain tensor \mathcal{C} .

It follows from the definition of I_{4s} in Equation 4-14 that

Equation 6-16

$$\frac{\partial G}{\partial \mathbf{C}} = G'(I_{4s}) \mathbf{s}_0 \otimes \mathbf{s}_0 \text{ and } \frac{\partial^2 G}{\partial \mathbf{C} \partial \mathbf{C}} = G''(I_{4s}) \mathbf{s}_0 \otimes \mathbf{s}_0 \otimes \mathbf{s}_0 \otimes \mathbf{s}_0$$

Following Holzapfel et al. [4] local convexity of $G(I_{4s})$ required for all second-order tensors \mathbf{A} that

Equation 6-17

$$\frac{\partial^2 G}{\partial \mathbf{C} \partial \mathbf{C}} [\mathbf{A}, \mathbf{A}] \equiv G''(I_{4s}) [(\mathbf{A} \mathbf{s}_0) \mathbf{s}_0]^2 \geq 0$$

Hence G is convex in C if $G''(I_{4s}) \geq 0$. For Equation 6-13 we obtain

Equation 6-18

$$G'(I_{4s}) = a_s x_{peri} (I_{4s} - 1) \cdot \exp(b_s x_{peri} (I_{4s} - 1)^2)$$

Equation 6-19

$$G''(I_{4s}) = a_s x_{peri} \cdot \exp(b_s x_{peri} (I_{4s} - 1)^2) \cdot (1 + 2b_s (I_{4s} - 1)^2)$$

For extension in the sheet direction I_{4s} is always above 0 and as the material response has to stiffen for higher stresses (see Dokos' experiments, section 4.3.2) a_s and b_s are always above zero as well. As x_{peri} is defined as the quotient of the thickness of perimysial collagen in diseased and normal case and the thickness in the diseased case was generally observed to be higher than in the healthy case, we have $x_{peri} \geq 1$. These inequalities imply that $G''(I_{4s}) > 0$ and hence G is a convex function. As x_{endo} is defined similar to x_{peri} , $a_n > 0$ and $b_n > 0$ as well, and it follows that Equation 6-15 is convex as well.

As the convexity of the individual terms that contribute additively to the strain-energy density function has been proven the overall strain-energy function is convex as well [4]. For the purpose of this thesis it is sufficient to guarantee convexity to ensure the suitability for numerical implementation (for further details see [43] and [44]). However, to ensure material stability the equations should be analysed in terms whether the strong ellipticity condition holds. It precludes non-smooth deformations for example. Yet the analysis for three-dimensional, anisotropic problems is difficult and goes beyond the scope of this thesis [4, 43]. Holzapfel et al. [4] analysed the ellipticity of their equation and found that strong ellipticity does hold for extension in the fibre or sheet direction, but not for compression. Hence the I_{4f} and I_{4s} terms were considered to be inactive when $I_{4f} < 1$ or $I_{4s} < 1$. Therefore, as only positive x_{endo} and x_{peri} were added to the equation we conclude that I_{4n} should be dropped as well if $I_{4n} < 1$ to ensure ellipticity. Further details can be found in [4].

As the introduced strain-energy-density function consists of a sum of separate functions, including only one invariant each time and no cross-terms of invariants the convexity status is easy to assess. The convexity of all functions is shown in this section and hence also, that the overall equation is suitable for numerical implementation.

7 Modelling of Heart Failure Mechanics

The three equations described in section 6 are analysed in their local and global mechanical behaviour in this section. Results are subsequently discussed for each case.

7.1 Implementation of the Augmented Holzapfel Equation

In this section the results of the implementation of the augmented Holzapfel equation described in section 6.1 are discussed. First an analytical implementation was undertaken to understand the qualitative influence of alterations in the equation. Subsequently a FEM analysis of LV passive inflation was implemented to examine the impacts of modifications on global organ behaviour.

7.1.1 Analytical Implementation

The qualitative responses of the augmented Holzapfel equation were investigated by simulating simple shear and biaxial extension as described in sections 5.2 and 5.3.

7.1.1.1 Simple Shear

To examine the effects of variation of κ_s , i.e. increasing or decreasing dispersion, on local mechanical behaviour simple shear of cubes was simulated, based on Dokos' experiments.

κ_s	FN [kPa]	FS [kPa]	NF [kPa]	NS [kPa]	SF [kPa]	SN [kPa]
0	13.9	17.37	1.756	1.756	6.505	3.04
0.3	13.99 ↑	17.45 ↑	1.842 ↑	1.842 ↑	5.495 ↓	2.03 ↓

Table 7-1 Value of stress at a shear strain amount of 0.5 for $\kappa_s = 0$ and $\kappa_s = 0.3$

Fig. 7-1 shows the shear stress-strain curve for $\kappa = 0$ and $\kappa = 0.3$, respectively. The SN curve showed the biggest change by decreasing from a value of 3.04 kPa

at a shear strain amount of 0.5 and $\kappa = 0$ to a value of 2.03 kPa at $\kappa = 0.3$. Table 7-1 gives an overview over the stress values for $\kappa = 0$ and $\kappa = 0.3$ at a shear-strain amount of 0.5 and shows that FS, FN and NS responses became slightly stiffer whereas SN and SF responses shifted to values corresponding to reduced stiffness.

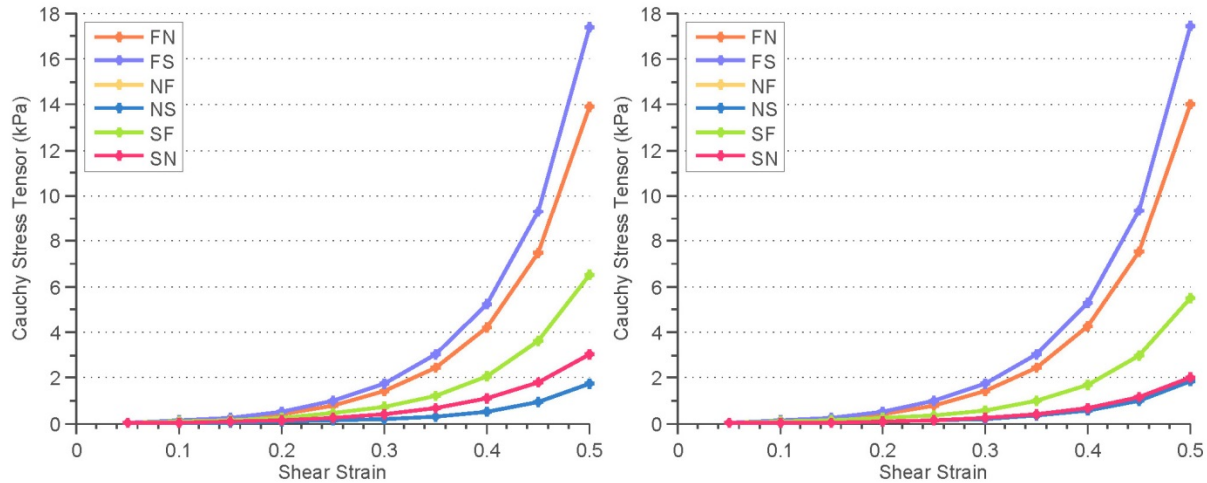


Fig. 7-1 Shear stress-strain curve for $\kappa_s=0$ (left) and $\kappa_s=0.3$ (right)

7.1.1.2 Axial Extension

Fig. 7-2 illustrates the stress-strain curves for the extension in the sheet and normal directions for $\kappa_s = 0$ and $\kappa_s = 0.3$. Whilst the stress-strain curve for the response in fibre direction did not vary the response in sheet direction changed significantly decreasing from 14.22 kPa to 2.769 kPa. The normal response shifted to a slightly stiffer behaviour from a value of 1.235 kPa at $\kappa_s = 0$ to 1.4 kPa at $\kappa_s = 0.3$ (see Table 7-2).

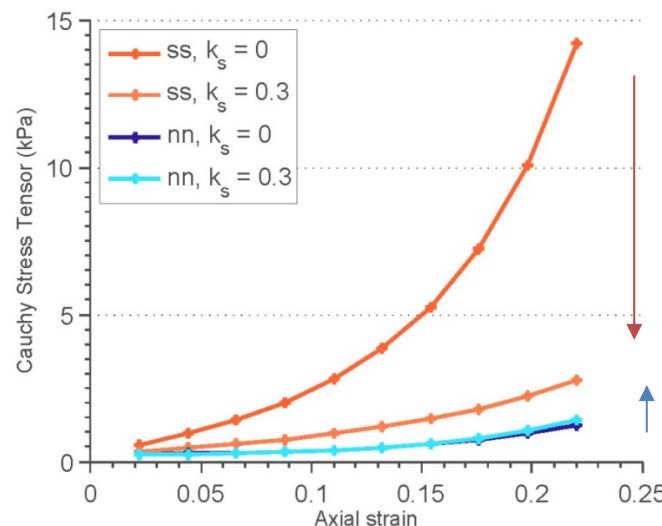


Fig. 7-2 Stress-strain curves for axial extension in the sheet (red) and normal (blue) directions for $\kappa=0$ and $\kappa=0.3$ (right)

κ_s	Stress ff [kPa]	stress ss [kPa]	Stress nn [kPa]
0	281.5	14.22	1.235
0.3	281.5	2.769	1.4

Table 7-2 Values of stress during axial extension in the fibre, sheet and normal directions at a shear strain amount of 0.22

7.1.2 Finite Element Analysis of LV Passive Mechanics

To analyse the influence of a variation of κ_s on global LV function, passive LV mechanics was simulated using a geometry of a 12 month WKY. Intraventricular pressure was increased from 0 mmHg to 30 mmHg and the associated chamber volume was calculated for each pressure increment. Pressure-volume curves were plotted and compared against each other.

In Fig. 7-3 the pressure-volume (PV) characteristics of the model (left) and the compliance-pressure curves are illustrated. An increase in κ_s resulted in an increase in compliance and a slight right-shift of the PV-curves. However, the effect seems to be marginal, particularly since the change became even smaller for higher κ_s values.

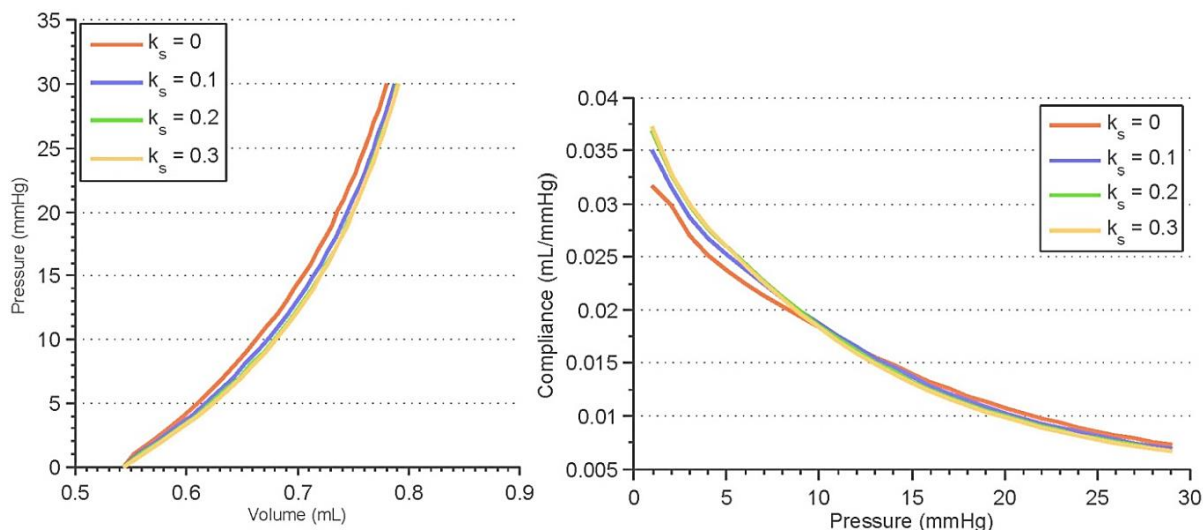


Fig. 7-3 PV-curve for 4 different κ_s parameters and compliance curve for 4 different values of κ_s

7.1.3 Conclusion and Discussion

In this section the simulation results are discussed and conclusions are summarised.

7.1.3.1 Structure of the Equation

Equation 7-1 shows the 2nd Piola Kirchhoff stress tensor components for the Holzapfel and Ogden relation augmented with κ_s for the lower limit $\kappa_s = 0$. In that case the equation reduces to the initial Holzapfel and Ogden relation (see Equation 4-13). Equation 7-2 describes the 2nd Piola Kirchhoff stress tensor components for the same relation for the upper boundary of $\kappa_s = 1/3$, which describes full dispersion.

Equation 7-1

$$\begin{aligned} T_{dev}^{11}(\kappa = 0) &= a \cdot \exp(2b(E_{11} + E_{22} + E_{33})) + 4a_f E_{11} \cdot \exp(4b_f E_{11}^2) \\ T_{dev}^{22}(\kappa = 0) &= a \cdot \exp(2b(E_{11} + E_{22} + E_{33})) + 4a_s E_{22} \exp(4b_s E_{22}^2) \\ T_{dev}^{33}(\kappa = 0) &= a \cdot \exp(2b(E_{11} + E_{22} + E_{33})) \end{aligned}$$

Equation 7-2

$$\begin{aligned} T_{dev}^{11}\left(\kappa = \frac{1}{3}\right) &= T_{dev}^{11}(\kappa = 0) + \frac{4}{9}a_s(E_{11} + E_{22} + E_{33}) \cdot \exp\left(\frac{4}{9}b_s(E_{11} + E_{22} + E_{33})^2\right) \\ T_{dev}^{22}\left(\kappa = \frac{1}{3}\right) &= a \cdot \exp(2b(E_{11} + E_{22} + E_{33})) + \frac{4}{9}a_s(E_{11} + E_{22} + E_{33}) \\ &\quad \cdot \exp\left(\frac{4}{9}b_s(E_{11} + E_{22} + E_{33})^2\right) \\ T_{dev}^{33}\left(\kappa = \frac{1}{3}\right) &= T_{dev}^{33}(\kappa = 0) + \frac{4}{9}a_s(E_{11} + E_{22} + E_{33}) \cdot \exp\left(\frac{4}{9}b_s(E_{11} + E_{22} + E_{33})^2\right) \end{aligned}$$

In this case it becomes clear that T_{dev}^{11} and T_{dev}^{33} increase in comparison to the initial equation by the same term.

As Equation 7-1 indicates, the augmented Holzapfel equation should show the same mechanical response for $\kappa_s = 0$ as the initial Holzapfel's equation. As can be seen from Fig. 6-1 this is the case.

7.1.3.2 Discussion of Simulation Results

In Table 7-1 the stress values after the application on a shear strain amount of 0.5 are summarised. Consistent with Equation 7-1 and Equation 7-2 the FN, FS and NS responses shift to higher stress values. However, the responses in SF and SN directions are more significant.

The effect of change of κ_s on the PV-curves is minimal. The fibre direction still dominates the response since it is much stiffer compared to the sheet direction and not significantly altered by changes in κ_s . Since the sheet direction softens significantly and stiffening in the fibre and normal directions is small compared

to this effect, increasingly compliant PV-curves for higher values for κ_s can be explained. In summary κ_s softens the sheet direction by describing decreased alignment of sheets and elevates the stiffness in the normal and fibre directions by adding the stiffness of the dispersed sheets. However, the latter effect is small compared to the amount of softening in sheet direction.

7.1.3.3 Conclusion

During the progression from a healthy case to diastolic dysfunction a significant decrease in compliance can be observed, while it increases subsequently with further progression to systolic heart failure. PV-curves for diastolic dysfunction are significantly left-shifted in comparison to age-matched WKY rats (see section 4.3.3). [18]

An increase in κ_s could take the progressive disorder of sheets into account that can be observed in SHRs at an age of eighteen to twenty-four months, since the PV-curve is shifted slightly to the right and curves for higher κ_s become more compliant. However, the changes are very small and the progression to diastolic heart failure cannot be modelled. Hence further modification has to be made to increase the impact of a change in structural parameters on the response of the equation. Since the impact is small no further FEM modelling is undertaken with this modification.

7.2 Implementation of the First Modification

In this section the results of the implementation of the first modified equation (Equation 6-4) described in section 6.2 are summarised and discussed.

7.2.1 Analytical Implementation

To examine the effects of variation of x_{endo} and x_{peri} on local mechanical behaviour simple shear and biaxial extension on cubes was simulated.

7.2.1.1 Simple Shear

In Table 7-3 the stress response is shown for different values for x_{endo} , while keeping $x_{peri} = 1$, at a shear strain amount of 0.5. Since x_{endo} modified the fibre and sheet directions only, the FS, FN, SF and SN modes were affected. As x_{endo} increased the stress values rised exponentially to very high values.

x_{endo}	x_{peri}	FN [kPa]	FS [kPa]	SF [kPa]	SN [kPa]
0.05	1	0.0155	3.437	3.426	0.004342
0.5	1	1.851	5.273	3.906	0.4844
1.5	1	68.59	72.01	13.97	10.55
2	1	420.6	424	44.06	40.64
2.5	1	3229	3232	175	171.6
3	1	32540	32540	836.5	833.1

Table 7-3 Value of stress at a shear strain amount of 0.5 for different values of x_{endo}

In Table 7-4 the stress response at a shear strain amount of 0.5 for different values of x_{peri} keeping $x_{endo} = 1$ is shown. As before for FS and FN modes the stress values increased exponentially for changes of x_{peri} .

x_{peri}	x_{endo}	NF=NS [kPa]
0.05	1	0.003969
0.5	1	0.3982
1.5	1	3.684
2	1	6.709
2.5	1	10.81
3	1	16.17

Table 7-4 Value of stress at a shear strain amount of 0.5 when varying x_{peri}

7.2.1.2 Axial extension

Since x_{endo} modifies the fibre and sheet terms, and x_{peri} affects the normal terms only, in Table 7-5 an overview of the stress values for axial extension in fibre, sheet and normal direction is given, for variations in x_{endo} and x_{peri} , respectively. As well as shown in simple shear simulations the stress increased exponentially with x values. The stress in fibre direction already reached a value of 806900 kPa

at $x_{endo} = 2$ Fig. 7-4 shows examples of stress/strain curves for different values of x_{peri} .

x_{endo}	Stress ff [kPa]	Stress ss [kPa]	x_{peri}	Stress nn [kPa]
0.5	13.6	3.096	0.5	2.003
1	281.5	34.57	1	8.397
1.5	9802	430.4	1.5	19.93
2	806900	8395	2	38.17

Table 7-5 Values of stress during axial extension in fibre, sheet and normal direction at a shear strain amount of 0.22

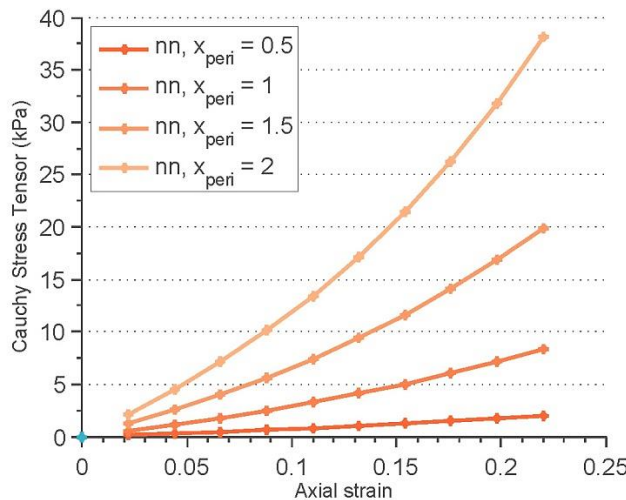


Fig. 7-4 Stress-strain curve for axial extension in normal direction for different x_{peri} values

7.2.2 Finite Element Analysis of LV Passive Mechanics

To analyse the global influence of a variation of x_{endo} and x_{peri} , passive filling of the LV was simulated using the geometry of a WKY rat. As the first step pressure-volume curves were plotted with varying values of x_{endo} and x_{peri} in order to gain a better understanding of the influence of the different parameters.

Following this initial analysis the normalised collagen fractions were constrained to be those derived from [15] and passive inflation was re-simulated. A bivariate 'M' and 'N' optimisation was then undertaken as described in section 5.6 to tailor the parameter set to match the behaviour of living myocardium. Subsequently the novel parameter set was applied using the geometry of a 12 month old SHR.

7.2.2.1 Global Influence

Fig. 7-5 and Fig. 7-6 illustrate the pressure-volume (PV) and compliance outputs of the model, for a variation of either x_{endo} or x_{peri} . Both PV-curves shifted to the left with higher values of x_{endo} and x_{peri} while curves became less compliant. Variations of x_{endo} resulted in a more significant change in stiffness of the PV-curve.

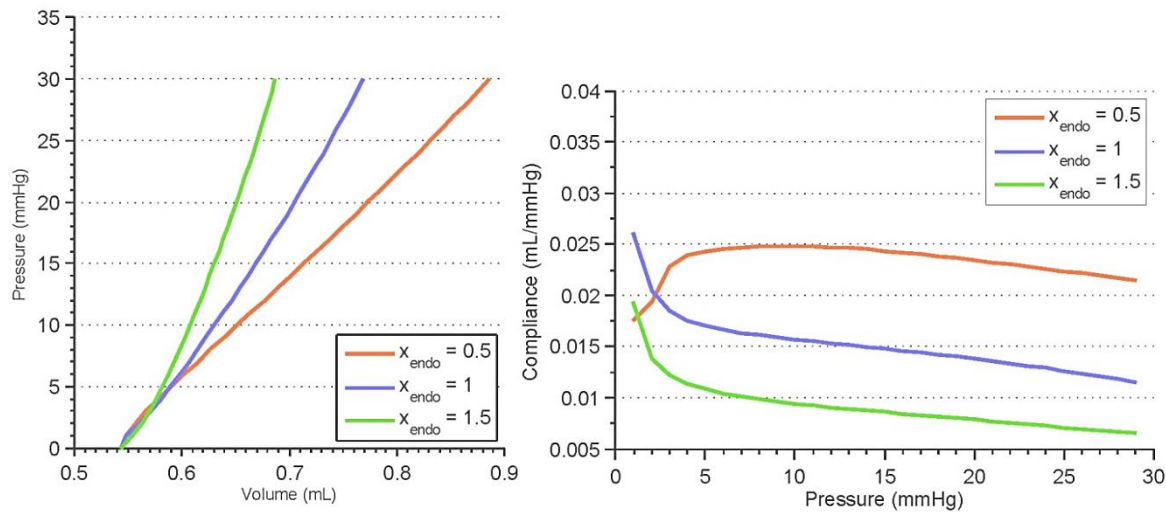


Fig. 7-5 Changes in PV and compliance-curves for variation of x_{endo} while $x_{peri} = 1$

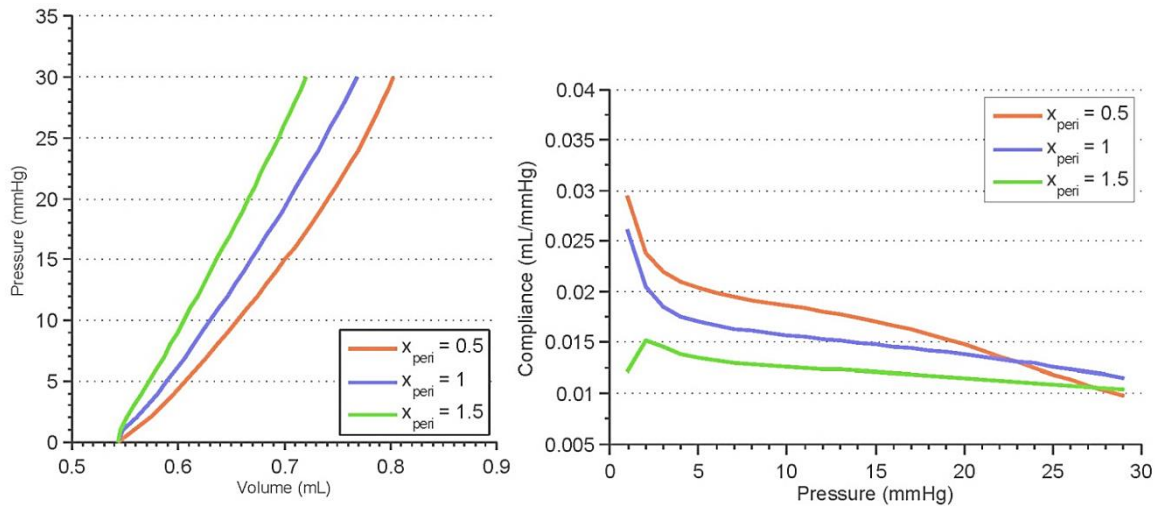


Fig. 7-6 Changes in PV and compliance-curves for variation of x_{peri} while $x_{endo} = 1$

7.2.2.2 'M' and 'N' Parameter Estimation

The first modification of the constitutive relation was implemented and simulated using the geometry of a 12 months WKY. x_{endo} and x_{peri} were chosen to be 1.25 and 0.8, respectively, according to Table 6-2. The optimal solution for 'M' and 'N' matched the average values after five iterations with five initial guesses as

described in section 5.6. ‘ M ’ was obtained as 0.475 and ‘ N ’ as 0.492 with a $resnorm$ of $6.52 \cdot 10^{-4}$.

Simulations for a SHR geometry at 12 months were undertaken with $x_{endo} = 5$ and $x_{peri} = 0.67$ (see Table 6-2), using material parameters obtained by bivariate optimisation using the geometry of a WKY at 12 months. The parameter set is summarised in Table 7-6.

$a_n [kPa]$	b_n	$a_f [kPa]$	b_f	$a_s [kPa]$	b_s	$a_{fs} [kPa]$	b_{fs}
3.014	0.108	11.78	5.568	3.294	3.478	0.176	5.740

Table 7-6 Summary of material parameters obtained by bivariate optimisation

In the left graph in Fig. 7-7 the model prediction in solid lines against the plot of experimental data for a WKY rat at an age of 12 months before fitting of ‘ M ’ and ‘ N ’ is shown .

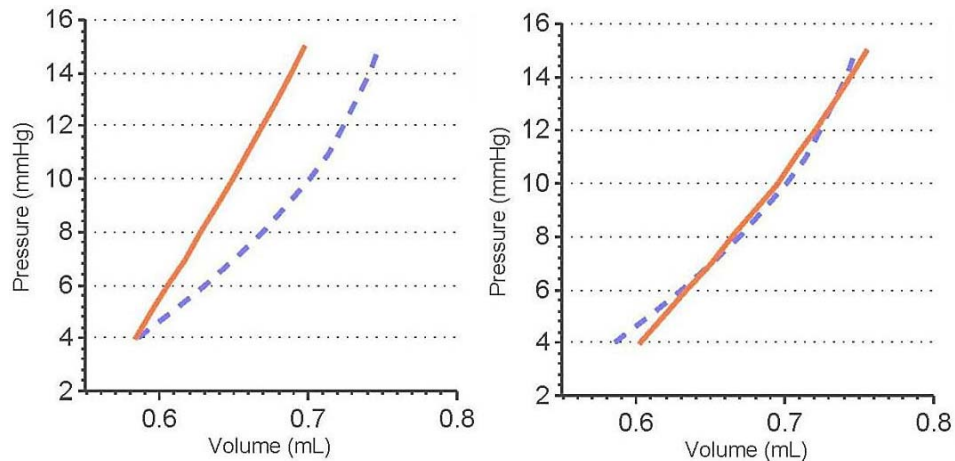


Fig. 7-7 PV-curves for a WKY rat at 12 months for model prediction (orange solid lines) and experimental data (violet dashed lines). Left for $M=N=1$ and right for fitted ‘ M ’ and ‘ N ’

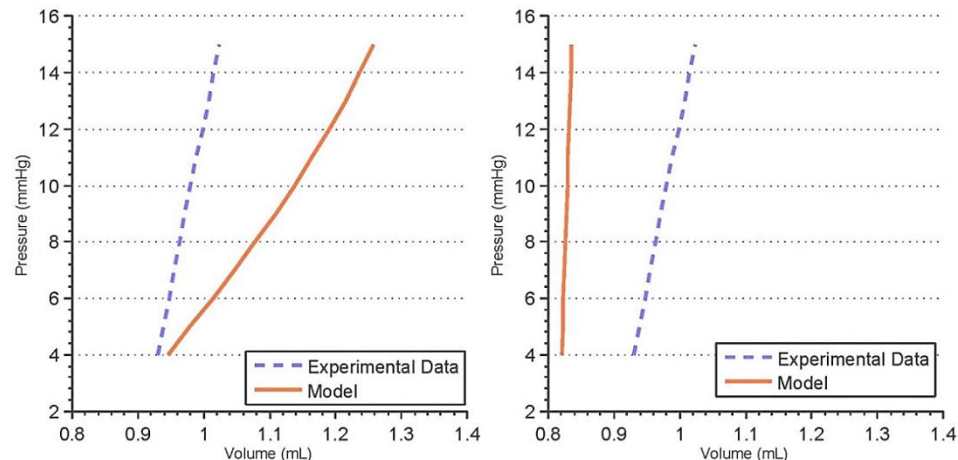


Fig. 7-8 PV-curves for a SHR at 12 months for model prediction (dashed lines) and experimental data. Left for $x_{endo} = x_{peri} = 1$ and right for $x_{peri} = 0.67$ and $x_{endo} = 5$

The model shows a stiffer behaviour than the experimental data. After the optimisation both curves aligned.

A stiffening and leftward shift of the PV-curves for SHRs at 12 months (see Fig. 7-8) could be noted when applying the new parameter set customised to the WKY rat functional data. Incorporating x_{endo} and x_{peri} lead to significant stiffening.

7.2.3 Conclusion and Discussion

In this section the simulation results are discussed and conclusions are summarised.

7.2.3.1 Structure of the Equation

To be sure that no linear correlation existed between the modified and original constitutive equation an excel calculation comparing the initial 2nd Piola Kirchhoff Stress Tensor component for fibre direction (without x_{endo} , Equation 7-3) with the modified component (Equation 7-4) was undertaken.

Equation 7-3

$$T_{dev,ini}^{11} = 4a_f E_{11} \cdot \exp(4b_f E_{11}^2)$$

Equation 7-4

$$T_{dev}^{11} = 4a_f E_{11} x_{endo}^2 \cdot \exp(4b_f x_{endo}^2 E_{11}^2)$$

Equation 7-5

$$T_{dev}/T_{dev,ini}^{11} = x_{endo}^2 \cdot \exp(4b_f E_{11}^2 \cdot (x_{endo}^2 - 1))$$

Since Equation 7-5 applies no linear relationship occurs. The parameters input to CellML and CMISS becomes:

$$[Mx_{endo}^2 a_f, Ma_{fs}, Mx_{peri}^2 a_n, Mx_{endo}^2 a_s, Nx_{endo}^2 b_f, Nb_{fs}, Nx_{peri}^2 b_n, Nx_{endo}^2 b_s]$$

Since not all parameters are multiplied by a volume fraction, there is no direct scaling of all 'M' and 'N' parameters, hence the modification is not just scaling the fitted parameters but modifying the anisotropy of the equation.

7.2.3.2 Analytical Implementation

As the results of axial extension and simple shear simulation show, stress values become very high for rising x values. This is due to the quadrature in the 2nd Piola Kirchhoff Stress Tensor components in front of the exponential as well as in the exponent and to the definition of x parameters.

7.2.3.3 FE Analysis

The PV-curves for the WKY rat geometry show a stiffer behaviour and a shift to the left for the model fit compared to the experimental data. This is reasonable, since Dokos' experimental data was obtained by shearing *ex vivo* cubes of myocardium. The mechanical response of dead myocardium is likely to be stiffer as the tissue enters a state of rigor mortis. The PV-data, in contrast, was obtained *in vitro* on a living heart, perfused to minimise the onset of rigor mortis.

7.2.3.4 Conclusion

The introduction of x_{endo} and x_{peri} results in a significantly less compliant behaviour. Since the model prediction for SHRs at 12 months (see Fig. 7-8) shifted well to the left and is stiffer than experimental data, the influence of x_{endo} and x_{peri} is too high and further modification should be reconsidered. x_{endo} has a larger effect since it modifies the fibre and sheet directions which are stiffer than the normal direction.

Since PV-curves for diastolic dysfunction are significantly left-shifted in comparison to age-matched WKY rats (see section 4.3.3), the introduction of a stiffening parameter that is correlated with the rise in collagen fraction with ongoing disease seems to be reasonable. However, their implementation into the equation has to be further refined, especially because data for perimysial collagen volume fraction is not convincing. Also, the incorporation of x_{endo} and x_{peri} results in a very stiff behaviour (see Fig. 7-8) and a left shift of the PV-curve that overestimates the behaviour for a SHR at 12 months. Another way of incorporating the thickening of perimysial collagen has to be found to be able to better describe the behaviour of SHRs at 12 months.

7.3 Implementation of the Second Modification

In this section the results of the implementation of the second modification equation described in section 6.3 are summarised and discussed.

7.3.1 Analytical Implementation

To examine the local effects of a variation of x_{endo} and x_{peri} on mechanical behaviour simple shear and biaxial extension on cubes is simulated as follows.

7.3.1.1 Simple Shear

In Table 7-7 stress values for a shear strain amount of 0.5 are summarised. Stress for NS and NF raised from 1.609 kPa to a value half as high as the stress value for FS and the stresses for SF and SN were substantially elevated.

x_{endo}	x_{peri}	FN	FS	NF = NS	SF	SN
1	1	12.59	16.01	1.609	6.121	2.699
5	8	12.59	16.01	8.502	492.4	476

Table 7-7 Values of stress at a shear strain amount of 0.5 for variable values of x_{endo} and x_{peri}

In Fig. 7-9 the changes between shear stress-strain curves for $x_{endo} = x_{peri} = 1$ (left) and $x_{endo} = 5, x_{peri} = 8$ (right) up to 30 % strain are compared.

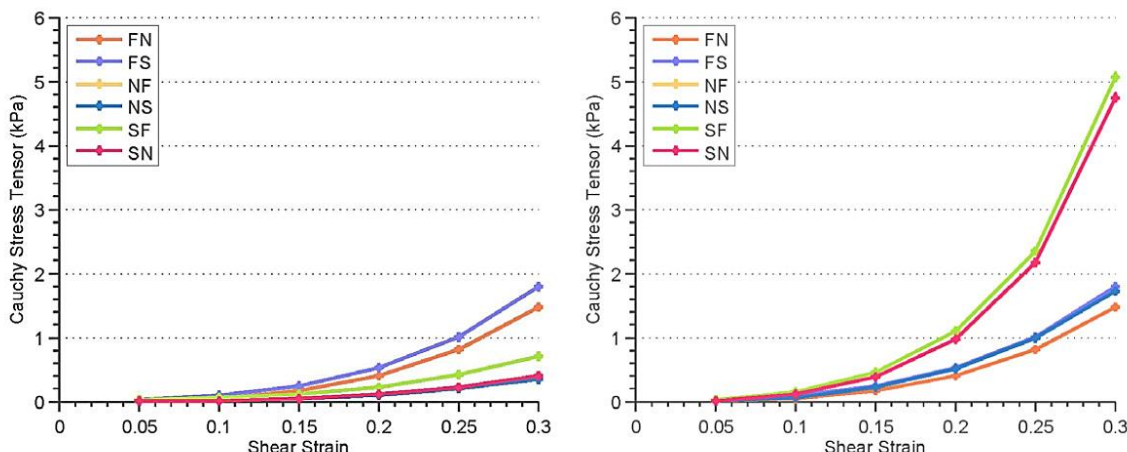


Fig. 7-9 2 Shear stress-strain curve up to an shear strain amount of 0.3 for $x_{endo}=x_{peri}=1$ (left) and $x_{endo}=5, x_{peri}=8$ (right)

7.3.1.2 Axial Extension

Since the amount of endomysial collagen around myocytes in diseased myocardium is observed to increase around five times compared to healthy myocardium, a range of values between 1 and 10 was used to investigate the effects.

In Fig. 7-10 the rise in stress in the normal direction for different values of x_{endo} in comparison to the response in the fibre direction is compared. As shown in the simulation of simple shear the stress values in the sheet direction raised exponentially to very high values of $77.38 \cdot 10^6$ kPa for $x_{peri} = 10$. Since x_{endo} modifies only the normal direction and x_{peri} only the sheet direction, the stress

response in the fibre direction remained unchanged. Table 7-8 summarises the stress values for different values of x_{endo} and x_{peri} .

x_{peri}	stress ss [kPa]	x_{endo}	Stress nn [kPa]	Stress ff [kPa]
1	34.57	1	8.397	281.5
5	41250	5	49.78	281.5
10	$77.38 \cdot 10^6$	10	123.2	281.5

Table 7-8 Values of stress during axial extension in sheet, normal and fibre direction at a shear strain amount of 0.22 %

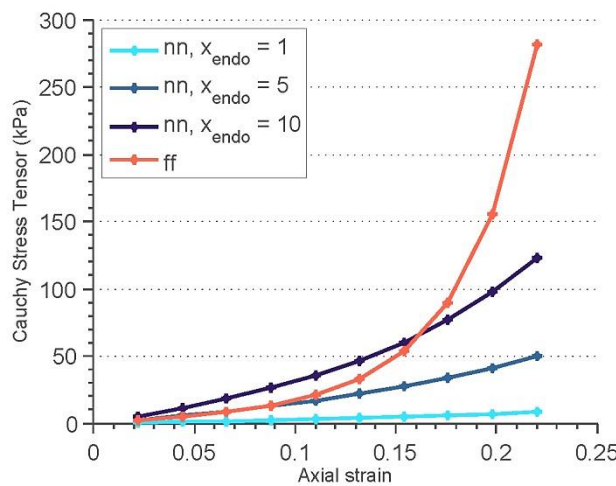


Fig. 7-10 Effect on Stress-Strain response in normal direction for different x_{endo} compared to the fibre direction (orange)

7.3.2 Finite Element Analysis of the Left Ventricle

The global influence of variations of x_{endo} and x_{peri} was examined by simulation of passive filling of the LV. PV-curves up to 30 mmHg were plotted and compared to understand the qualitative influence of variations of x_{endo} and x_{peri} .

Subsequently a bivariate 'M' and 'N' optimisation was undertaken for $x_{endo} = x_{peri} = 1$ as described in section 5.6 to tailor the parameter set to be able to represent living myocardium for all five available geometries of 12 month WKYs (see Appendix 2A for a summary of all five optimisations). The novel parameter sets were then implemented using the geometry of a 12 month SHR. The parameter set of the WKY rat that gives the closest fit to experimental data for a 12 month SHR case with the SHR geometry was used further.

To make sure a physically meaningful combination of x_{endo} and x_{peri} is theoretically possible an optimisation for both parameters was undertaken and then reviewed. Successively x_{endo} and x_{peri} were determined as described in section 6.3. Then the initial dataset determined by fitting to Dokos' data (see Table 6-3) was used to perform a bivariate optimisation to estimate values for 'M' and 'N' which would be capable to reproduce both WKY and SHR PV-curves just by alteration of x_{endo} and x_{peri} . As fitting to PV-curves did not give satisfactory results fitting was subsequently undertaken to compliance curves.

7.3.2.1 Global Influence

Fig. 7-11 illustrates PV outputs of the model as functions of x_{endo} and x_{peri} from 1 to 10. PV-curves became steeper with rising values of x_{endo} and x_{peri} and hence the highest compliance could be observed for $x_{endo} = x_{peri} = 1$. Variations to higher values for x_{endo} and x_{peri} resulted in a significant stiffening of the PV response.

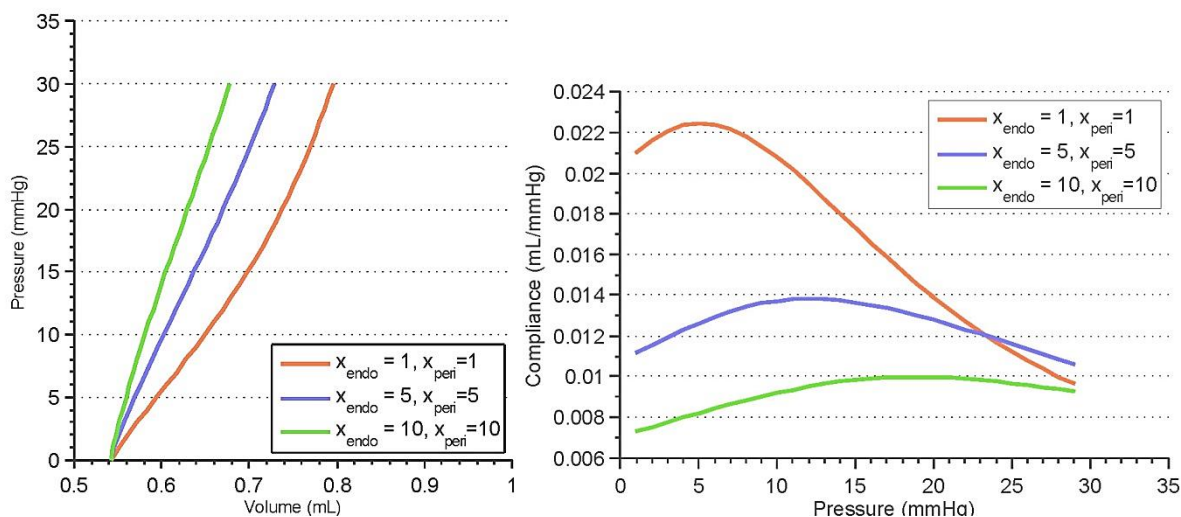


Fig. 7-11 Changes in PV-curves for different combinations of x_{peri} and x_{endo}

7.3.2.2 'M' and 'N' parameter estimation

The second modification was implemented and simulated with 12 months WKY rat geometries. x_{endo} and x_{peri} were chosen to be 1 to represent the healthy case as the normalisation case. The optimal solution for 'M' and 'N' resembled the average values after five iterations with five initial estimates as described in section 5.6.

In Fig. 7-12 the experimental data versus the model fit for the WKY rat geometry that gives the best fit to the subsequent implementation using the geometry of a SHR is shown. For this WKY geometry 'M' was obtained as 1.26 and 'N' as 0.133 with a *resnorm* of $1.80 \cdot 10^{-3}$. In Table 7-9 the parameter set used further is

shown. As can be seen on the right of Fig. 7-12 the 'M' and 'N' optimisation was not able to capture the curvature of the WKY case.

$a_n [kPa]$	b_n	$a_f [kPa]$	b_f	$a_s [kPa]$	b_s	$a_{fs} [kPa]$	b_{fs}
8.017	0.029	31.334	1.509	8.761	0.942	0.467	1.555

Table 7-9 Summary of material parameters obtained by bivariate optimisation

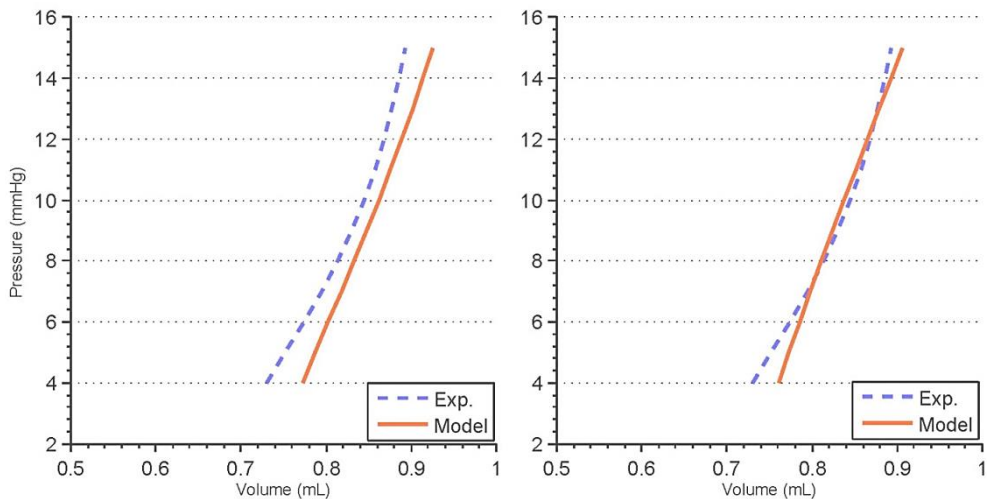


Fig. 7-12 PV-curves for a WKY rat at 12 months with model prediction overlaid with experimental data Left for ' $M=N=1$ ' and right for fitted ' M ' and ' N '

7.3.2.3 Theoretical Optimisation of x_{endo} and x_{peri}

Since another way to incorporate the structural changes of perimysial and endomysial collagen than the collagen volume fraction had to be found, an optimisation approach was undertaken to find theoretical values for x_{endo} and x_{peri} that would be capable of representing the diseased case. To validate whether a set of values for x_{endo} and x_{peri} would be able to give a reasonable fit to PV data, three optimisations were performed using a similar framework as described for the bivariate 'M' and 'N' optimisation (see section 5.6).

Passive filling was simulated using the geometry of a SHR employing the novel parameter set obtained in the previous section (see Table 7-9). First x_{endo} was increased from 1 to 15 and for each x_{endo} an optimisation for x_{peri} was performed. Then x_{peri} was increased from 1 to 15 as well and for each value an optimisation for x_{endo} was performed. The third step consisted of a bivariate optimisation for both x_{peri} and x_{endo} .

In Fig. 7-13 values of x_{peri} after the optimisation are illustrated, for a chosen value of x_{endo} (left) and vice versa (right). Although the plot for the *resnorm* is rather flat

for the optimisation of x_{peri} , a local minimum for $x_{peri} = 8$ and $x_{endo} = 5$ can be seen for both optimisations.

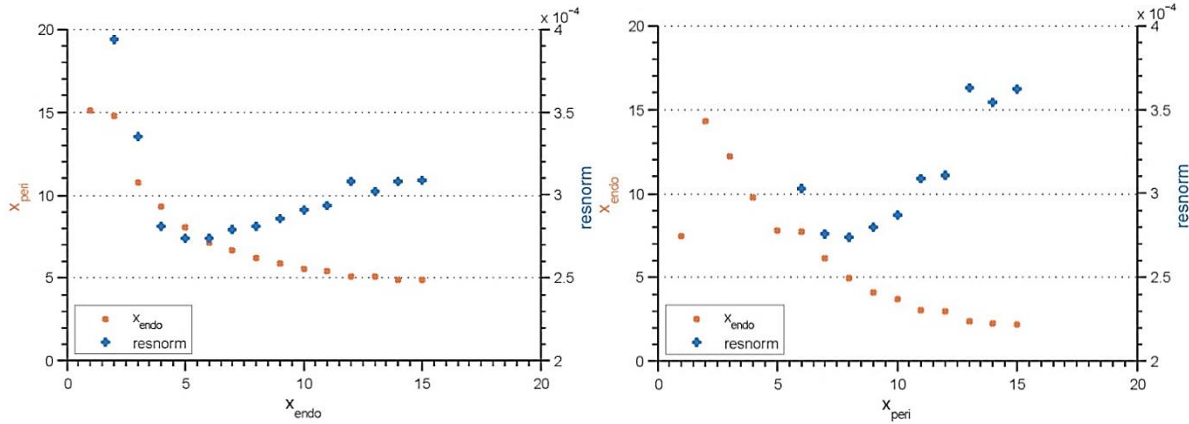


Fig. 7-13 Results of optimisations of x_{peri} (left) and x_{endo} (right, left y-axis), plotted against the $resnorm$ (right y-axis), respectively

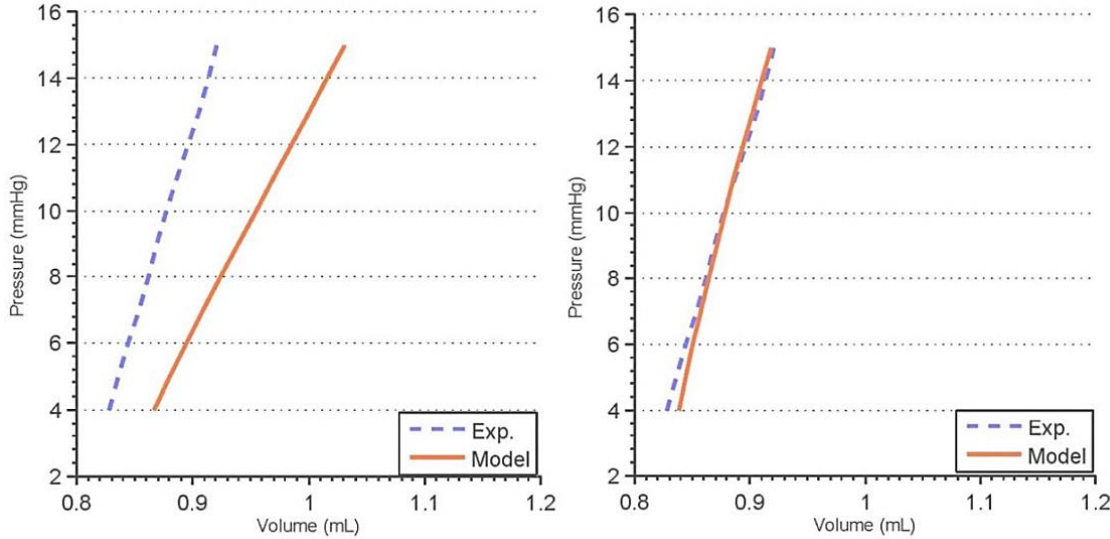


Fig. 7-14 PV-curves for a SHR rat at 12 months (model prediction and experimental data).
Left for $x_{endo} = x_{peri} = 1$ and right for $x_{endo} = 5$, $x_{peri} = 8$

In Fig. 7-14 PV-curves evaluated at $x_{endo} = x_{peri} = 1$ and $x_{endo} = 5$, $x_{peri} = 8$ for the novel parameter set obtained after 'M' and 'N' optimisation using the geometry of a WKY are shown. By changing the values of x_{endo} and x_{peri} , a stiffening and leftward shift of the model prediction towards the experimental PV-curve was predicted by the model.

The bivariate optimisation results are highly dependent on initial values for x_{endo} and x_{peri} (see Table 7-10) and give a similarly good fit to experimental PV data.

	initial x_{endo}	initial x_{peri}	optimised x_{endo}	optimised x_{peri}	resnorm
a	10	5	9.976	5.652	$2.899 \cdot 10^{-4}$
b	5	5	5.122	7.616	$2.825 \cdot 10^{-4}$
c	5	10	3.866	9.884	$2.889 \cdot 10^{-4}$

Table 7-10 Results for bivariate optimisation of x_{endo} and x_{peri}

In Fig. 7-15 FN, SF and NS curves evaluated using the optimised parameter sets of x_{endo} and x_{peri} are illustrated. The curves differ from each other dependent on the parameter set. This variability shows that fitting to PV-Curves is not capable of reproducing the orthotropic behaviour of myocardium in contrast to fitting to Dokos' shear data.

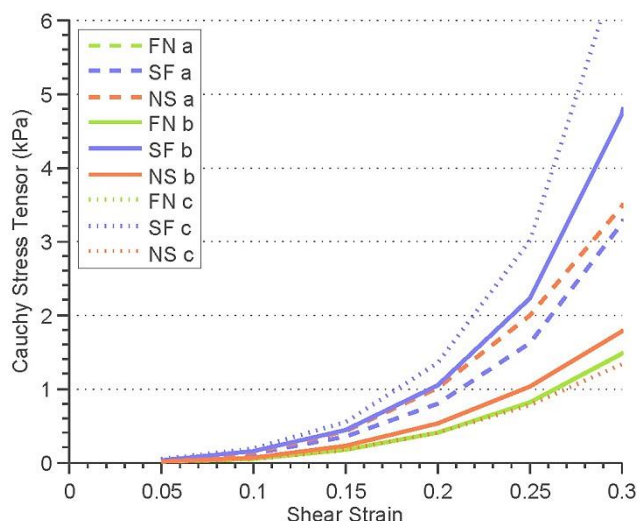


Fig. 7-15 FN, SF and NS curves for optimised parameter sets a, b and c as defined in Table 7-10

7.3.2.4 'M' and 'N' Parameter Estimation for SHR and WKY

As described in section 6.3 x_{endo} and x_{peri} were obtained from structural images. As x_{endo} is easier to determine, it was set to be 5 for the 'M' and 'N' optimisations. Three values for x_{peri} were chosen [6, 8, 10] and hence three optimisations were undertaken.

For $x_{endo} = 5$, $x_{peri} = 8$ the obtained values for 'M' and 'N' were $M = 1.285$ and $N = 0.126$ with a *resnorm* of 2.1e-3. In Fig. 7-16 the optimisation process for this case is shown. The left graph shows model predictions for SHR and WKY PV-curves versus the experimental data for each case, respectively, using the initial parameter set and setting all x_{endo} and x_{peri} to one. By changing the values of

x_{endo} and x_{peri} to the values obtained from the images the SHR curve shifted left towards the experimental PV-curve for the SHR case (graph in the middle). By performing the 'M' and 'N' optimisation both model predictions were shifted once more towards their experimental PV-curves.

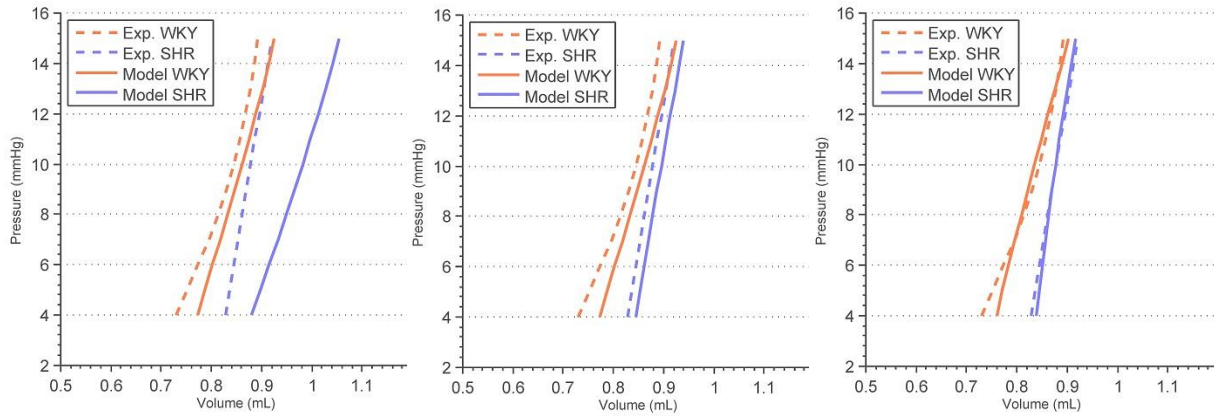


Fig. 7-16 Optimisation process: 1. model prediction vs. experimental data for $x_{peri} = x_{endo} = 1$ for both SHR and WKY for the initial parameter set; 2. $x_{endo} = 5$, $x_{peri} = 8$ for the SHR case; 3. output after bivariate optimisation

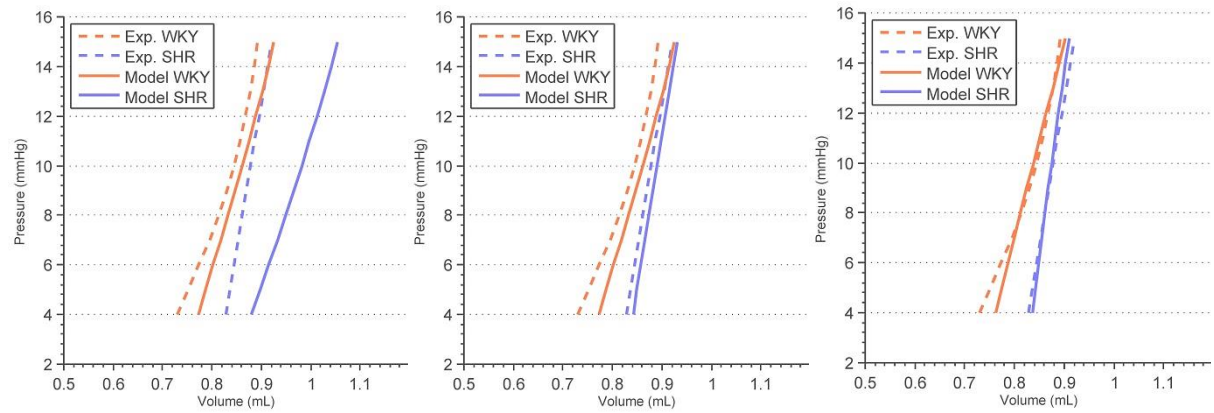


Fig. 7-17 Optimisation process: 1. model prediction vs. experimental data for $x_{peri} = x_{endo} = 1$ for both SHR and WKY for the initial parameter set; 2. $x_{endo} = 5$, $x_{peri} = 10$ for the SHR case; 3. output after bivariate optimisation

For $x_{endo} = 5$, $x_{peri} = 10$ the obtained values for 'M' and 'N' are $M = 1.229$ and $N = 0.507$, the *resnorm* is 2.5e-3. Fig. 7-17 shows the optimisation process. The middle graph shows that applying a value of ten for x_{peri} gave a slightly less good fit than eight, as the curve seems to be stiffer. However, the difference was not significant and the 'M' and 'N' optimisation gave a similar fit to experimental data as in the previous case.

A summary of the optimal parameter sets and goodness of fit for each case is given in Appendix 2B.

For all optimisations the upper part of the curves seemed to give a good fit, whereas the lower part (around 4 mmHg – 8 mmHg) did not improve. This can be

due to the initial offset that had to be applied at the end diastolic pressure of 6 mmHg to the experimental volumes (see section 5.6). This offset has been taken from the end diastolic volume (EDV) recorded for the individual rat geometries ($EDV_{WKY} = 0.774 \text{ ml}$, $EDV_{SHR} = 0.845 \text{ ml}$). The predicted EDV for the fitted models however was slightly higher than the recorded EDV, causing unsatisfactory volume alignment. Hence all ' M ' and ' N ' optimisations were run a second time, using the predicted model EDV gained by simulation of passive inflation using the initial parameter set (see Table 7-11). This ensured the alignment of model and experimental curves at 6 mmHg and made it possible for the optimiser to achieve a better fit to the data.

EDV	$x_{endo} = 5, x_{peri} = 6$	$x_{endo} = 5, x_{peri} = 8$	$x_{endo} = 5, x_{peri} = 10$
WKY [ml]	0.8028	0.8028	0.8028
SHR [ml]	0.8657	0.8606	0.8574

Table 7-11 EDV used for second optimisation

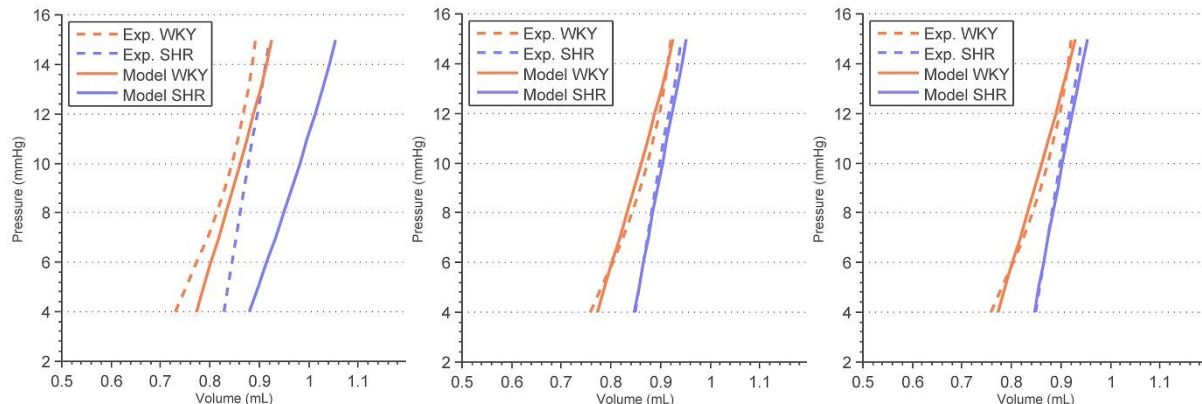


Fig. 7-18 1. model prediction vs. experimental data for $x_{peri} = x_{endo} = 1$ for both SHR and WKY for the initial parameter set; 2 $x_{endo} = 5, x_{peri} = 6$ for the SHR case; 3. output after bivariate optimisation

Fig. 7-18 and Fig. 7-19 show the results of the optimisations for $x_{endo} = 5$ and $x_{peri} = 6$ and $x_{endo} = 5$ and $x_{peri} = 10$, respectively. The fit for the SHR curve got better, the higher x_{peri} got, giving a very good fit for $x_{peri} = 10$. However, the curvature of the WKY curve was not captured by the model prediction for the WKY rat geometry.

In Fig. 7-20 model predictions for SHR and WKY compliance curves after the bivariate optimisation with $x_{endo} = 5, x_{peri} = 10$ are shown. The comparison between predicted and experimental WKY compliance showed once more that the curvature was not captured very well. Both compliance curves were quite flat

and especially the WKY compliance was not captured well. A summary of the obtained parameter sets and goodness of fit for each case is given in Appendix 2C.

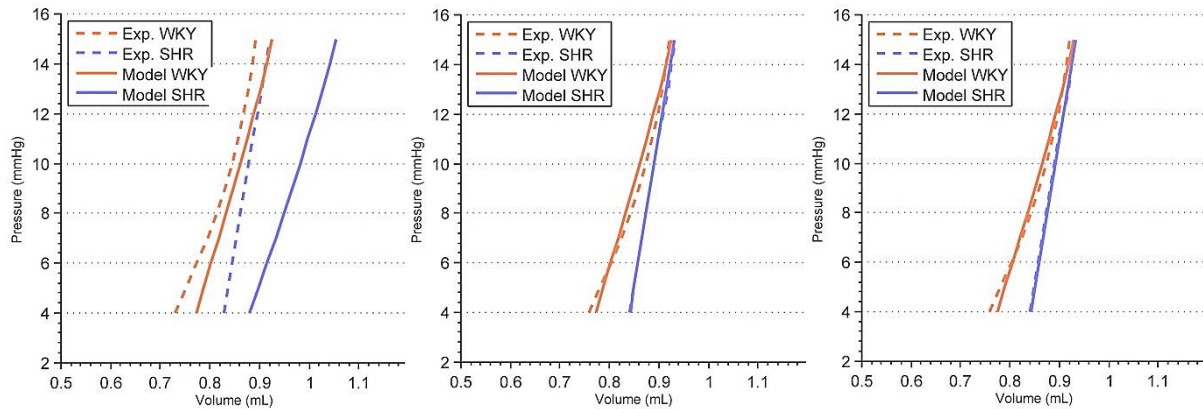


Fig. 7-19 1. model prediction vs. experimental data for $x_{peri} = x_{endo} = 1$ for both SHR and WKY for the initial parameter set; 2. $x_{endo} = 5$, $x_{peri} = 10$ for the SHR case; 3. output after bivariate optimisation

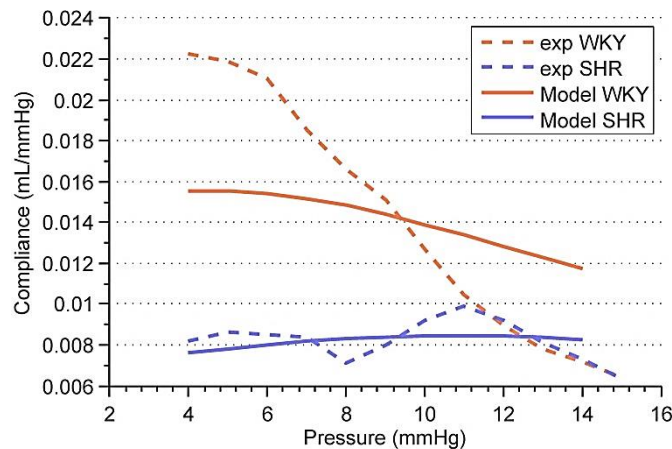


Fig. 7-20 Comparison between experimental and model prediction compliance curves, $x_{endo} = 5$, $x_{peri} = 10$

7.3.2.5 Bivariate fitting to Compliance Curves

Fitting to PV-Curves involved the application of a volume offset to the experimental PV data. Also, compliance curves did not align very well, although the fit to PV-curves suggested a good optimisation result.

Hence in a second approach passive inflation was simulated and compliance curves were then compared between model prediction and experimental data to further optimise material parameters. The procedure was similar to the bivariate optimisation approach as described in section 5.6, except that the objective function was calculated by a vector of model predicted and experimental compliance values.

Fig. 7-21 shows the optimisation result for $x_{endo} = 5$, $x_{peri} = 10$. The obtained values for 'M' and 'N' were $M = 0.706$ and $N = 1.824$ with a *resnorm* of 1.0 e-4. The compliance curve for the WKY case was still not able to represent the experimental behaviour, although the curves aligned better than after fitting to PV-curves.

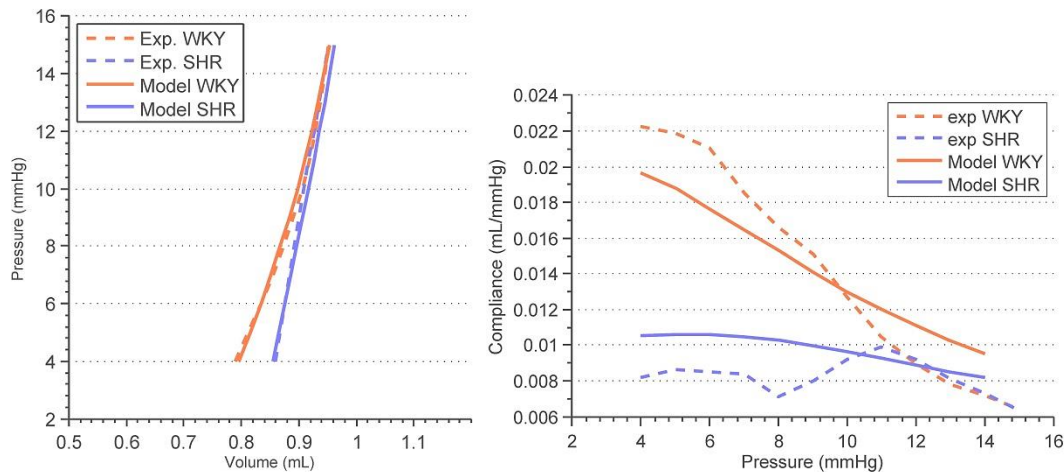


Fig. 7-21 Result of 'M' and 'N' optimisation for $x_{endo} = 5$, $x_{peri} = 10$ after fitting to experimental compliance curves

7.3.2.6 Parameter Sensitivity Analysis

It was not able to reproduce the compliance curves for the healthy case sufficiently using bivariate optimisation. Hence a parameter sensitivity analysis was carried out to investigate how each parameter contributes to the model fit. Knowing about the contributions an efficient new optimisation approach could be developed without having to optimise all eight parameters.

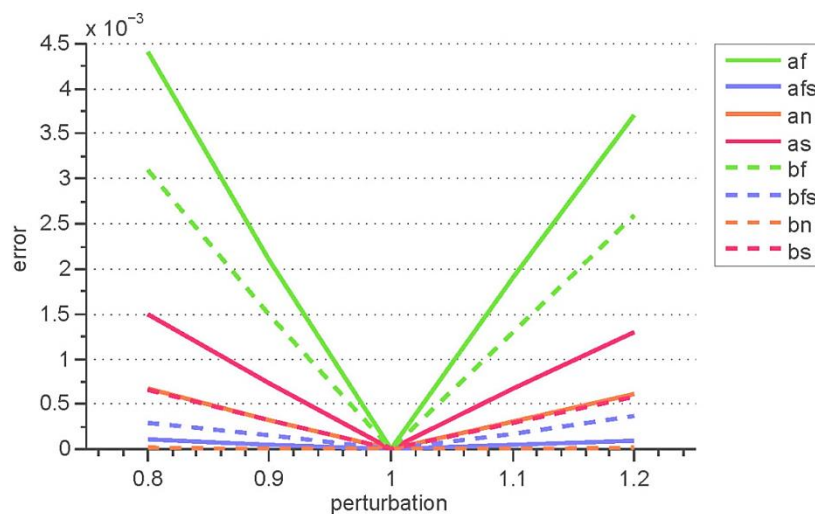


Fig. 7-22 Root mean square errors for parameter sets as a function of parameter proportions

The parameter set for $x_{endo} = 5$, $x_{peri} = 10$ obtained in the previous section after fitting the compliance curve was used to generate synthetic compliance data. Perturbations of $\pm 10\%$ and $\pm 20\%$ were applied to each parameter separately and the model is solved for each case. Subsequently the RMS (root mean square error) was calculated with respect to the synthetic data.

In Fig. 7-22 the results of the perturbations are illustrated and suggest that a_f and b_f dominate the response.

7.3.2.7 Multivariate Fitting to Compliance Curves

As shown above, a_f and b_f are the dominating parameters. Hence a second, multivariate optimisation was undertaken, optimising all parameters as in the bivariate optimisation except a_f and b_f , which were optimised separately. This results in four parameters that have to be optimised.

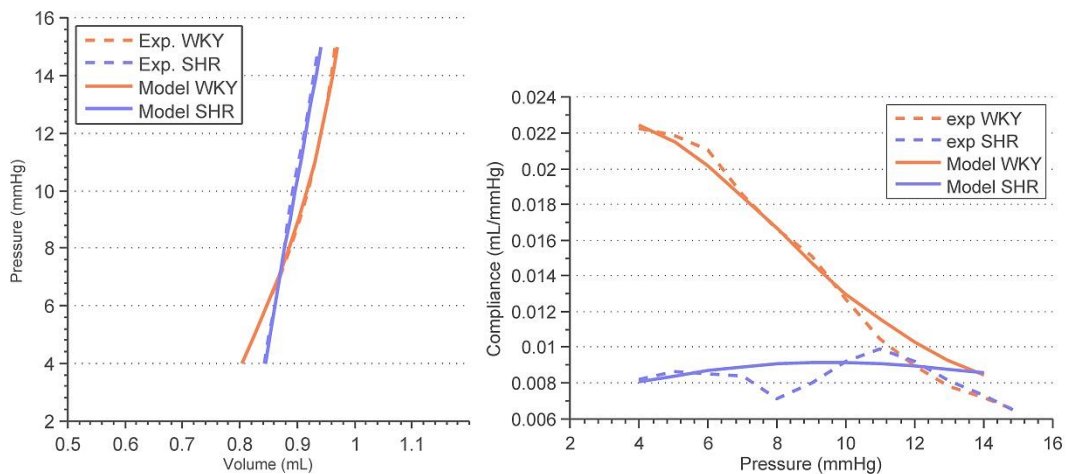


Fig. 7-23 Result of ' M ', ' N ', ' O ', ' P ' optimisation for $x_{endo} = 5$, $x_{peri} = 10$ after fitting to experimental compliance curves

The parameters input to CellML and CMISS became:

$$[Oa_f, Ma_{fs}, Ma_n, Ma_s, Pb_f, Nb_{fs}, Nb_n, Nb_s]$$

Using $x_{endo} = 5$ and $x_{peri} = 10$ the optimisation resulted in ' M ' = 1.337, ' N ' = 0.646, ' O ' = 0.471, ' P ' = 2.389 and a *resnorm* of 2.61e-05. The resulting PV and compliance curves after multivariate optimisation are shown in Fig. 7-23.

For $x_{endo} = 5$ and $x_{peri} = 8$ the fit for the SHR case got worse compared to $x_{peri} = 10$, resulting in a *resnorm* of 3.61e-5 with ' M ' = 1.451, ' N ' = 0.717, ' O ' = 0.470 and ' P ' = 2.423.

A summary of the obtained parameter sets and goodness of fit for each case is given in Appendix 2D.

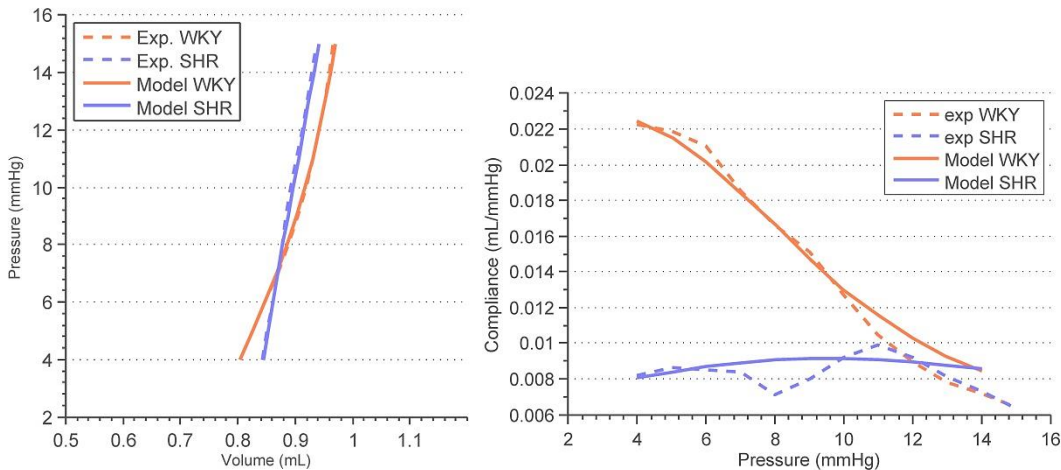


Fig. 7-24 Result of ' M' , ' N ', ' O ', ' P ' optimisation for $x_{endo} = 5$, $x_{peri} = 8$ after fitting to experimental compliance curves

Fig. 7-25 shows the results for $x_{endo} = x_{peri} = 1$ after a multivariate optimisation. It becomes clear that without the application of x_{endo} and x_{peri} it was not possible to obtain a good fit to both healthy and diseased compliance curves.

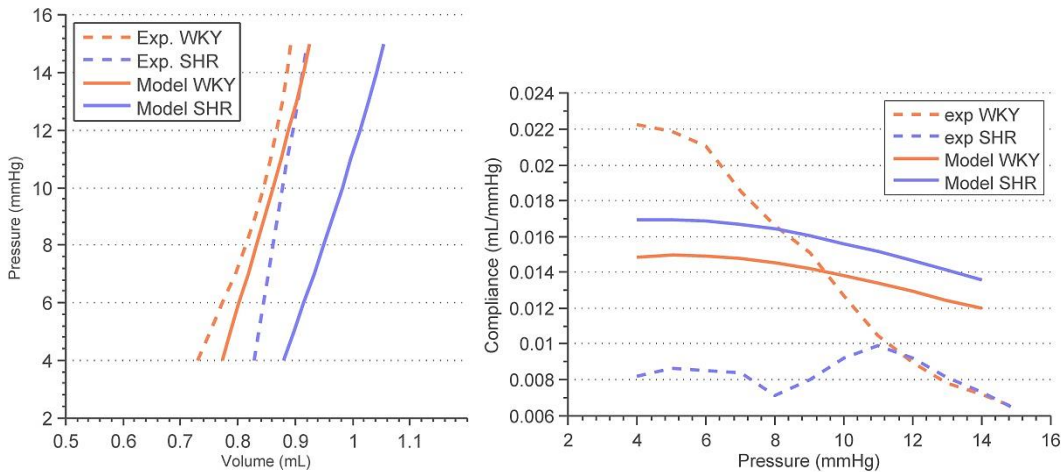


Fig. 7-25 Result of ' M' , ' N ', ' O ', ' P ' optimisation for $x_{endo} = 1$, $x_{peri} = 1$ after fitting to experimental compliance curves

To further reduce the number of parameters that had to be optimised the optimisation was undertaken by using three parameters ' M ', ' N ' and ' O '. The latter either multiplied a_f or b_f and the parameters input to CellML and CMISS became

$$[Oa_f, Ma_{fs}, Ma_n, Ma_s, Nb_f, Nb_{fs}, Nb_n, Nb_s]$$

or

$$[Ma_f, Ma_{fs}, Ma_n, Ma_s, Ob_f, Nb_{fs}, Nb_n, Nb_s].$$

Optimising a_f separately resulted in ' M ' = 1.350, ' N ' = 2.465 and ' O ' = 0.397 with a *resnorm* of 2.49 e-5, whereas optimising b_f separately resulted in ' M ' = 0.717, ' N ' = 1.242 and ' O ' = 1.915 with a *resnorm* of 9.67 e-5. The fits are shown in Fig.

7-26 and Fig. 7-27. The goodness of fit for the optimisation of a_f separately resulted in a similarly good fit as optimising four parameters, whereas optimising b_f separately did not reproduce the curves sufficiently. Hence optimising three parameters, multiplying a_f with 'O' was capable of reproducing the pressure-volume curves.

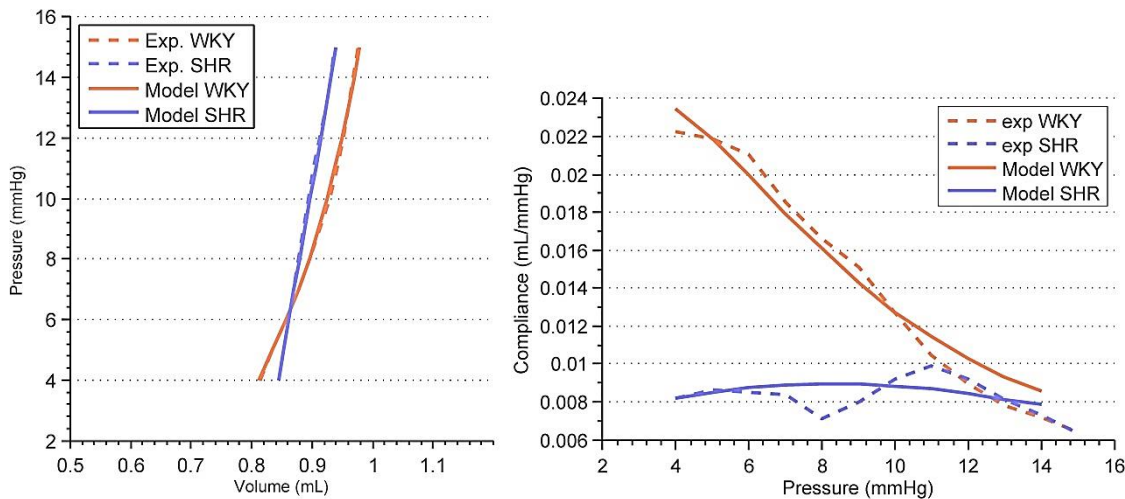


Fig. 7-26 Results of 'M', 'N', 'O*a_f' optimisation for $x_{endo} = 5$, $x_{peri} = 8$ after fitting to experimental compliance curves

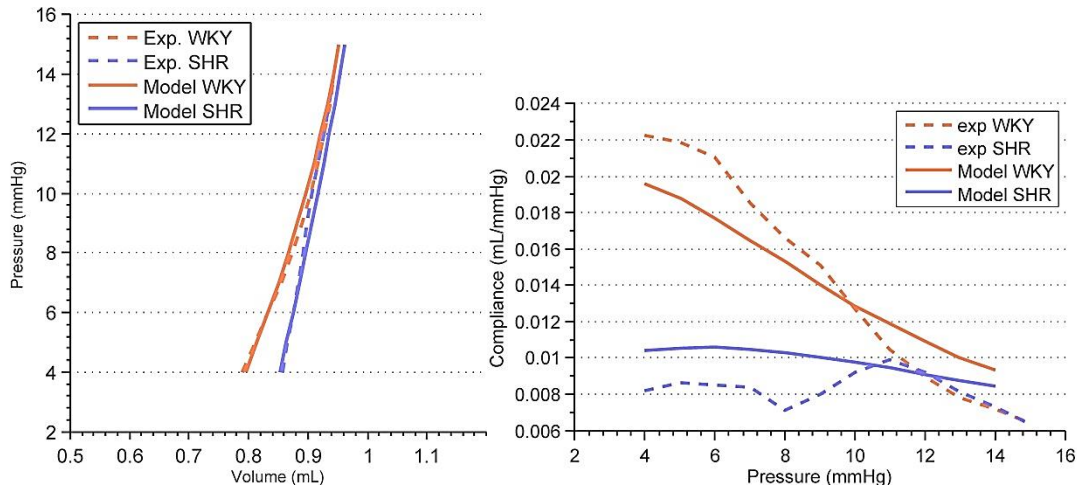


Fig. 7-27 Results of 'M', 'N', 'O*b_f' optimisation for $x_{endo} = 5$, $x_{peri} = 8$ after fitting to experimental compliance curves

7.3.3 Conclusion and Discussion

Subsequently simulation results are summarised and discussed and a conclusion is given.

7.3.3.1 Analytical Implementation

The results of simulation of simple shear are consistent with the expectations. As the sheet direction is initially stiffer than the normal direction, applying x_{peri} in the sheet-direction-term results in a high stiffness at a shear strain amount of 50 %. The response in the normal direction also becomes stiffer, as considered to happen due to the elevated amount of endomysial collagen.

7.3.3.2 FE Analysis

The global response to the application of x_{endo} and x_{peri} is also consistent with the expectations. The higher the values of x_{endo} or x_{peri} were, the higher was the stiffness of the PV-curves.

The theoretical estimation of x_{endo} and x_{peri} by optimising both values shows that an optimal fit to experimental data is possible with physiologically explainable values for both parameters. However, the optimal parameter space is very flat and it becomes clear, that only fitting to PV-curves does not take the orthotropic behaviour of myocardium into account (see Fig. 7-15).

It should be noted that a variation of x_{peri} from six to ten has a large influence of the steepness of the predicted PV-curves. It results in a significant stiffening of the PV-curves with higher values for x_{peri} .

7.3.3.3 Bivariate Optimisation

The bivariate optimisation for both WKY and SHR geometry simultaneously gives a good fit for the upper part of both PV-curves. The fit for the lower parts (4 mmHg to 8 mmHg) nevertheless does not seem to improve. This is most likely due to the definition of the initial offset applied to the experimental data. Additionally a bivariate optimisation does not provide enough free parameters to give a good fit throughout the curve. Also the experimental PV-curve used is not obtained from the same animal as the geometric data.

Hence, all 'M' and 'N' optimisations were re-run, using the predicted model EDV gained by simulation of passive inflation using the initial parameter set (see Table 7-11). The fits to the experimental PV-curves were better than the previous case. However, the 'M' and 'N' optimisation was not able to give a good fit to the WKY

curve as the curvature is not able to be matched by applying just two global scaling factors.

7.3.3.4 Fitting to Compliance Curves

Fitting to PV-curves included applying a volume offset to the experimental data, which is a big disadvantage, as the alignment of experimental data to the model is arbitrary. Hence, a second approach was chosen that involved fitting directly to experimental compliance curves. The bivariate optimisation was able to represent the experimental compliance curves better than fitting to PV-curves. However, a simple bivariate approach could not sufficiently capture the experimental compliance of the WKY rat.

Therefore a four parameter optimisation was undertaken. The error was significantly smaller than errors during fitting to PV-curves ($resnorm = 7.24e-4$ for the PV-fitting in comparison to $resnorm = 2.06e-5$ for the multivariate optimisation while fitting to compliance curves). The curvature of both healthy and diseased case is able to be captured with this approach.

Utilizing a three parameter optimisation, multiplying ' M ' and ' N ' with all ' a ' and ' b ' parameters except with a_f , which was multiplied by ' O ', gives a similarly well fit to experimental data as the four parameter estimation.

However, the values of ' M ', ' N ', ' O ' and ' P ' cannot be given any physical meaning, as fitting to compliance curves is not capable of representing the orthotropic behaviour of myocardium. If it was possible to fit to shear data of diseased myocardium instead an attempt to analyse these values would be reasonable.

7.3.3.5 Conclusion

The introduction of x_{endo} and x_{peri} gives the desired response as they result in reasonably good fits to experimental data for both WKY and SHR cases using one parameter set, especially for $x_{peri} = 10$. Hence the structure of the equation gives the desired feature of being capable of representing both healthy and diseased myocardium.

It is important to note that the simulations are only undertaken for two animal geometries and hence they only show that the equation is capable of representing these two cases. Future work should hence include applying the new constitutive equation on more cases. Also values for x_{endo} and x_{peri} should be obtained from more images than just from one as perimysial and endomysial collagen amounts can differ from case to case.

8 Summary and Future Work

In this thesis a novel biophysical constitutive model was developed that is capable of modelling the passive mechanical behaviour of myocardial tissue during diastolic HF. To assist with constitutive model development, cine MRI, confocal microscopy images and ex-vivo pressure-volume relations of rat hearts were utilized.

The remodelling of endomysial and perimysial collagen significantly influences significantly the mechanical response along the normal and sheet direction, respectively. Thus it can be concluded that collagen remodelling has a major impact on the passive mechanical behaviour of the LV during the progression towards diastolic HF.

Two structural parameters that reflected the thickening of perimysial and endomysial collagen were defined and values for both were determined from high resolution confocal structural images. The parameters were then incorporated in a modified existing constitutive equation. By using only one set of mechanical properties for the healthy as well as the diseased case but utilizing the two structural parameters obtained directly from confocal images of diseased hearts, it was possible to represent the passive LV mechanics of both the healthy and diseased hearts.

A limitation of this work was the lack of sufficient experimental data. Only one geometry for a WKY rat and one geometry for a SHR at 12 months were used for fitting to PV and compliance curves. Also the available PV data did not belong to the available geometries but was obtained from previous studies. Furthermore there was no geometry available for 18 and 22 months old rats; hence it was not possible to investigate the progression towards systolic HF. More data for older rats is presently being acquired and will be available for future work. This may make it possible to examine the effects of the dispersion model. In the future PV data should be available for each geometry, so that fitting to PV- or compliance curves can be more subject specific.

Another limitation is the utilization of a 4 DOF single element model. The accuracy of the geometric representation of each age-specific model is limited

due to the limited number of geometric DOF. Future work will include a 16-element model that will give a better fit to cine MRI data.

The data available for passive inflation of the LV was only available above 4 mmHg and hence the compliance curves were only possible to be calculated above 4 mmHg. As the model prediction of compliance beneath 4 mmHg were ascending first and descending afterwards it is not possible yet to verify whether this behaviour is physiological or not. PV-data that is being presently recorded includes pressures below 4 mmHg and hence a comparison will be possible in the future.

Another disadvantage of this study is the lack of adequate shear- and biaxial extension data for healthy and diseased rat myocardium. Fitting to PV- and compliance curves is not sufficient to capture the orthotropic behaviour of myocardium as it only represents the bulk mechanical behaviour. Hence, values obtained via bivariate- or multivariate fitting could not be interpreted to gain deeper understanding of the on-going changes during diastolic HF. Experiments should be developed to gain information about biaxial extension of living myocardial tissue. Also shear data for diseased myocardium would be useful to gain information about how the mechanical behaviour in each direction changes with on-going remodelling. With this information the M and N parameters gained by the optimisations could be interpreted for each direction and hence a deeper understanding of remodelling in each material direction could be gained.

The analysis of the structural images was only done manually and should be analysed automatically in the future to guarantee a more reproducible and objective analysis. Although incorporating the thickening of endomysial and perimysial collagen seems to be sufficient to describe the differences between normal and diastolic HF tissue, the behaviour of other components of the ECM should also be considered. There is a significant amount of scar tissue and vessels that are not aligned with material directions and are hence not considered here. Furthermore, only one image for each case was analysed. Subsequent work should include the computational analysis of a number of images for healthy and diseased cases to gain statistical values for the estimated structural parameters. The inclusion of other components apart from collagen should also be considered.

Incorporating the smallest possible changes and to ensure convexity of the equation is not violated the equation was only modified in sheet and normal direction. In the future the influence of constituents in fibre and also in the shearing terms should be considered. Also, no additional coupling terms for fibre-

normal and sheet-normal direction were added. A possible addition of these terms should be considered in future work as well.

As the influences of each component of the myocardium is not known, future work could include stepping back and utilizing a FEM model of a single cube which incorporates the structure that can be seen on the available structural images. Simulations on this cube could contribute to understanding of how each component contributes to myocardial mechanical behaviour.

In this study, structural parameters which directly reflect the structural remodelling were incorporated in an existing passive orthotropic constitutive model. Material parameters were then estimated to match *in vitro* passive PV data. With the addition of the structural parameters it was possible to identify one set of material parameters which described the mechanical behaviour of both healthy and diseased hearts. Utilising a computational modelling framework like this will eventually allow examining the effects of individual factors on ventricular dysfunction at different stages of HF.

9 Nomenclature

CMISS	Continuum Mechanics, Image analysis, Signal processing and System Identification
CIM	Cardiac Image Modeller
DOF	Degrees of Freedom
ECM	Extra Cellular Matrix
EDV	End Diastolic Volume
EVCM	Extended Volume Confocal Microscopy Imaging
FE	Finite Element
FEM	Finite Element Modelling
HFpEF	Heart Failure with Preserved Ejection Fraction
HFrEF	Heart Failure with Reduced Ejection Fraction
HHD	Hypertensive Heart Disease
LA	Left Atrium
LV	Left Ventricle
MRI	Magnetic Resonance Imaging
PV	Pressure Volume
RA	Right Atrium
RMSE	Root Mean Square Error
RV	Right Ventricle
SALS	Small Angle Light Scattering
SHR	Spontaneously Hypertensive Rat
SPAMM	Spatial Modulation of Magnetization
SV	Stroke Volume

SW Stroke Work

WKY Wistar-Kyoto Rat

10 References

- [1] A. J. Pope, "Characterising myocardial remodelling in hypertensive heart disease. Structural and functional changes in the spontaneously hypertensive rat." *PhD Thesis, the University of Auckland, New Zealand (Supervisors: Smaill BH, LeGrice IJ)*, 2011.
- [2] V. Y. Wang, "Modelling In Vivo Cardiac Mechanics using MRI and FEM," 2012.
- [3] G. B. Sands, B. H. Smaill and I. J. LeGrice, "Virtual sectioning of cardiac tissue relative to fibre orientation," in *Engineering in Medicine and Biology Society, 2008. EMBS 2008. 30th Annual International Conference of the IEEE*, 2008, pp. 226-229.
- [4] G. A. Holzapfel and R. W. Ogden, "Constitutive modelling of passive myocardium: a structurally based framework for material characterization," *Philosophical Transactions of the Royal Society A: Mathematical, Physical and Engineering Sciences*, vol. 367, pp. 3445-3475, 2009.
- [5] J. Daut, "Herzmechanik," *Physiologie Des Menschen*, pp. 539-564, 2011.
- [6] E. E. Selkurt, *Physiology*. Boston: Little, Brown and Company, 1984.
- [7] Wikimedia Commons, "Wiggers Diagram," vol. 2013, 20 March 2012, 2012.
- [8] R. Klabunde, *Cardiovascular Physiology Concepts*. LWW, 2011.
- [9] A. J. Pope, G. B. Sands, B. H. Smaill and I. J. LeGrice, "Three-dimensional transmural organization of perimysial collagen in the heart," *American Journal of Physiology-Heart and Circulatory Physiology*, vol. 295, pp. H1243-H1252, 2008.
- [10] A. V. Panfilov and A. V. Holden, *Computational Biology of the Heart*. John Wiley & Sons, 1997.
- [11] M. Nash and P. Hunter, "Regional mechanics of the beating heart," in *Cardiac Perfusion and Pumping Engineering*, D. N. Ghista and Y. E. Ng, Eds. World Scientific, 2007.
- [12] I. J. LeGrice, B. Smaill, L. Chai, S. Edgar, J. Gavin and P. J. Hunter, "Laminar structure of the heart: ventricular myocyte arrangement and connective tissue

- architecture in the dog," *American Journal of Physiology-Heart and Circulatory Physiology*, vol. 269, pp. H571-H582, 1995.
- [13] M. P. Nash and P. J. Hunter, "Computational mechanics of the heart," *Journal of Elasticity*, vol. 61, pp. 113-141, 2000.
- [14] C. S. Lam, E. Donal, E. Kraigher-Krainer and R. S. Vasan, "Epidemiology and clinical course of heart failure with preserved ejection fraction," *European Journal of Heart Failure*, vol. 13, pp. 18-28, 2011.
- [15] S. S. Najjar, "Heart Failure With Preserved Ejection Fraction: Failure to Preserve, Failure of Reserve, and Failure on the Compliance Curve," *J. Am. Coll. Cardiol.*, vol. 54, pp. 419-421, 2009.
- [16] B. A. Borlaug, M. M. Redfield, G. De Keulenaer and D. L. Brutsaert, "Diastolic and Systolic Heart Failure Are Distinct Phenotypes Within the Heart Failure SpectrumResponse to Borlaug and Redfield," *Circulation*, vol. 123, pp. 2006-2014, 2011.
- [17] G. W. De Keulenaer, D. L. Brutsaert, B. A. Borlaug and M. M. Redfield, "Systolic and Diastolic Heart Failure Are Overlapping Phenotypes Within the Heart Failure SpectrumResponse to De Keulenaer and Brutsaert," *Circulation*, vol. 123, pp. 1996-2005, 2011.
- [18] I. J. LeGrice, A. J. Pope, G. B. Sands, G. Whalley, R. N. Doughty and B. H. Smaill, "Progression of myocardial remodeling and mechanical dysfunction in the spontaneously hypertensive rat," *American Journal of Physiology-Heart and Circulatory Physiology*, vol. 303, pp. H1353-H1365, 2012.
- [19] N. M. Albert, C. A. Eastwood and M. L. Edwards, "Evidence-based practice for acute decompensated heart failure," *Crit. Care Nurse*, vol. 24, pp. 14-29, 2004.
- [20] M. H. Drazner, "The progression of hypertensive heart disease," *Circulation*, vol. 123, pp. 327-334, 2011.
- [21] J. D. Humphrey and F. C. Yin, "On constitutive relations and finite deformations of passive cardiac tissue: I. A pseudostrain-energy function," *J. Biomech. Eng.*, vol. 109, pp. 298-304, Nov, 1987.
- [22] J. Guccione, A. McCulloch and L. Waldman, "Passive material properties of intact ventricular myocardium determined from a cylindrical model," *J. Biomech. Eng.*, vol. 113, pp. 42, 1991.
- [23] P. Hunter, S. Sideman and H. Fozzard, "Myocardial constitutive laws for continuum mechanics models of the heart," *Adv. Exp. Med. Biol.*, vol. 382, pp. 303-318, 1995.

- [24] K. D. Costa, J. W. Holmes and A. D. McCulloch, "Modelling cardiac mechanical properties in three dimensions," *Philosophical Transactions of the Royal Society of London.Series A: Mathematical, Physical and Engineering Sciences*, vol. 359, pp. 1233-1250, 2001.
- [25] H. Schmid, M. P. Nash, A. A. Young and P. J. Hunter, "Myocardial material parameter estimation-a comparative study for simple shear," *J. Biomech. Eng.*, vol. 128, pp. 742-750, Oct, 2006.
- [26] E. Nevo and Y. Lanir, "Structural finite deformation model of the left ventricle during diastole and systole." *J. Biomech. Eng.*, vol. 111, pp. 342, 1989.
- [27] Y. Lanir, "Constitutive equations for fibrous connective tissues," *J. Biomech.*, vol. 16, pp. 1-12, 1983.
- [28] M. S. Sacks, "Incorporation of experimentally-derived fibre orientation into a structural constitutive model for planar collagenous tissues," *J. Biomech. Eng.*, vol. 125, pp. 280-287, Apr, 2003.
- [29] H. Wang, X. Luo, H. Gao, R. Ogden, B. Griffith, C. Berry and T. Wang, "A modified Holzapfel-Ogden law for a residually stressed finite strain model of the human left ventricle in diastole," *Biomechanics and Modeling in Mechanobiology*, pp. 1-15, 2013.
- [30] T. S. Eriksson, A. J. Prassl, G. Plank and G. A. Holzapfel, "Modeling the dispersion in electromechanically coupled myocardium," *International Journal for Numerical Methods in Biomedical Engineering*, vol. 11, pp 1267-1284, 2013.
- [31] T. C. Gasser, R. W. Ogden and G. A. Holzapfel, "Hyperelastic modelling of arterial layers with distributed collagen fibre orientations," *Journal of the Royal Society Interface*, vol. 3, pp. 15-35, 2006.
- [32] W. J. Karlon, J. W. Covell, A. D. McCulloch, J. J. Hunter and J. H. Omens, "Automated measurement of myofibre disarray in transgenic mice with ventricular expression of ras," *Anat. Rec.*, vol. 252, pp. 612-625, 1998.
- [33] G. A. Holzapfel and R. W. Ogden, "Constitutive modelling of arteries," *Proceedings of the Royal Society A: Mathematical, Physical and Engineering Science*, vol. 466, pp. 1551-1597, 2010.
- [34] C. Westbrook and C. K. Roth, *MRI in Practice*. Wiley-Blackwell, 2013.
- [35] S. Dokos, B. H. Smaill, A. A. Young and I. J. LeGrice, "Shear properties of passive ventricular myocardium," *American Journal of Physiology-Heart and Circulatory Physiology*, vol. 283, pp. H2650-H2659, 2002.

- [36] G. A. Holzapfel, *Nonlinear Solid Mechanics: A Continuum Approach for Engineering*. John Wiley & Sons Ltd., 2000.
- [37] H. Schmid, M. Nash, A. Young, O. Rohrle and P. Hunter, "A Computationally Efficient Optimization Kernel for Material Parameter Estimation Procedures," *Transactions-American Society of Mechanical Engineers Journal of Biomechanical Engineering*, vol. 129, pp. 279, 2007.
- [38] P. Nielsen, I. Le Grice, B. Smaill and P. Hunter, "Mathematical model of geometry and fibrous structure of the heart," *American Journal of Physiology-Heart and Circulatory Physiology*, vol. 260, pp. H1365-H1378, 1991.
- [39] O. H. Cingolani, X. Yang, M. A. Cavasin and O. A. Carretero, "Increased systolic performance with diastolic dysfunction in adult spontaneously hypertensive rats," *Hypertension*, vol. 41, pp. 249-254, 2003.
- [40] T. Eriksson, G. Plank and G. Holzapfel, "A structurally motivated model for myocardium fibre and sheet disarray," in *8th European Solid Mechanics Conference (ESMC)*, Graz, Austria, 2012.
- [41] H. Wang, H. Gao, X. Luo, C. Berry, B. Griffith, R. Ogden and T. Wang, "Structure-based finite strain modelling of the human left ventricle in diastole," *International Journal for Numerical Methods in Biomedical Engineering*, vol. 29, pp. 83-103, 2013.
- [42] S. Huang, "Modelling cardiac remodelling - the effect of structural changes on the cardiac mechanical function in the SHR", *Bachelors Dissertation Project*, The University of Auckland, 2013.
- [43] R. W. Ogden, "Nonlinear elasticity, anisotropy, material stability and residual stresses in soft tissue," *Courses and Lectures - International Centre for Mechanical Sciences*, pp. 65-108, 2003.
- [44] G. A. Holzapfel, T. C. Gasser and R. W. Ogden, "A new constitutive framework for arterial wall mechanics and a comparative study of material models," *Journal of Elasticity and the Physical Science of Solids*, vol. 61, pp. 1-48, 2000.

11 Appendix

11.1 Appendix 1A

Derivation of the 2nd Piola Kirchhoff Stress tensor components from Holzapfel's strain energy function augmented with the sheet distribution parameter κ_s (see section 6.1).

$$\bar{W} = \frac{a}{2b} \exp[b(I_1 - 3)] + \sum_{i=f,s} \frac{a_i}{2b_i} \{\exp[b_i(I_{4i}^* - 1)^2] - 1\} + \frac{a_{fs}}{2b_{fs}} [\exp(b_{fs}I_{8fs}^2) - 1]$$

Rewrite the invariants in terms of the Green-Lagrangian Strain tensor components \mathbf{E} .

$$\mathbf{E} = \frac{1}{2}(\mathbf{C} - \mathbf{I})$$

$$I_1 = \text{tr}(\mathbf{C}) = C_{ff} + C_{ss} + C_{nn} = 2E_{ff} + 2E_{ss} + 2E_{nn} + 3$$

$$I_{4f}^* = f_0 \cdot (Cf_0) = \begin{bmatrix} 1 \\ 0 \\ 0 \end{bmatrix} \cdot \left(\begin{bmatrix} C_{ff} & C_{fs} & C_{fn} \\ C_{sf} & C_{ss} & C_{sn} \\ C_{nf} & C_{ns} & C_{nn} \end{bmatrix} \begin{bmatrix} 1 \\ 0 \\ 0 \end{bmatrix} \right) = C_{ff} = 2E_{ff} + 1$$

$$I_{8fs} = f_0 \cdot (Cs_0) = \begin{bmatrix} 1 \\ 0 \\ 0 \end{bmatrix} \cdot \left(\begin{bmatrix} C_{ff} & C_{fs} & C_{fn} \\ C_{sf} & C_{ss} & C_{sn} \\ C_{nf} & C_{ns} & C_{nn} \end{bmatrix} \begin{bmatrix} 0 \\ 1 \\ 0 \end{bmatrix} \right) = C_{fs} = 2E_{fs}$$

$$I_{4s} = s_0 \cdot (Cs_0) = \begin{bmatrix} 0 \\ 1 \\ 0 \end{bmatrix} \cdot \left(\begin{bmatrix} C_{ff} & C_{fs} & C_{fn} \\ C_{sf} & C_{ss} & C_{sn} \\ C_{nf} & C_{ns} & C_{nn} \end{bmatrix} \begin{bmatrix} 0 \\ 1 \\ 0 \end{bmatrix} \right) = C_{ss} = 2E_{ss} + 1$$

$$\begin{aligned} I_{4s}^* &= \kappa_s I_1 + (1 - 3\kappa_s) I_{4s} = \kappa_s (2E_{ff} + 2E_{ss} + 2E_{nn} + 3) + (1 - 3\kappa_s)(2E_{ss} + 1) \\ &= 2\kappa_s (E_{ff} + E_{nn}) + 2E_{ff}(1 - 2\kappa_s) + 1 \end{aligned}$$

Calculate the 2nd Piola Kirchhoff stress tensor components using Equation 11-1 to describe passive deformation.

Equation 11-1

$$\mathbf{T}^{MN} = \frac{1}{2} \left(\frac{\partial W}{\partial E_{MN}} + \frac{\partial W}{\partial E_{NM}} \right) - p \frac{\partial X_M}{\partial x_k} \frac{\partial X_N}{\partial x_k}$$

$$T_{dev}^{ff} = a \cdot \exp \left(2b(E_{ff} + E_{ss} + E_{nn}) \right) + 4E_{ff}a_f \cdot \exp(4b_f E_{ff}^2) + 4a_s((E_{ff} + E_{nn})\kappa_s^2 + E_{ss}(\kappa_s - 2\kappa_s^2)) \cdot \exp \left(4b_s(\kappa_s(E_{ff} + E_{nn}) + E_{ss}(1 - 2\kappa_s))^2 \right)$$

$$T_{dev}^{ss} = a \cdot \exp \left(2b(E_{ff} + E_{ss} + E_{nn}) \right) + 4a_s((E_{ff} + E_{nn})(\kappa_s - 2\kappa_s^2) + E_{ss}(1 - 4\kappa_s + 4\kappa_s^2)) \cdot \exp \left(4b_s(\kappa_s(E_{ff} + E_{nn}) + E_{ss}(1 - 2\kappa_s))^2 \right)$$

$$T_{dev}^{nn} = a \cdot \exp \left(2b(E_{ff} + E_{ss} + E_{nn}) \right) + 4a_s((E_{ff} + E_{nn})\kappa_s^2 + E_{ss}(\kappa_s - 2\kappa_s^2)) \cdot \exp \left(4b_s(\kappa_s(E_{ff} + E_{nn}) + E_{ss}(1 - 2\kappa_s))^2 \right)$$

$$T_{dev}^{fs} = T_{dev}^{sf} = 2a_{fs}E_{fs} \cdot \exp(4b_{fs}E_{fs}^2)$$

$$T_{dev}^{fn} = T_{dev}^{nf} = 0$$

$$T_{dev}^{sn} = T_{dev}^{ns} = 0$$

11.2 Appendix 1B

Derivation of the 2nd Piola Kirchhoff Stress tensor components from Equation 11-2 (see section 6.2).

Equation 11-2

$$\begin{aligned}\bar{W} = & \frac{a_s}{2b_s} [\exp(b_s(x_{endo}I_{4s} - 1)^2) - 1] + \frac{a_f}{2b_f} [\exp(b_f(x_{endo}I_{4f} - 1)^2) - 1] \\ & + \frac{a_n}{2b_n} [\exp(b_n(x_{peri}I_{4n} - 1)^2) - 1] + \frac{a_{fs}}{2b_{fs}} [\exp(b_{fs}I_{8fs}^2) - 1]\end{aligned}$$

Rewrite new invariants in terms of Green's strain tensor \mathbf{E} .

$$\mathbf{E} = \frac{1}{2}(\mathbf{C} - \mathbf{I})$$

$$I_{4f} = f_0 \cdot (Cf_0) = \begin{bmatrix} 1 \\ 0 \\ 0 \end{bmatrix} \cdot \left(\begin{bmatrix} C_{ff} & C_{fs} & C_{fn} \\ C_{sf} & C_{ss} & C_{sn} \\ C_{nf} & C_{ns} & C_{nn} \end{bmatrix} \begin{bmatrix} 1 \\ 0 \\ 0 \end{bmatrix} \right) = C_{ff} = 2E_{ff} + 1$$

$$I_{4s} = s_0 \cdot (Cs_0) = \begin{bmatrix} 0 \\ 1 \\ 0 \end{bmatrix} \cdot \left(\begin{bmatrix} C_{ff} & C_{fs} & C_{fn} \\ C_{sf} & C_{ss} & C_{sn} \\ C_{nf} & C_{ns} & C_{nn} \end{bmatrix} \begin{bmatrix} 0 \\ 1 \\ 0 \end{bmatrix} \right) = C_{ss} = 2E_{ss} + 1$$

$$I_{4n} = n_0 \cdot (Cn_0) = \begin{bmatrix} 0 \\ 0 \\ 1 \end{bmatrix} \cdot \left(\begin{bmatrix} C_{ff} & C_{fs} & C_{fn} \\ C_{sf} & C_{ss} & C_{sn} \\ C_{nf} & C_{ns} & C_{nn} \end{bmatrix} \begin{bmatrix} 0 \\ 0 \\ 1 \end{bmatrix} \right) = C_{nn} = 2E_{nn} + 1$$

$$I_{8fs} = f_0 \cdot (Cs_0) = \begin{bmatrix} 1 \\ 0 \\ 0 \end{bmatrix} \cdot \left(\begin{bmatrix} C_{ff} & C_{fs} & C_{fn} \\ C_{sf} & C_{ss} & C_{sn} \\ C_{nf} & C_{ns} & C_{nn} \end{bmatrix} \begin{bmatrix} 0 \\ 1 \\ 0 \end{bmatrix} \right) = C_{fs} = 2E_{fs}$$

Calculate the 2nd Piola Kirchhoff stress tensor components using Equation 11-1 to describe passive deformation.

$$T_{dev}^{ff} = 4a_f E_{ff} x_{endo}^2 \cdot \exp(4b_f x_{endo}^2 E_{ff}^2)$$

$$T_{dev}^{ss} = 4a_s E_{ss} x_{endo}^2 \cdot \exp(4b_s x_{endo}^2 E_{ss}^2)$$

$$T_{dev}^{nn} = 4a_n E_{nn} x_{peri}^2 \cdot \exp(4b_n x_{peri}^2 E_{nn}^2)$$

$$T_{dev}^{fs} = T_{dev}^{sf} = 2a_{fs} E_{fs} \cdot \exp(4b_{fs} E_{fs}^2)$$

11.3 Appendix 1C

Derivation of the 2nd Piola Kirchhoff Stress tensor components from Equation 11-3 (see section 6.3).

Equation 11-3

$$\begin{aligned}\bar{W} = & \frac{a_s}{2b_s} [\exp(b_s x_{peri}(I_{4s} - 1)^2) - 1] + \frac{a_f}{2b_f} [\exp(b_f(I_{4f} - 1)^2) - 1] \\ & + \frac{a_n}{2b_n} [\exp(b_n x_{endo}(I_{4n} - 1)^2) - 1] + \frac{a_{fs}}{2b_{fs}} [\exp(b_{fs} I_{8fs}^2) - 1]\end{aligned}$$

Rewrite new invariants in terms of Green's strain tensor E .

$$E = \frac{1}{2}(\mathcal{C} - I)$$

$$I_{4f} = f_0 \cdot (Cf_0) = \begin{bmatrix} 1 \\ 0 \\ 0 \end{bmatrix} \cdot \left(\begin{bmatrix} C_{ff} & C_{fs} & C_{fn} \\ C_{sf} & C_{ss} & C_{sn} \\ C_{nf} & C_{ns} & C_{nn} \end{bmatrix} \begin{bmatrix} 1 \\ 0 \\ 0 \end{bmatrix} \right) = C_{ff} = 2E_{ff} + 1$$

$$I_{4s} = s_0 \cdot (Cs_0) = \begin{bmatrix} 0 \\ 1 \\ 0 \end{bmatrix} \cdot \left(\begin{bmatrix} C_{ff} & C_{fs} & C_{fn} \\ C_{sf} & C_{ss} & C_{sn} \\ C_{nf} & C_{ns} & C_{nn} \end{bmatrix} \begin{bmatrix} 0 \\ 1 \\ 0 \end{bmatrix} \right) = C_{ss} = 2E_{ss} + 1$$

$$I_{4n} = n_0 \cdot (Cn_0) = \begin{bmatrix} 0 \\ 0 \\ 1 \end{bmatrix} \cdot \left(\begin{bmatrix} C_{ff} & C_{fs} & C_{fn} \\ C_{sf} & C_{ss} & C_{sn} \\ C_{nf} & C_{ns} & C_{nn} \end{bmatrix} \begin{bmatrix} 0 \\ 0 \\ 1 \end{bmatrix} \right) = C_{nn} = 2E_{nn} + 1$$

$$I_{8fs} = f_0 \cdot (Cs_0) = \begin{bmatrix} 1 \\ 0 \\ 0 \end{bmatrix} \cdot \left(\begin{bmatrix} C_{ff} & C_{fs} & C_{fn} \\ C_{sf} & C_{ss} & C_{sn} \\ C_{nf} & C_{ns} & C_{nn} \end{bmatrix} \begin{bmatrix} 0 \\ 1 \\ 0 \end{bmatrix} \right) = C_{fs} = 2E_{fs}$$

Calculate the 2nd Piola Kirchhoff stress tensor components using Equation 11-1 to describe passive deformation.

$$T_{dev}^{ff} = 4a_f E_{ff} \cdot \exp(4b_f E_{ff}^2)$$

$$T_{dev}^{ss} = 4a_s E_{ss} x_{peri} \cdot \exp(4b_s x_{peri} E_{ss}^2)$$

$$T_{dev}^{nn} = 4a_n E_{nn} x_{endo} \cdot \exp(4b_n x_{endo} E_{nn}^2)$$

$$T_{dev}^{fs} = T_{dev}^{sf} = 2a_{fs} E_{fs} \cdot \exp(4b_{fs} E_{fs}^2)$$

11.4 Appendix 2A

	WKY_20120719_01	WKY_20120808_01	WKY_20120810_01	WKY_20120816_01	WKY_20120810_02
	initial estimate	optimisation result	initial estimate	optimisation result	initial estimate
af	24.82	11.732	24.82	31.334	24.82
afs	0.37	0.175	0.37	0.467	0.37
an	6.35	3.002	6.35	8.017	6.35
as	6.94	3.280	6.94	8.761	6.94
bf	11.32	12.747	11.32	1.509	11.32
bfs	11.67	13.141	11.67	1.555	11.67
bn	0.22	0.248	0.22	0.029	0.22
bs	7.07	7.961	7.07	0.942	7.07
M	1	0.473	1	1.262	1
N	1	1.126	1	0.133	1
rn	0.158		1.8e-3	3.934e-5	5.21e-5
					2.227e-4

Table 11-1 Results of 'M' and 'N' optimisation for WKY geometries (rn = resnorm)

11.5 Appendix 2B

SHR 20120824_02 , WKY_20120808_01						
	$x_{endo} = 5, x_{peri} = 6$		$x_{endo} = 5, x_{peri} = 8$		$x_{endo} = 5, x_{peri} = 10$	
	initial estimate	optimisation result	initial estimate	optimisation result	initial estimate	optimisation result
af	24.82	32.942	24.82	31.906	24.82	30.509
afs	0.37	0.491	0.37	0.476	0.37	0.455
an	6.35	8.428	6.35	8.163	6.35	7.806
as	6.94	9.211	6.94	8.921	6.94	8.531
bf	11.32	0.101	11.32	1.422	11.32	5.737
bfs	11.67	0.105	11.67	1.466	11.67	5.915
bn	0.22	0.002	0.22	0.028	0.22	0.112
bs	7.07	0.063	7.07	0.888	7.07	3.583
M	1	1.327	1	1.285	1	1.23
N	1	0.009	1	0.126	1	0.507
rn	2.3e-3		2.1e-3		2.5e-3	

Table 11-2 Summary of results of 'M' and 'N' optimisation for simultaneous fit of WKY and SHR geometries using experimental EDV values (rn = resnorm) (see section 7.3.2.4).

11.6 Appendix 2C

SHR 20120824_02 , WKY_20120808_01						
	$x_{endo} = 5, x_{peri} = 6$		$x_{endo} = 5, x_{peri} = 8$		$x_{endo} = 5, x_{peri} = 10$	
	initial estimate	optimisation result	initial estimate	optimisation result	initial estimate	optimisation result
af	24.82	25.148	24.82	24.509	24.82	23.972
afs	0.37	0.375	0.37	0.365	0.37	0.357
an	6.35	6.434	6.35	6.270	6.35	6.133
as	6.94	7.032	6.94	6.853	6.94	6.703
bf	11.32	9.505	11.32	10.786	11.32	12.109
bfs	11.67	9.799	11.67	11.119	11.67	12.483
bn	0.22	0.185	0.22	0.210	0.22	0.235
bs	7.07	5.936	7.07	6.736	7.07	8.562
M	1	1.013	1	0.987	1	0.966
N	1	0.840	1	0.954	1	1.070
rn	1.3e-3		08.44e-4		7.24e-4	

Table 11-3 Summary of results of 'M' and 'N' optimisation for simultaneous fit of WKY and SHR geometries ($rn = resnorm$) with EDV values summarised in Table 7-11 (see section 7.3.2.4).

11.7 Appendix 2D

SHR 20120824_02 , WKY_20120808_01						
	$x_{endo} = 5, x_{peri} = 6$		$x_{endo} = 5, x_{peri} = 8$		$x_{endo} = 5, x_{peri} = 10$	
	initial estimate	optimisation result	initial estimate	optimisation result	initial estimate	optimisation result
af	24.82	11.692	24.82	11.913	24.82	11.692
afs	0.37	0.495	0.37	0.537	0.37	0.495
an	6.35	8.490	6.35	9.217	6.35	8.490
as	6.94	9.279	6.94	10.073	6.94	9.279
bf	11.32	27.040	11.32	27.431	11.32	27.040
bfs	11.67	7.539	11.67	8.368	11.67	7.539
bn	0.22	0.142	0.22	0.158	0.22	0.142
bs	7.07	4.567	7.07	5.070	7.07	4.567
M	1	1.337	1	1.451	1	1.337
N	1	0.646	1	0.717	1	0.646
O	1	0.471	1	0.480	1	0.471
P	1	2.389	1	2.423	1	2.389
rn	1.26e-4		3.61e-5		2.61e-5	

Table 11-4 Summary of results of 'M', 'N', 'O' and 'P' optimisation for simultaneous fit of WKY and SHR geometries (rn = resnorm) to compliance curves (see section 7.3.2.7).

11.9 Appendix 3A

Filename Main_ParameterFitting_Multivariate.m

This file is the main framework used to optimise parameter sets, applying an experimental end diastolic volume offset.

```
%% This script estimates two scaling parameters M & N using Least
Squares Non Linear fitting
%% This matlab file is designed to write a CellML file and CMISS com
file to solve 4 versions of rat geometries (normal WKY, and 12, 18
and 24 month SHR) and subsequently analyse the stress-strain
relationship and passive pressure volume relationship during
diastole
```

```
function Main_ParameterFitting_Multivariate
clc;
clear all;
close all;

options = optimset('Display','iter',...
    'TolX' ,1e-7,....
    'TolFun' ,1e-10,....
    'MaxFunEvals' ,500,....
    'DiffMaxChange' ,1,....
    'DiffMinChange' ,1e-6,....
    'TolCon' ,1e-15,....
    'largeScale','on');

% TolX on parameters
% TolFun on objective function

% Initial guess for 'M' and 'N', using our own parameter
% This assumes all other parameters are constant

m0 = [1 1];
lb = [0.0001 0.0001]; %lower bound
ub = [60 60]; %upper bound

% Define the array to store 'modes', which are the versions of
geometry
% '00': 12 WKY
% '12': 12 SHR
% '18': 18 SHR
% '24': 24 SHR

modes = '00';

f=@(M)ErrorFunction(M,modes);
% Estimate new material parameter M & N using least squares non
linear minimization of the objective function

[m_new,resnorm,residual] = lsqnonlin(f,m0,lb,ub,options)

end

%% SOLVE THE MODEL IN CMISS
```

```

function [pressure, volume] = SolveDeformation(M, modes)
%% Setting up the files for solving
Write_IPCELL_WKY(M);

% Generate a com file to solve for passive inflation in CMISS
filenamew= ('Forward_Holzapfel_Prolate_cell_WKY.com');
fidw=fopen(filenamew,'w');
fprintf(fidw, '#Forward solve for 1x1x1 cube using 1st modification
of Holzapfels law implemented with CellML\n');
fprintf(fidw, ' set echo on\n');
fprintf(fidw, '$mode="%s"\n',modes);
fprintf(fidw, ' read commands;prolate_cellml_WKY;\n');
fprintf(fidw, ' fem quit;\n');

% Close the com file
fclose(fidw);

% Run CMISS to solve for passive inflation
fprintf('**** Initiate CMISS to calculate volume for M= %f
****\n',M);
system('rm Output.out');
system('cm Forward_Holzapfel_Prolate_cell_WKY.com ->& Output.out');
fprintf('**** Finished solving mode %s.....\n',modes);

%% Once the model is solved, process PV data output from CMISS
% Read in pressure volume data from file
[pressure, volume] = ReadPressureVolume(modes);

% Truncate arrays to match length of experimental data (assuming
same pressure increments)
pressure = pressure(4:30);
volume = volume(4:30);
disp(length(volume));

end

%% ANALYSE THE DATA
function [pressure, volume, compliance] = ReadPressureVolume(modes)
% Get pressure and volume information from file
clear pressure;
clear volume;
clear compliance;
clear stuff;

% Open file for reading
filename = sprintf('RecordingPV_WKY_%s.txt',modes);
fid=fopen(filename,'r');

% Store entire file content into 'stuff' array
stuff=textscan(fid,'%s'); % reads into array of characters
stuff=stuff{1,1};
numSteps = size(stuff,1);

for i = 1:(numSteps(1)/2)
    pressure(i) = str2num(stuff{i*2 -1}); %reading in odd values
    volume(i) = str2num(stuff{i*2}); %reading in even values
end

```

```
% Convert units for Pressure and Volume
% Default CMISS pressure (kPa) -> mmHg (experimental data)
% Default CMISS volume (mm^3) -> mL (experimental data)
pressure = pressure*7.500;
volume = volume*0.001;

% Save variables to file
savefileas = sprintf('JUSTSOLVE_%s', modes);
save(savefileas);
st = fclose(fid);
end

%% DETERMINING THE ERROR (Objective Function)

function error = ErrorFunction(M,modes)

% Gives model values for pressure and volume
[pressure, volume] = SolveDeformation(M,modes);

% Truncate vectors to exclude 0-3mmHg & set a max pressure of 15mmHg
volume = volume(5:16);
pressure = pressure(5:16);

% Read in PV data from Experimental data set, where
% ExperimentalData = [pressure, WKY18, SHR12, SHR18, SHR24]

load('ExperimentalData.csv');

pressure_exp = ExperimentalData(:,1);
if modes=='00'
    volume_exp=ExperimentalData(:,2);
elseif modes=='12'
    volume_exp=ExperimentalData(:,3);
elseif modes=='18'
    volume_exp=ExperimentalData(:,4);
elseif modes=='24'
    volume_exp=ExperimentalData(:,5);
end

ExpData = {'WKY12' 'SHR12' 'SHR18' 'SHR24'};

% Apply volume offset to experimental data
EDV=774;
fprintf('EDV is %f ....\n',EDV);
EDV_exp=volume_exp(find(pressure_exp==6));
WKY12 = volume_exp + (EDV/1000-EDV_exp);

% Truncate WKY data to 15mmHg max
WKY12 = WKY12(1:12);

% Define objective function
error = volume - WKY12';

disp('error = ');
disp(error);
end
```

11.10 Appendix 3B

Filename: prolate_cellml.com

This file simulates passive inflation of the ventricle using CMISS. It is called by the MATLAB script in Appendix 3A.

```
##### This com file is designed to simulate ventricular passive
inflation #####
use MechanicsAuxil_SHR;

# make an output directory for the current mode
$OUTPUT_DIR = "output_".$mode."/ "
if( ! -d ${OUTPUT_DIR})
{mkdir ${OUTPUT_DIR};}

$outputAll="outputAll_".$mode."/ ";
if( ! -d ${outputAll})
{mkdir ${outputAll};}

# Make an output directory for the current mode
$output_CavityVolume = "output_CavityVolume_".$mode."/ ";
if( ! -d ${output_CavityVolume})
{mkdir ${output_CavityVolume};}

$output_CavityVolume = "output_CavityVolume_".$mode."/ ";

#system('rm *.txt');

##### Define the regions #####
$WALL=1;
$CAVITY=2;
##### Define the class #####
$TISSUE=1;
$CELL=2;
#### Step 1: Read in auxiliary files for setting up the model #####
fem define param;r;prolate           # 3D prolate spheroidal
fem define reg;r;two                 # Define two regs: 1) wall 2) cavity
fem define coordinate;r;profib reg $WALL          # 4 nodes
#### Step 2(a): Read in the wall model (ipnode and ipelem) #####
fem define node;r;prolate_fitted_Endo_SHR reg $WALL
# wall model (ipnode): 4 nodes
fem define base;r;profib   # trilinear + quadratic hydr. pressure
fem define element;r;prolate_fitted_Endo reg $WALL
# single axisymmetric element

##### Calculates LV Wall Volume #####
fem list elements;LVWALL total region 1;

$LV_WALL_VOLUME=`awk '\$1=="Total"{printf("%d",\$4);exit}' \
LWALL.opelem`;
print "\nLV pressure = ${LV_P}\n LV_volume=${LV_WALL_VOLUME} \n";
```

```

fem export nodes;undeformed_${mode} as undeformed_${mode} reg $WALL
# Export the reference undeformed model for visualisation in CMGUI
fem export elements;undeformed_${mode} as undeformed_${mode} reg
$WALL
# Export the reference undeformed model for visualisation in CMGUI

fem list element total reg $WALL;
    # Calculate the wall volume
fem group elem 1 as ALL_ELEMENTS reg $WALL;

##### Step 2(b): Read in the cavity model (ipnode and ipelem) #####
fem define coor;r;cavity reg $CAVITY
fem define node;r;LVCavity_SHR reg $CAVITY # cavity model (ipnode)
fem define elem;r;LVCavity_SHR reg $CAVITY

fem export node;LVCavity_SHR as LVCavity_SHR reg $CAVITY
fem export elem;LVCavity_SHR as LVCavity_SHR reg $CAVITY

fem list element total reg $CAVITY
    # Calculate the cavity volume
fem list elements; $output_CavityVolume/LVCavity_0.0 total region 2;
$LV_P=0.0;
$LV_CAVITY_VOLUME=`awk '\$1=="Total"\{printf("%d",\$4);exit\}' \
$output_CavityVolume/LVCavity_0.0.opelem`;
MechanicsAuxil_SHR::writePressureVolume($LV_P,$LV_CAVITY_VOLUME,$mod
e);

##### Step 3: Read in auxiliary files for setting up the FE problem
for tissue #####
fem define fibre;r;profib reg $WALL
# Theoretical fibre angles: +80(endo) and -60 (epi)
fem define element;r;profib fibre reg $WALL      # fibre elements

fem export nodes;undeformed_${mode} as undeformed_${mode} reg $WALL
# Export the reference undeformed model for visualisation in CMGUI
fem export elements;undeformed_${mode} as undeformed_${mode} reg
$WALL
# Export the reference undeformed model for visualisation in CMGUI

fem define equation;r;profib reg $WALL class $TISSUE lock;
# 3D, finite elasticity
fem define material;r;holzapfel_sheet_2012 reg $WALL class $TISSUE;
# modified Holzapfel equation with normal term and collagen
fractions
#fem define active;r;zero reg $WALL class $TISSUE;
#Set up activation, initial 0 during passive inflation
fem define initial;r;profib reg $WALL class $TISSUE;
# Set up boundary conditions: 1) preload = 1kPa;
# 2) Fix mu (longitudinal) coordinates of all nodes;
# 3) Fix theta (angular) coordinate of node 2 (endocardial) to
prevent rigid body rotation
fem define solve;r;profib reg $WALL class $TISSUE;
# Define solving method: Newton iterations

##### Step 4: Define the grid #####
fem define grid;r;ProlateGrid gauss region $WALL class $CELL;

```

```

# Define the grid
fem update grid geometry region $WALL;
# Sets up the grid geometry
fem group grid element ALL_ELEMENTS as ALL_GRID_PT;
# Group all grid points

fem def equa;r;CellEquation region $WALL class $CELL;
#Define the equation for the cell class
fem def mate;d region $WALL class $CELL;
# Define the material for the cell class

fem define cell;r;holzapfel_cellml_fitted_SHR region $WALL class
$CELL; # Define ipcell which defines which cellml file to use
fem define mate;r;sheets_normal_v2 cell region $WALL class $CELL;
# Define material for the cell, grid-point based
fem define init;d region $WALL class $CELL;
# Set default initial condition
fem define solv;r;CellSolve region $WALL class $CELL;
# Define the solving method for the cell class
fem solve region $WALL class $CELL to 0;
# Set time step for the time integration to be 0

##### Step 4: Simulate passive inflation until LV cavity pressure
reaches 1kPa (preload) #####
$ITERS =10;
$TOL = 1e-6;
$PRESS = 0;
$PRELOAD = 15/7.5; #convert mmHg in kPa
$stepstopreload = 15;
$i=0;

while ($i < $stepstopreload ){   # Increment to Preload Pressure

    $INCREM = $PRELOAD/$stepstopreload;
# This assumes 0 starting pressure

    $PRESS = $PRESS + $INCREM;
# Increase pressure using small increments
    $FILE = ${NAME1}.${PRESS};
    $i++;
=====
        print "\033[0;30;42m
=====
\033[0m\n";
print "\033[0;30;42m      Solving iteration $i, pressure $PRESS
\033[0m\n";
        print "\033[0;30;42m
=====
\033[0m\n";
=====
fem solve increment $INCREM iter $ITERS error $TOL reg $WALL class
$TISSUE;
        $NAME="LVInflation_".${mode}."_".${i}
        $FILE=$OUTPUT_DIR.${NAME};
        fem define initial;w;$FILE reg $WALL;

# Export the model first

```

```
fem export nodes;$FILE field as LVInflation reg $WALL;
fem export elements;$FILE field as LVInflation reg $WALL;

$NAME="LVInflation_".${mode}."_FibreStrain_".${i}
      $FILE=$OUTPUT_DIR.${NAME};
fem list strain;$FILE region 1;
$NAME="LVInflation_".${mode}."_FibreStress_".${i}
      $FILE=$OUTPUT_DIR.${NAME};
fem list stress;$FILE region 1;

      $FILE2=$outputAll."LVMODEL_".${i};
fem export nodes;$FILE2 field as LVMODEL region $WALL;
fem export eleme;$FILE2 field as LVMODEL region $WALL;
##### Calculate the cavity volume #####
read commands;Extract_Pressure
read commands;Cal_CavityVolume_SHR
##### Redefine initial condition and insolv file for the wall
$NAME="LVInflation_".${mode}."_".${i}
      $FILE=$OUTPUT_DIR.${NAME};
fem define initial;r;$FILE reg $WALL;
fem define solve;r;profib reg $WALL;
}

# Make a copy of the PV file under mode name
fem eval reaction;EndofInflation reg $WALL
# Evaluate the reaction force to ensure solution is converged,
optional
fem define initial;w;profib_EndInflation reg $WALL
# Export the deformed solution in ipinit format
fem export nodes;EndInflation_${mode} field as EndInflation_${mode}
reg $WALL
# Export the passively inflated at end diastole
fem export elements;EndInflation_${mode} field as
EndInflation_${mode} reg $WALL
fem list strain;WallStrain_ED_${mode} gauss region 1;
fem list strain;FibreStrain_ED_${mode} gauss region 1;
fem list stress;WallStress_ED_${mode} gauss region 1;
fem list stress;FibreStress_ED_${mode} gauss region 1;
```